Infrared Spectroscopy of Metal Cluster-Adsorbate Systems Solvated in Superfluid Helium Nanodroplets

by
Paul L. Stiles

A dissertation submitted to the faculty of the University of North Carolina at Chapel Hill in partial fulfillment of the requirements for the degree of Doctor of Philosophy in the Department of Computer Science.

Chapel Hill
2006

Approved by:

Roger E. Miller, Advisor

Lee G. Pedersen, Reader

Michael Rubenstein, Reader

Malcolm D. E. Forbes, Committee Member

H. Holden Thorp, Committee Member

ABSTRACT
PAUL L. STILES: Infrared Spectroscopy of Metal Cluster-Adsorbate Systems Solvated in Superfluid Helium Nanodroplets.
(Under the direction of Roger E. Miller.)

High-resolution infrared spectroscopy has been used to study various metal cluster-HCN systems solvated in superfluid helium nanodroplets. The metal clusters include magnesium, zinc, copper and silver. The weakly interacting nature of the helium droplets allowed for the free rotation of molecules solvated within them and, as a result, full rotationally resolved infrared spectra were acquired. The ro-vibrational spectra was used, along with extensive *ab initio* calculations, to determine the structures of the metal-HCN complexes. Through the application of moderate electric fields to the laser interaction region, we also were able to measure accurate dipole moments, giving further information about the nature of the interaction between adsorbate and metal cluster.

Dedicated to memory of Professor Roger E. Miller

ACKNOWLEDGMENTS

The life of a new student in a state-of-the-art chemical physics laboratory is a sink or swim affair. The thought of being able to understand the machinery, much less the science in a laboratory of the Miller labs complexity was, at times, overwhelming. Ultimately, with the support of my family and friends, through the tough times and long hours, I was able to achieve my goal of earning my Ph.D. degree.

First and foremost I would like to thank my parents, Bus and Lynda. They emphasized to me the importance of choosing a career that made me happy, regardless of financial gain. I love what I do and thank them for their excellent advice. Both were extremely patient with me and gave unconditional love, even when I probably did not deserve any. I know they are proud of me and I hope they understand how proud I am of them. I also want to thank Dawn, Tim, Daisy, Scott and Lexi. We make up the interesting clan that is called the Stiles family and I want them to understand how much I appreciate their support and love. I would not be the person I am today without their influence.

Of my non-family friends I have to thank Becky for her unbelievable patience with me as I battled through the stress of this last year. The tragic loss of Roger to lymphoma was terrible and meant that I would have to rely on others to help me with my thesis. Luckily for me, Becky is an excellent editor. Many thanks to Nate, Will, Scott, Eddie, Gary, Travis, Will Lewis, Jeremy and Myong-Yong. These are my friends who made my time in Chapel Hill, both in and out of lab, much more enjoyable. Thank you Tar Heel basketball for the 2005 NCAA national championship.

I would also like to thank the National Science Foundation for their generous support (CHE-04-46594).

Contents

List of Figures

List of Tables

Chapter 1

Introduction

1.1 Metal Clusters and Helium Droplets

A fundamental understanding of small metal clusters is of great importance to fields such as catalysis, surface and materials science. Metal cluster systems do more than just "bridge the gap" between the atomic and bulk regimes. In many cases they actually represent a unique class of molecules that can facilitate reactions or display completely new physical properties [2]. Study after study has shown that the properties of metal clusters can vary drastically from one cluster to another upon the addition or subtraction of a single metal atom [3, 4, 5]. Perhaps the most famous of these metal cluster studies is that of Haruta [6], who in 1993 reported the oxidation of CO over nanoscale gold clusters supported on metal oxides. This study was initially a great shock to the catalysis world because, as everyone knows, bulk gold is completely inert. The work sparked an explosion of research [7, 8, 9, 10, 11, 12, 13, 14](too much to review here) in the hope of understanding why the nanoscale gold clusters were reactive when their bulk counterpart was not. [3]

Soon after Haruta's discovery it became clear than solely an understanding of the metal cluster would not be sufficient. The interaction between adsorbate molecules and metal clusters would have to be tackled too. One of the best methods for such investigations is high-resolution infrared spectroscopy. Not only does this method offer detailed information about how complexation with metal clusters affects the adsorbate, but also, if the complex under investigation is rotationally resolved, direct evidence for metal-cluster structure can be obtained. Just as in other fields of chemistry, structure and function are intimately connected, and the quest for experimental evidence for metal-cluster structure is the first step towards a fundamental understanding. Although infrared spectra exist for adsorbate-metal cluster complexes [15, 16], there is virtually no infrared data that provides direct

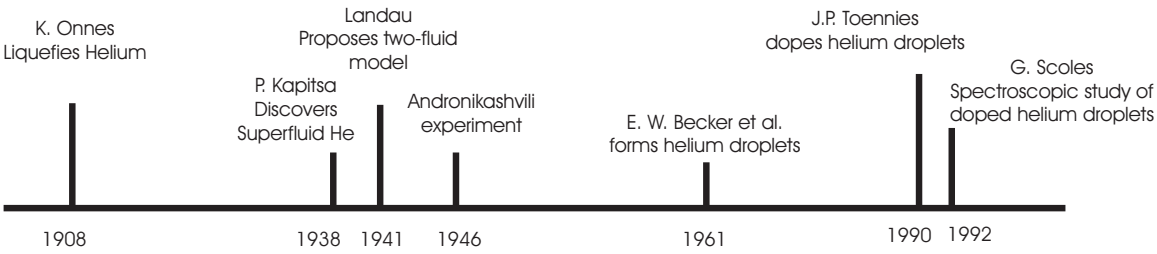

Figure 1.1: Superfluid Helium Timeline

structural evidence, i.e. rotationally resolved spectra.

The relatively new technique of using superfluid helium droplets is ideally suited for the study of metal-clusters and their interactions with adsorbates. The clusters of interest are grown in helium nanodroplets, a nearly ideal spectroscopic matrix [17, 18, 19]. The homogeneous and non-dissipative nature of the helium solvent results in infrared spectra that are rotationally resolved and from which we can obtain detailed structural information. Stark spectroscopy can also be performed within helium droplets, providing a probe of the extent of charge transfer between the metal complex and the adsorbate molecule. The experiments reported here are therefore quite unique, providing us with a new approach for studying these interesting and important systems. Although the focus of the present study is on magnesium, zinc, copper, silver and gold clusters, the method is quite general and can be applied to other metals.

1.1.1 Helium droplet history

Over the span of one century, helium has gone from an unexplained absorption line found during a solar eclipse to being used as a spectroscopic matrix. The story of helium begins with its discovery in 1895, by Sir William Ramsay. Following the timeline shown in Figure 1.1, the first step towards the development of helium droplet spectroscopy was the liquidification of helium in 1908 by Onnes [20]. After a great deal of research on the properties of liquid helium, Kapitsa discovered, once it was cooled below 2.17 K, liquid helium had the unusual ability to flow through small orifices without friction [21]. This critical point has since become know as the lambda point because the discontinuity in helium's heat capacity resembles the Greek letter, λ (Figure 1.2).

Kapitsa's discovery prompted him to lobby his friend and fellow Russian Lev Landau to take up the theoretical problem of superfluidity, as the phenomenon had become known. In a series of papers in the mid- to late-forties Landau proposed the two-fluid model [22]. The

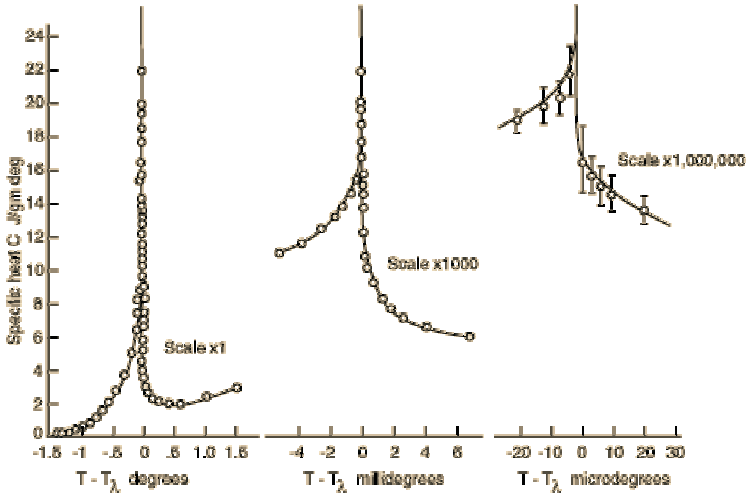

Figure 1.2: Liquid helium's discontinuity in heat capacity

model describes how helium, cooled below its lambda point (2.17 K), consists of a superfluid and normal-fluid fraction. In this model, the normal-fluid carries all of the viscosity while the superfluid fraction is capable of frictionless flow. In 1946 the two-fluid model was confirmed when Andronikashvilli performed his experiments that measured the moment of inertia of a series of discs suspended in helium [23]. As predicted by theory, the disks suspended in liquid helium gradually experienced less and less friction as the temperature of the helium was lowered from its lambda point.

The formation of helium droplets from a free jet expansion was first accomplished by Becker and co-workers in 1961 [24]. Early cluster studies were stymied, in large part, by the fact that helium droplets do not absorb light below 20 eV. This began to change when Toennies and co-workers [25, 26, 27] doped helium droplets by passing a beam of droplets through a pick-cell chamber containing gas-phase molecules. It was quickly realized that the optical transparency of helium could be turned into a great advantage when Scoles and co-workers carried out the first spectroscopic study of a molecule (SF_6) solvated within a helium droplet [28]. This early infrared experiment was done with a line tunable CO_2 laser, which was unable to resolve any rotational structure. Soon after, Frochtenicht et al. [29] used a diode laser to study the same band of SF_6 and found a rotationally resolved spectrum, suggesting free rotation within the droplet. The intensities of this spectrum were fit, and it was found that, in agreement with theory, the droplet temperature was 0.4 K.

The strong spectral evidence for free rotation and a temperature well below helium's lambda point quickly led researchers to suggest the superfluidity of these nanoscale droplets.

Given that the formal definition of superfluidity is based upon bulk thermodynamic quantities that are not well defined on the microscopic level, the actual "superfluidity" of helium droplets has been somewhat controversial [22]. Nevertheless, whether the free rotation of dopants within helium is called "superfluidity" or the "quantum exchange of helium atoms" [30], the fact remains that free rotation does exist within the droplet, making it a very unique substance.

1.1.2 Helium droplets vs. the gas-phase

Many insights into the nature of helium droplets were gained in the early rotationally resolved spectra of SF_6 [31]. Most importantly, it was found that the overall symmetry of the molecule was unchanged compared to the gas-phase and that simply using a modified set of fitting constants would be sufficient for the analysis of the spectrum. It was also discovered that the vibrational frequency of the solvated molecule was shifted very little from its corresponding gas-phase value. In contrast, large matrix shifts are quite common in molecules embedded in solid argon or neon, for example. (Since then, it has been found that matrix shifts due to helium are typically less than 1 cm^{-1} for free stretch vibrations.)

The near gas-phase environment of superfluid helium droplets is not without its complications. In 1996 the SF_6 experiments in helium droplets were revisited [19] with a continuously tunable diode laser. The high resolution laser made it possible for an accurate determination of the spherical top's rotational constant. Comparisons with the gas-phase showed that the helium droplet reduced the rotational constant by a factor of 3. It is now known that for heavy rotors ($B < 1$ cm^{-1}), a small fraction of the helium density contributes to the effective moment of inertia of the solvent molecule [32, 33, 30, 34]. Unfortunately, the degree to which the helium effects the rotational constant is known for only a few sample systems [35, 36, 37, 38], as the complexity of such calculations is great. To date, however, enough systems have been measured in the droplet to make some empirical conclusions, namely, that for heavy rotors ($B < 1$ cm^{-1}) the helium rotational constants are reduced by a factor of 2.5 ± 0.5 [39, 40, 41, 30]. This trend is shown in Figure 1.3 and will be referred to several times in the work. Physically, in the "adiabatic following regime" [35], as it has become known, a heavy molecule rotates slow enough for a small fraction of the helium solvent to rotate along with the molecule, resulting in a larger moment of inertia (smaller rotational constant). In contrast, a smaller, lighter molecule rotates much too fast for the helium to follow and as a result the rotational constants are very close to their gas-phase counterparts.

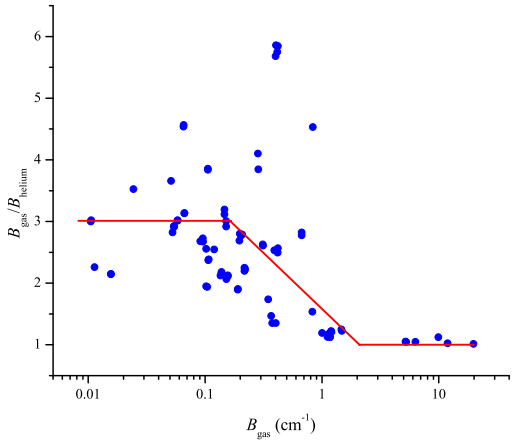

Figure 1.3: Comparison of measured B rotational constants in helium and the gas-phase as a function of rotational constant

Chapter 2

Experimental Method

In the last decade of expansion in the field of superfluid helium droplets many different avenues of research have been pursued. Some quick examples include time-of-flight mass spectrometry studies of large clusters, atomic reactions on or in helium droplets, and laser induced fluorescence of doped helium droplets. The laboratory in which this data was obtained utilized the technique of high-resolution infrared spectroscopy to probe the complexes formed within helium droplets. The following chapter will explain the helium droplet formation process, the pick-up technique, helium droplet beam depletion detection via optothermal methods, and the method of pendular spectroscopy.

The continuous stream of helium droplets is created by expanding ultrapure helium (99.9999micron nozzle. Helium pressures behind the nozzle are typically around $40-60$ bar, with the baseline pressure in the source chamber of 10^{-6} torr. The droplets are formed in the high pressure portion of the expansion and as the pressure falls below the equilibrium vapor pressure of the droplets, they cool by evaporation to a temperature of 0.37 K. This all takes place in the first chamber shown in Figure 2.1. In general, droplets can be formed with essentially any size, depending upon the source temperature and pressure, from a few hundred atoms to droplets containing in excess of a million helium atoms [42, 43, 44, 45]. In the latter case, the nozzle temperature is lowered to the point where the helium liquefies within the nozzle. The resulting liquid jet then breaks up into droplets of much larger size [46, 47].

Figure 2.2 shows a set of calibration curves for the ^{4}He mean droplet size, as a function of source temperature and pressure [48, 49, 47, 45]. For nozzle conditions which produce the smaller droplets (a few thousand atoms or less) typically used for spectroscopy, it is now generally accepted that the droplet size distribution is log-normal [48, 49], although the experimental evidence for this is still indirect. It is nevertheless clear that the droplet size distribution is quite broad, so that at a given mean droplet size there is a wide range of sizes

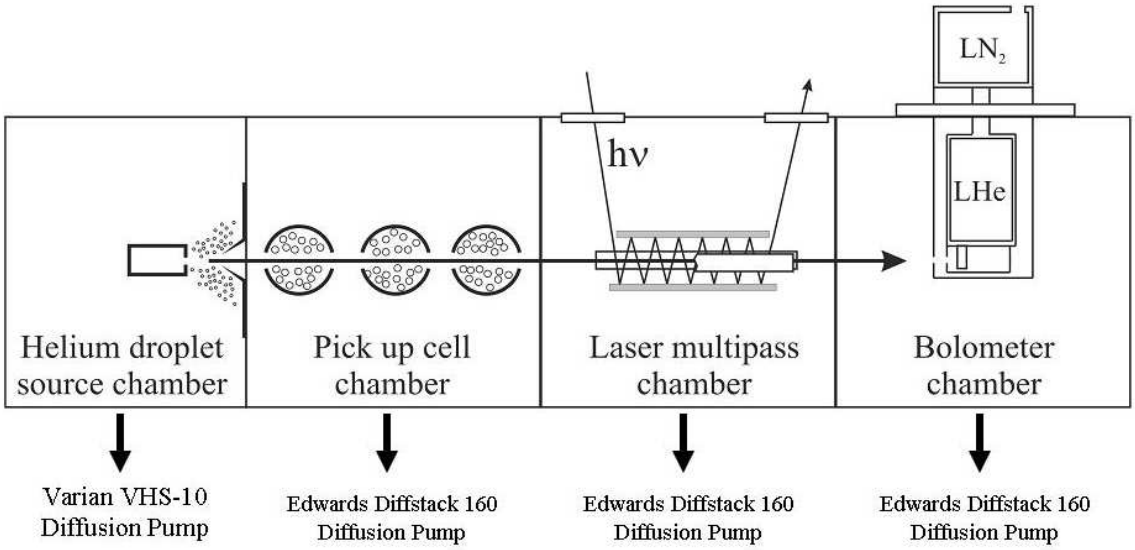

Figure 2.1: Schematic diagram of the differentially pumped bolometer based helium droplet spectrometer instrument. A multipass cell is used to cross the laser with the droplet beam many times. A pair of electrodes straddle the laser interaction region for their use in Stark/pendular spectroscopy.

present in the beam, as illustrated by the log-normal distributions shown in Figure 2.2. The ability to vary the droplet size is extremely important when forming larger complexes, given that the droplet must have significant heat capacity to accommodate the heats of formation of these species, without the loss of all the helium by evaporation. For spectroscopic studies it is generally best to work with the smallest possible droplets, since by simple conservation of helium, there are fewer droplets when the mean size is large. Fewer droplets mean fewer dopant molecules, which translates into low spectroscopic signals, assuming the sensitivity is linearly dependent upon the number of absorbers. Depending upon the nozzle temperature, the droplet velocities [50, 48] typically fall in the range 200-400 m/sec (although droplets as slow as 50 m/s have been produced [43]), meaning that in a typical apparatus, with a beam path length of 1 meter, the flight time of the droplets is approximately 2-5 msec.

2.1 Pick-up technique

As indicated in Figure 2.1, the helium expansion is skimmed to form a well collimated droplet beam in a second differential pumping chamber. The large cross sections associated with the droplets necessitate a low background pressure in the second chamber, to avoid the unwanted

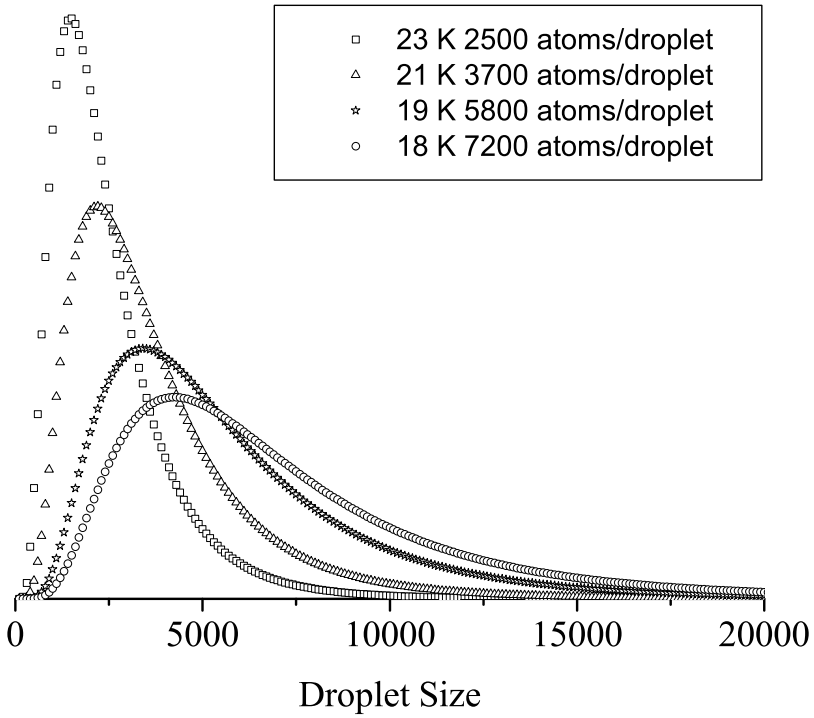

Figure 2.2: Calculated lognormal helium droplet distributions for several nozzle conditions and a constant backing pressure of 50 bar. The average droplet size for each condition is given in the legend

contamination of the droplets. This is particularly true for the very largest droplets, where we find that pressures in the low 10^{-8} Torr range are required to avoid water contamination.

Intentional doping of the droplets with the species of interest is accomplished using the pick-up technique first developed for heavier rare gas clusters [25, 26]. This involves passing the beam through a pick-up chamber maintained at a pressure sufficient to permit the capture of the desired number of gas phase atoms or molecules. For droplets in the size range 1,000-5,000 atoms and a pick-up cell length of 10 cm, this corresponds to a pressure of approximately 10^{-6} Torr [27]. As discussed in detail previously [51, 52], the pick-up process obeys Poisson statistics [27], and as such, the probability that a droplet captures a given number of molecules, k, from the pick-up cell of length L is given by

$$P(k) = \frac{(\alpha L)^k}{k!} exp - (\alpha L) \tag{2.1}$$

where $\alpha = \rho\,\sigma$, ρ being the number density of the gas in the pick-up cell, and σ being the cross section of the droplet. The high mobility of the molecules in the superfluid helium combined with the small droplet volume ensures that the captured impurities quickly condense to form molecular clusters. Thus, the average size of the clusters formed in the droplets can be changed by simply varying the pick-up cell pressure.

The signal dependency on pickup cell pressure has become an invaluable tool in the assignment of cluster species within helium droplets. As shown in Figure 2.3, HCN monomer has an optimal signal at the lowest pressures, while the larger multimers optimize with increasing pickup cell pressure. With just the simple adjustment of a needle-valve leading to the pickup cell, one can be reasonably sure of the source of a particular vibrational band.

2.1.1 Metal Oven

The only requirement for the pick-up of dopants within a helium droplet is that the gas pressure is sufficiently high to ensure a collision between the droplet and dopant. For the doping of metal atoms into the droplets, the requirement is for an oven that can heat a given metal to sufficiently high vapor pressure. This is generally done using an alumina coated tungsten crucible that is placed directly below the helium droplet beam. It has been the experience of this author that metal must be heated to temperatures that bring the metal's vapor pressure to at least $1x10^{-4}$ torr. The crucible (Figure 2.4) is mounted between two large, water-cooled, copper electrodes that allow for very large currents to pass through the heater element. With this oven, we can heat metals up to 1300 C, which covers a large range of metals that can be vaporized (Table 2.1).

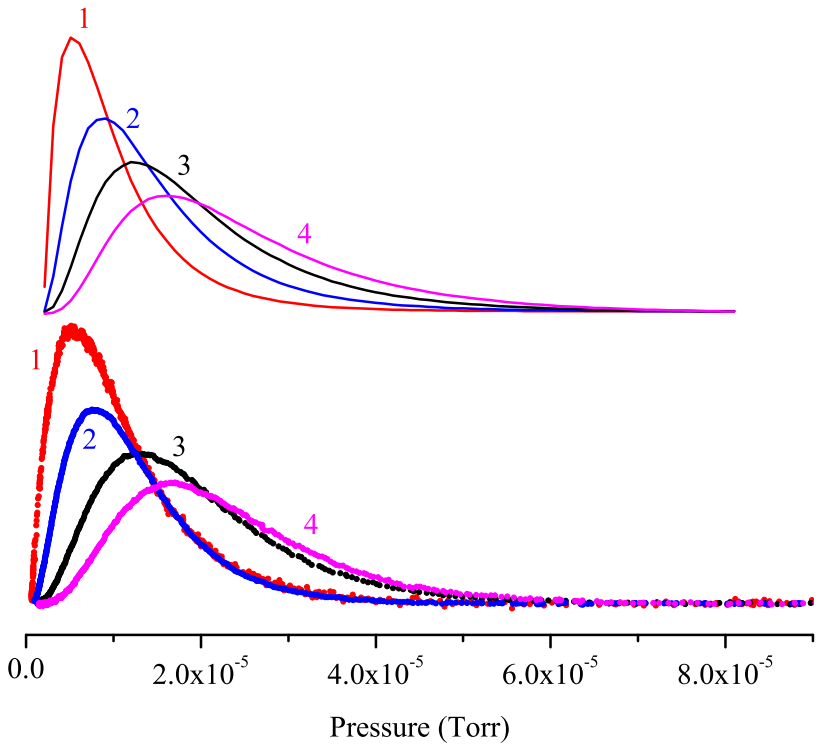

Figure 2.3: Pick-up cell pressure dependencies for HCN. The uppermost curves correspond to the simulated pick-up probabilities, while the lower curves were obtained experimentally. The monomer (1), dimer (2), trimer (3) and tetramer (4) are labeled accordingly.

Table 2.1: Vapor pressures for various metals at given temperatures. Temperature is given in degrees Celsius.

	Vapor Pressure (Torr)			
Metal	10^{-6}	10^{-5}	10^{-4}	10^{-3}
Silver	685	752	832	922
Gold	947	1032	1132	1252
Copper	852	937	1027	1132
Magnesium	246	282	327	377
Zinc	177	209	247	292

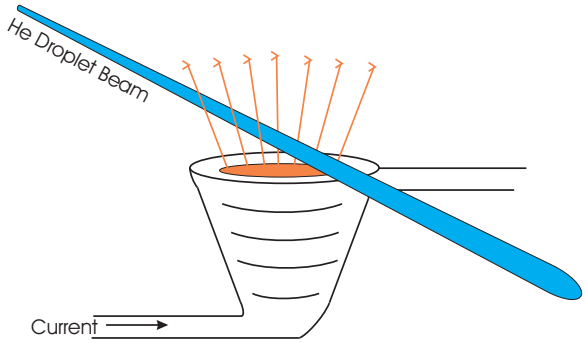

Figure 2.4: Resistively heated alumina crucible

2.2 Laser system

All of the spectroscopic experiments presented in this thesis were undertaken using a Burleigh FCL-20 color center laser, pumped with a Coherent Sabre model Kr-ion laser. Using the KCl:Li and RbCl:Li crystals, this system can continuously scan from 3000 cm^{-1} to 4100 cm^{-1}. The output power can range from 10 mW to 25 mW. The principles of the color center laser and scanning techniques can be be found elsewhere [53, 54, 55, 56].

2.3 Detection

The acquisition of IR spectra was undertaken through the detection of a laser induced depletion of the helium droplet beam. Briefly, the droplets which contain an infrared active molecule in the laser frequency range will absorb a photon as it passes through the laser multipass cell, shown in Figure 2.1. The vibrationally excited molecule will then relax back down to the ground state by transfering its energy to the helium droplet. This in turn heats the droplet, which cools back down to 0.37 K by the evaporation of helium atoms. It is know through bulk liquid helium experiments that 1 cm^{-1} of energy corresponds to the evaporation of 5 helium atoms [27], so in a typical IR experiment (3000 cm^{-1}) approximately 600 helium atoms are evaporated per photon absorbed. A spectrum is acquired by monitoring the beam depletion as a function of laser frequency.

There are currently two methods for the detection of laser induced depletion of the helium droplet beam. The first, which was not used in this study, is through the use of a mass spectrometer [57, 29, 40] and will not be discussed. The second and preferred method for this lab is through the use of a bolometer [58, 59]. A bolometer is a thermal device used to measure the energy of the droplet beam. It is essentially a very sensitive thermometer, which consists

of a semi-conductor element in series with a reference resistor. The bolometer is coupled to a liquid helium cryostat that is continuously pumped in order to reach its operating temperature of 1.6 K. The helium beam impacts the bolometer element and provides us with a constant background. When droplet beam depletion is induced, the bolometer detects this through a loss in signal.

2.4 Pendular spectroscopy

The extremely cold environment that is found within helium droplets (0.37 K) makes the use of pendular spectroscopy especially useful [60, 61, 62, 63]. The word "pendular" was used to describe this type of spectroscopy because when a polar molecule is placed in a DC electric field it behaves as a quantum pendulum. The electric dipole moment of the molecule orients along the electric field lines. The lower the rotational temperature and the larger the electric field the more oriented the molecule becomes. At high temperatures the fields required to achieve significant orientation are often impractically high, but due to the low temperature of the helium droplet highly oriented states can be achieved at moderate fields.

For a parallel band the entire ro-vibrational spectrum collapses into a single transition when the laser polarization is aligned parallel to the DC field. As a result, large increases in the signal-to-noise level are achieved. The electrodes shown in Figure 2.1 were used to apply the DC field to the laser interaction region. We also can apply smaller fields to this same region and record Stark spectra of rotationally resolved bands. This will be discussed in detail in the next chapter.

Chapter 3

Dipole moments in helium droplets

In this chapter, Stark spectra are reported for hydrogen cyanide and cyanoacetylene solvated in helium nanodroplets. The goal of this study is to understand the influence of the helium solvent on measurements of the permanent electric dipole moment of a molecule. We find that the dipole moments of the helium-solvated molecules, calculated assuming the electric field is the same as in vacuum, are smaller than the well-known gas-phase dipole moments of HCN and HCCCN. A simple elliptical cavity model quantitatively accounts for this difference, which arises from the dipole-induced polarization of the helium.

3.1 Introduction

The field of helium droplet spectroscopy has recently undergone rapid expansion into some new and exciting areas [41, 19, 64, 65, 66]. Part of the interest in this field stems from the fact that the interaction between a solvated molecule and the helium is so weak that the corresponding vibrational frequencies are often only slightly shifted from the gas phase values. As a result, vibrational spectra obtained for the solvated molecules can be compared with the results of ab initio calculations, without the need to account for the matrix shift. In contrast, the rotational constants of molecules are quite different from the gas phase values, owing to the fact that the motion of the molecule is accompanied by the correlated movement of the surrounding helium atoms [67, 35, 68, 69, 70]. Considerable progress has been made towards the development of theories [69, 71, 67, 70] to explain this phenomenon and a quantitative understanding is within sight.

Although molecular spectroscopy can provide detailed information on many other properties of these systems, including the permanent electric dipole moment, as of yet these have remained largely unexplored. In the present paper we consider the effects of the helium

solvent on the measured electric dipole moment of molecules. This work is motivated by the interest in using dipole moments as probes of the structure and bonding in molecules and their complexes. Indeed, the dipole moments of metal-adsorbate complexes [72] are particularly useful in determining the structure of these species and the nature of the bonding, including the onset of charge transfer [73]. Large electric fields are also being used to orient polar molecules in helium [74], further increasing the practical importance of accurate dipole moment measurements. The goal of the present study is to shed light on how Stark spectra of solvated molecules need to be corrected to account for the effects of the solvent.

Two linear, polar molecules (HCN and HCCCN) are used in the present study to investigate the effects of the helium on the measured electric dipole moment. The dipole moments of HCN and HCCCN are accurately determined in the gas phase for the ground state [75, 76], and for HCN in the C-H stretch excited vibrational state [75, 77], so that quantitative comparisons can be made between the gas phase and helium data. The assumption is made that the charge distribution, and hence dipole moment, of the molecule is not directly affected by the helium solvent. This assumption is strongly justified by the fact that the interactions with helium are exceedingly weak, compared to the covalent bonds of the molecule. Therefore, any deviation from the gas phase dipole moment must result from the effective shielding of the applied field by the helium solvent. The current work represents a quantitative follow-up on a previous paper on the Stark effect of HCN in helium [78].

3.2 Experimental

In brief, the helium droplet source consists of a 5 m diameter nozzle, operated at 20 K, through which ultra-pure helium is expanded from 50 atmospheres. Under these conditions helium droplets are formed having a mean diameter of approximately 7 nm (4,000 atoms). These droplets pass through the pick-up cell, which is maintained at a pressure between 10^{-6} and 10^{-5} torr of HCN or HCCCN. In this region, the molecules are captured by the helium droplets and cooled to the equilibrium temperature of 0.37 K [39, 19]. The pick-up cell pressure was adjusted to optimize for the pick-up of a single molecule. The seeded droplets then pass through the laser excitation region, where vibrational excitation of the molecules in the helium droplet is followed by vibrational relaxation, causing the evaporation of several hundred helium atoms. The beam depletion is measured with a bolometer. By tuning the laser through the spectrum and recording the attenuation signal on the bolometer, it is possible to obtain the spectrum of the molecules in the liquid helium. In the present study we use an F-center laser to excite the C-H stretching vibration of the HCN and HCCCN.

The Stark spectra reported here were obtained by positioning a set of electrodes orthogonal to a multi-pass laser cell so that a DC electric field could be applied to the laser interaction region. The angle between the laser electric field direction and the DC field was adjusted to 45 using a Fresnel rhomb, so the $\Delta M = 0$ and $\Delta M = \pm 1$ transitions could be observed in a single scan. The vacuum electric field was calibrated by turning off the helium droplet beam and raising the pressure in the pick-up cell to the point where it acted like an effusive source for gas phase beam experiments. The Stark spectrum of the R(1) transition of gaseous HCN was recorded at several values of the applied electric field. Since the dipole moments and rotational constants of HCN are known in both the ground and vibrationally excited states, these Stark spectra can be used to accurately calibrate the electric field. The helium droplet measurements were then carried out under identical experimental conditions.

3.3 Dipole moment of HCN in Helium droplets

In the absence of an electric field, the infrared spectrum associated with the C-H stretch of HCN consists of a single R(0) transition, given that the rotational constant of HCN in helium is 1.0175 cm^{-1} 10965 and the droplet temperature is 0.37 K [39]. This transition is ideally suited for the measurement of the dipole moment of HCN in the vibrationally excited state, since the spacing between the $\Delta M = 0$ (parallel) and $\Delta M = \pm 1$ (perpendicular) transitions depends only on the excited state Stark effect. The spacing between these two transitions increases with field; therefore the most precise measurements of the dipole moment will be at the highest fields. The series of spectra shown in Figure 3.1 were recorded at a 45 polarization at different electric field strengths. Clearly the splitting between the two transitions increases with electric field strength in a non-linear fashion, consistent with the approximate second order Stark effect for HCN. It is important to point out that there is a small splitting between the two transitions even at zero field, which we explained previously [78] in terms of the anisotropic interaction between the helium and the molecule. Since this zero field splitting is rather small, compared to external field induced splittings at the highest fields, we neglected it in the analysis of the data.

The splitting between the $\Delta M = 0$ and $\Delta M = \pm 1$ components of the R(0) transition depends only on the magnitude of the applied field, the rotational constant and electric dipole moment of HCN in the vibrationally excited state. Since the rotational constant of the solvated molecule in the vibrationally excited state is accurately known from previous measurements [78] to be 1.175 cm^{-1}, the corresponding dipole moment can be determined. This should be considered an effective dipole moment, given that we are using the vacuum

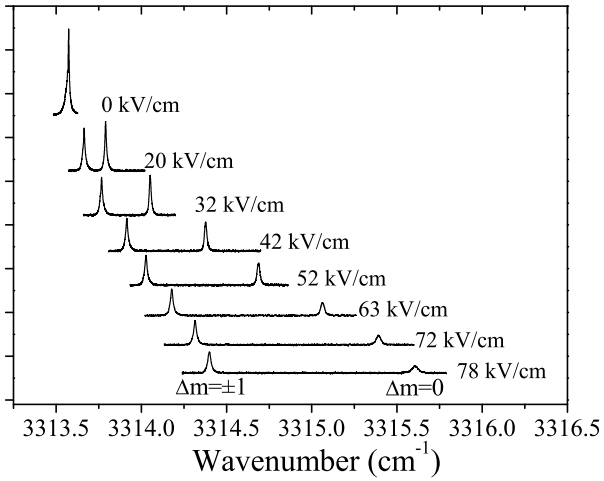

Figure 3.1: Series of Stark spectra of HCN in helium. The electric field strength at which the spectra were measured is indicated in the figure. The laser polarization was set to approximately 45o with respect to the applied electric field axis, in order to make the intensities of the $\Delta M = \pm 1$ and $\Delta M = 0$ transitions approximately equal.

field in this calculation. At the relatively high fields used in these experiments, a simple second order, perturbative treatment of the Stark effect is insufficient to determine the dipole moment. Instead, the Stark splittings were calculated by diagonalizing the full Hamiltonian matrix, including states of sufficiently high J to ensure convergence. As shown in Figure 3.2, the dipole moments obtained from these measurements are systematically lower than the gas phase dipole moment of HCN. The latter is indicated in the figure by the horizontal line at 3.0174 D, compared to the effective dipole moment of the solvated molecule of 2.949(6) D.

From work dating back as far as 1935 [79], it is known that the effective dipole moment in a liquid depends upon the dielectric constant of the solvent and the shape of the solute molecule. For the simple case where the molecules carve out a spherical cavity at the center of a spherical droplet, the solution to Laplace's equation is well known [80]. Using the dielectric constant of Donnelly and Barenghi [81], the corresponding ratio of the cavity field to that in the vacuum is 0.999312. This would give a slightly larger effective dipole moment, in contrast to the experimental results.

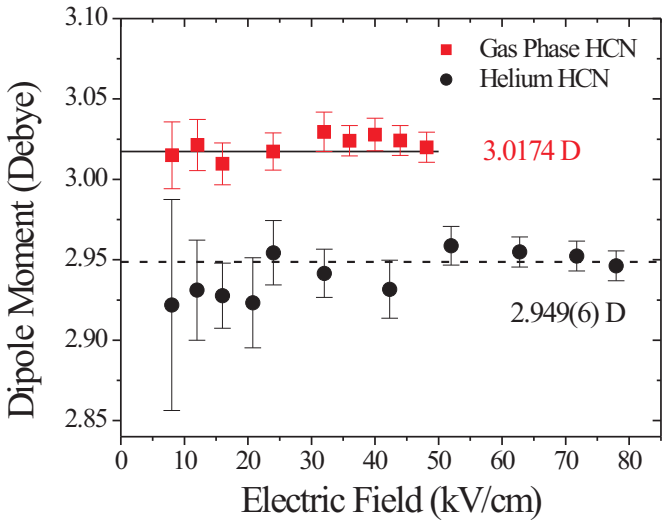

Figure 3.2: Plot of the dipole moments of HCN in the gas phase (squares) and in helium droplets (circles) at a variety of applied electric field strengths. The gas phase values are shown to illustrate the experimental accuracy of the measurement and to highlight the difference with the measurements in helium droplets. The two horizontal lines indicate the gas phase excited state dipole moment (3.0174 D) and the average value measured in helium droplets (2.949(6) D). The error bars reflect the accuracy of the measured peak positions and the uncertainty in the applied electric field strength determined from the gas phase data.

3.4 Higasi shielding model

We next consider the fact that the dipole moment of the solvated molecule polarizes the surrounding helium. The induction model of Higasi13719 can be applied to the present problem. The effective dipole moment in helium is simply the sum of the gas phase dipole moment of the molecule (μ_0) and the induced dipole moment of the surrounding solvent (μ_i). The shape of the solute cavity (determined by the shape of the molecule) is critical in determining the magnitude and direction of this induced dipole. For a spherical cavity with a point dipole at its center, the induced dipole averages to zero. A dipole in a prolate ellipsoidal cavity, appropriate for HCN, the contribution from the opposing induced dipoles (in the region of the short axis A) exceeds that from the helium along the long axis (B), making the effective dipole moment smaller. From the treatment of Higasi [79];

$$\mu_i = 4\pi\rho\alpha_m\mu_0 M^{-1}\left(\frac{-1}{k^2-1}\left[1 - \frac{k}{\sqrt{k^2-1}}\log_{10}\{k+\sqrt{k^2-1}\right] - \frac{1}{3}\right) \tag{3.1}$$

where

$$k = \frac{A}{B} > 1 \tag{3.2}$$

Based on the van der Waals radial for the atoms in HCN, we estimate that k = 2.93. The molar polarizability of helium was taken from Harris-Lowe and Smee [82] to be $\alpha_m = 0.123296$ cm^3/mole, and the helium density at 0.35 K was taken from Donnelly and Barenghi [81], namely 0.1451391 g/cm^3. These constants yielded a value for i of -0.0473 D, for a calculated dipole moment of 2.970 D, in rather good agreement with the experimental value of 2.949(6) D. The calculated value is still somewhat larger than experiment, as might be expected given the fact that we have used the bulk density of helium in this calculation, while it is expected that the local density around the HCN molecule will be somewhat higher than this [69]. The helium density that is needed to exactly reproduce the experimental result is 0.211 g/cm^3. The latter calculation assumes that the other parameters in the model are correctly chosen, while, in fact, the value of k used here is most likely too large, given the helium density distributions calculated by Viel and Whaley for HCN [69]. As a result, we do not feel that the specific values of the k and the effective density have much more significance than simple empirical parameters needed to reproduce the experimental results. Thus the correction method proposed here should be viewed as empirical, although based upon a physically reasonable model.

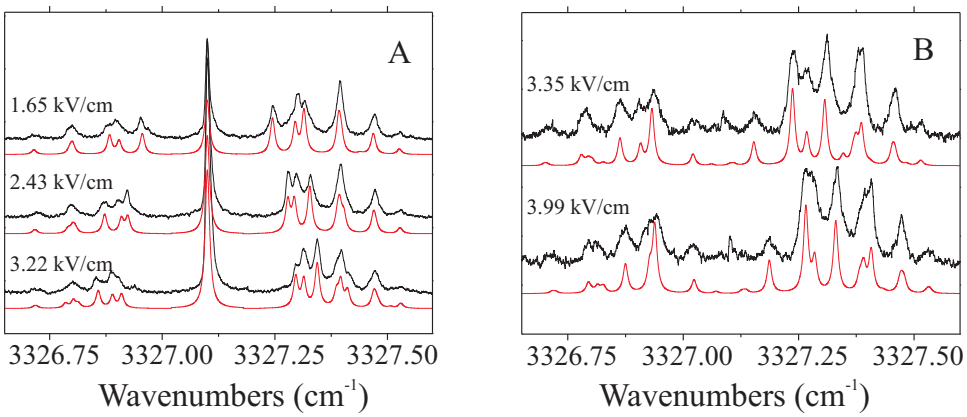

Figure 3.3: Series of Stark spectra of HCCCN in helium. The laser polarization was parallel for the spectra shown in (A), and perpendicular for the spectra in (B). The simulated spectra for each are shown just below the experimental and give an average value of 3.58 0.08 D and 3.65 0.08 D for the ground and vibrationally excited states, respectively.

3.5 HCCCN dipole measurements

The effects of the cavity geometry can be explored using another molecule, chosen here to be HCCCN. Figure 3.3 shows a series of Stark spectra for cyanoacetylene, taken at different fields and laser polarization directions (parallel and perpendicular).

The simulated spectra were generated using the same procedures discussed above for HCN and the resulting dipole moments for the ground and excited states are 3.58 ± 0.08 D and 3.65 ± 0.08 D, respectively. The gas phase dipole moment of cyanoacetylene in the ground state is accurately known [76], namely 3.73172 D. Here again, the effective dipole moment in helium is smaller than the gas phase value, the difference in this case being -0.15 D. The larger difference for cyanoacetylene, compared to HCN, is consistent with the above model, given that the aspect ratio for the associated cavity is larger for HCCCN. Using a k value of 4.46, determined from the van der Waals radii, the Higasi model gives i = -0.0689 D, using the bulk helium density. Using the enhanced helium density determined from the HCN experiment (0.211 g/cm^3), we calculate an induced dipole moment of i = -0.100 D, which reproduces the measured ground state dipole moment of HCCCN to within 1.5The fact that the model correctly predicts that the solvent effect for HCCCN is approximately double that of HCN gives it further support and suggests it can be used to correct for the (already small) helium solvent effect on molecular dipole moment measurements. The uncorrected and calculated dipole moments are summarized in Table 3.1.

It is interesting to note that the above model predicts that a polar oblate symmetric top

Table 3.1: Experimentally determined dipole moments in the gas phase (μ_{gas}) and helium droplets (μ_{He}), calculated induced dipole moments of the surrounding helium (μ_i), and sum of the gas phase dipole moments and induced dipole moments (μ_{He}). The first density (g/cm^3) is given in the literature15, and the second was adjusted to fit the HCN experimental dipole moment. Dipole moments are given in Debye.

	Experimental		Calculated	
	μ_{gas}	μ_{He}	μ_i	μ_{He}
HCN	3.0174	2.948(6)	-0.0473	2.970
HCCCN	3.73172	3.58±0.08	-0.0689	3.663

will show the opposite effect, namely a larger effective dipole than the isolated molecule. This is because the axial helium (which has an induced dipole that adds to that of the molecule) is closer to the molecule than the radial helium (opposing dipole). Unfortunately, a good candidate molecule for testing this prediction (having a vibrational band within the tuning range of our laser system) was not available.

3.6 Summary

The first conclusion we can draw from the above discussion is that the dipole moments of molecules solvated in helium are only slightly different from those of the corresponding gas phase molecules. Indeed, for the two molecules considered here the average differences are only 2.3 % and 4 %, respectively, for HCN and HCCCN. The Higasi model is in rather good agreement with the experimental results, indicating that the effective dipoles obtained from helium droplet experiments can be corrected with confidence to obtain those of the isolated molecules to better than 1.5 %. This is certainly sufficient to make quantitative comparisons with the results of theoretical calculations. These findings are important when it comes to applying Stark spectroscopy to the study of helium solvated molecules that have not been observed in the gas phase. Indeed, there are many species [64, 65, 66]that are seen in helium that are difficult or impossible to make in other ways.

Chapter 4

HCN-Mg binary complex

High-resolution infrared spectra are reported for two isomers of the magnesium-HCN binary complex, corresponding to the magnesium bonding at the nitrogen and hydrogen ends of the molecule. Stark spectra are also reported for these complexes, from which the corresponding dipole moments are determined. Ab initio calculations confirm that the potential energy surface has two minima, consistent with the experimentally determined structures. The wavefunctions of the 2D intermolecular CCSD(T) potential energy surface, calculated with the collocation method, are also reported for the magnesium-HCN system and are used to calculate the vibrationally averaged dipole moment for both isomers, which are then compared to experiment.

4.1 Introduction

The quest for a fundamental understanding of the interactions between molecules and metals has been a dominant theme in surface science for many years. Towards this end, numerous experimental and theoretical studies have provided important insights into the metal-adsorbate bond [83, 84, 85, 86, 87, 88, 89, 90, 91, 92]. In parallel with these studies, cluster science is providing methods for investigating the size dependence of these properties [93, 94]. Indeed, understanding the development of bulk, metallic properties as the cluster size increases is a subject of considerable current interest [95, 96]. In the context of nanoscience, this approach also promises to reveal properties of finite systems that are distinctly different from those of the bulk metal [97]. Detailed comparisons between theory and experiment for these finite systems are providing fundamental insights into the corresponding interactions and might ultimately provide a more fundamental understanding of the reaction dynamics on bulk metals [98].

The field of metal cluster science is far too extensive to be reviewed here and we simply note that considerable progress has already been made towards this ultimate goal [99, 16, 5, 100, 101]. Although a single metal atom/adsorbate system is certainly a very poor model for the corresponding metal surface - adsorbate, detailed studies of these binary complexes are of interest in their own right. In particular, they provide an important contrast with which the bulk interactions can be compared. Unfortunately, the number of detailed structural studies of such systems is still quite limited. Recent progress has been made in this direction by Gerry and co-workers, using microwave spectroscopy, for such systems as Pt-CO [102]. In these studies, laser vaporization was used to produce a platinum vapor that was co-expanded into vacuum with CO. Fourier -Transform microwave spectroscopy was then used to measure the pure rotational spectrum of several of the isotopomers of the resulting binary complex. These studies can provide detailed information on the bond lengths in these species, providing benchmarks for comparison with ab initio theory. These binary complexes have qualitatively different interactions (in particularly, they are much more weakly bound) than stable inorganic metal complexes, which have also been studied by microwave spectroscopy [103].

Infrared spectroscopy has been used extensively in the study of adsorbates on surfaces [104, 105, 106] and it is therefore surprising to find how little corresponding data exists for adsorbate-metal clusters, particularly those involving more than one metal atom. In a recent paper [66] we reported a new approach for preparing metal cluster-adsorbate complexes and characterizing them using high-resolution infrared spectroscopy. The approach involves forming the complexes in the nearly ideal spectroscopic medium of helium nanodroplets [28, 19, 64, 107, 108, 17]. The previous study gave preliminary data for HCN bound to magnesium clusters containing up to three atoms. In all cases, we observed the formation of complexes in which the HCN adsorbs to the metal with the nitrogen end "down". Rotational fine structure was resolved in these infrared spectra, providing detailed information on the cluster structure.

In the present chapter, a more detailed investigation of the HCN-Mg system is presented. The corresponding potential energy surface reported here has two minima, with the magnesium atom binding to either end of the HCN. A more extensive spectral search revealed that both of these isomers are formed and stabilized in the helium droplet environment. The ability of helium to stabilize higher energy isomers has been demonstrated previously in our group [64]. This can be understood by noting that the condensation energy released during the growth process, which would normally remain in the newly formed complex, is quickly relaxed to the helium matrix. As a result, the system can easily become trapped in a local

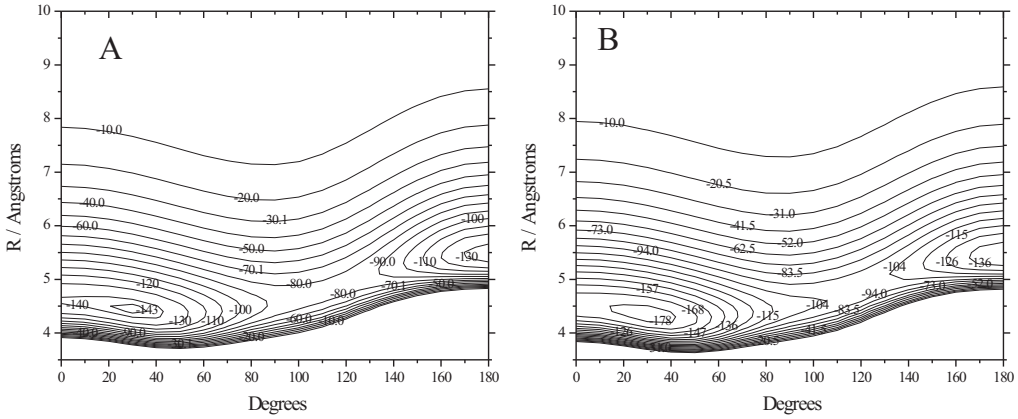

Figure 4.1: Potential energy surfaces for the HCN-Mg binary complex. A and B correspond to the CCSD(T) and MP2 surfaces, respectively.

minimum on the potential energy surface, corresponding to the stabilization of a higher energy isomer. Stark spectra are also reported for the two isomers, providing accurate dipole moments. Comparisons with the ab initio calculations are done by vibrationally averaging the calculated dipole moment function using wavefunctions obtained from a collocation calculation [109], based upon the ab initio HCN-Mg potential energy surface.

4.2 *ab initio* calculations

In light of our previous work on the binary HCN-Mg complex [66], we carried out ab initio calculations for this system at both the CCSD(T) and MP2 levels using MOLPRO [110]. All of the results presented here were obtained using the 6-311++G(3df,3pd) basis set. Basis set superposition error was taken into account using counterpoise correction methods [111]. For the purposes of generating the intermolecular potential surface, the HCN was treated as rigid, with the HCN bond lengths fixed at values calculated from a full CCSD(T)/6-311++G(3df,3pd) geometry optimization of HCN. The Jacobi coordinate system has its origin at the center of mass of the HCN and is defined such that $\theta = 0$ corresponds to the linear HCN$\cdots$Mg complex. Calculations were carried out at 10 radial points (between 3 and 9 Å), and at 12 Gauss-Legendre quadrature angles between 0 to 180 degrees.

The resulting potential energy surfaces are shown in Figure 4.1. Qualitatively the two surfaces are similar, both of them having two minima, corresponding to the magnesium

binding to the hydrogen or nitrogen end of the molecule. The global minimum on both surfaces corresponds to the magnesium binding to the nitrogen end, with the secondary minimum corresponding to the hydrogen bonded complex. In the latter case the minimum is in the linear configuration, while for the nitrogen bound isomer the global minimum corresponds to a bent structure. However, the energy in the corresponding linear geometry is only 3 cm^{-1} above the minimum (CCSD(T)), suggesting that the amplitude of the bending motion will be large and the vibrationally averaged structure will be essentially linear. Note that the energy difference between these two minima is only 13 cm^{-1} on the CCSD(T) surface, while it is 42 cm^{-1} on the MP2 surface. We assume that the CCSD(T) surface is the more accurate of the two.

Since the amplitude of the intermolecular bending is expected to be large, comparisons between the experimental and calculated properties requires that the latter be vibrationally averaged. To this end, we also calculated the MP2/6-311++G(3df,3pd) dipole moment surface using MOLPRO (MOLPRO manual section 4.13). This enabled us to calculate the vibrationally averaged dipole moment based on the CCSD(T) potential energy surface for comparison with experiment.

In addition to the potential energy surfaces presented above, we calculated fully optimized geometries for both minima. The resulting structures are summarized in Table 4.1. The MP2 level dipole moments and vibrational frequency shifts (harmonic approximation) were also calculated for the two isomers and are reported in Table 4.2.

4.2.1 Electron difference density calculations

The concept of electron difference densities, sometimes called deformation densities, has existed for some time [112]. In its normal application, it involves taking the difference between the electron density of a molecule, and the densities of a set of non-interacting atoms in the same geometrical arrangement. By looking at the changes in the density between the two cases, one can gain insight into the nature of the intramolecular bonding. Indeed, this approach provided the framework for the scheme for determining atomic charges developed by Hirshfeld [112]. For application to the magnesium-HCN complexes studied in this work, we have extended the concept to study intermolecular bonding. By subtracting the densities of non-interacting fragments from the density of the whole complex, the interactions between the molecules are highlighted in the resulting difference density map. In particular, properties such as induced dipole moments and charge transfer can be directly calculated from the difference densities by taking the appropriate integrals. In what follows we describe the salient features of this approach as it applies to the current problem, and present the

Table 4.1: Calculated Bond Lengths (Å), Bond Angles (degrees) and Rotational Constants for HCN, HCN-Mg and Mg-HCN using the 6-311++G(3df,3pd) Basis Set.

	Method		
	MP2	CCSD(T)	exp
HCN			
C-H	1.0653	1.0680	1.06501
C-N	1.1656	1.1592	1.15324
HCN$\cdots$Mg			
C-H	1.0655	1.0683	
C-N	1.1659	1.1592	
N-Mg	3.7782	3.9011	
C-N-Mg	144.05	150.20	
H-C-N	179.940	179.997	
B″	0.0690	0.0642	
Mg$\cdots$HCN			
C-H	1.0668	1.0695	
C-N	1.1660	1.1594	
N-Mg	3.6045	3.6306	
C-N-Mg	180.0	180.0	
B″	0.0465	0.0461	

Table 4.2: A summary of the experimental and calculated MP2/6-311++G(3df,3pd) molecular constants for the two isomers of HCN-Mg. The calculated values are all for the equilibrium structures of the complexes. Note that the rotational constants in helium are much smaller than the ab initio values, as expected (see text). μ_c is the experimental dipole moment corrected for the effects of the helium solvent: i.e. representative of the gas phase value.

	Exp	MP2
HCN$\cdots$Mg		
Δ /cm^{-1}	1.86	2.63
B$''$ /cm^{-1}	0.02861	0.0690
B$'$ /cm^{-1}	0.02851	—
D$''$ /cm^{-1}	2.48 x 10^{-5}	—
D$'$ /cm^{-1}	2.05 x 10^{-5}	—
μ / D	3.23 $\pm$ 0.05	3.646
μ_c / D	3.33 $\pm$ 0.05	—
Mg$\cdots$HCN		
Δ /cm^{-1}	29.6	25.65
B$''$ /cm^{-1}	0.0095	0.0465
μ / D	3.2 $\pm$ 0.5	3.690
μ_c / D	3.3 $\pm$ 0.5	—

results.

The procedure used for generating the difference densities was as follows. First, a geometry optimization was performed for the complex and the electron density was saved. A single point electron density calculation was then performed for each fragment using the geometry and full basis set from the optimized complex; this was achieved by alternatively "dummying out" the atoms in the fragments not being calculated. This "dummying" was done to minimize the effects of basis-set superposition error, as in the counterpoise correction scheme of Boys and Bernardi [111]. Finally, the fragment densities were added together to make a single reference density, which was then subtracted from the density of the complex to generate the difference densities.

The geometry optimization and electron density calculations were done at the BCCD(T) / 6-311++G(3df, 3pd) level using the MOLPRO 2000 ab initio package [110]. Since the true BCCD(T) densities were not available from the program, we used the "optimized" single determinant BCCD density, determined according to the "Brueckner Orbital expectation value" (BOX) scheme of Hesselmann and Jansen. [113] Those authors have recently shown that this type of single determinant coupled-cluster density, while not the true density, does contain some information about the electron correlation, and gives improved values for

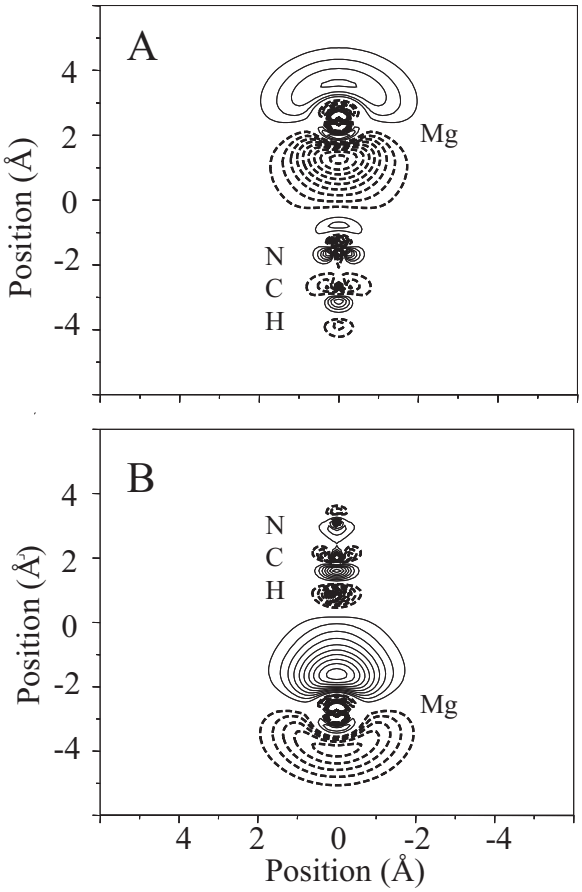

Figure 4.2: Electron difference density plots (see text) for (A) the N-bound and (B) the H-bound isomers of the magnesium HCN complexes. Solid and dashed contours are used to indicate positive and negative values of the electron difference density, respectively. The contours are spaced at 0.006 e/Å^3 intervals, with the absolute value decreasing from outermost contour of 0.0008 e/Å^3

one-electron properties [113] and intermolecular interaction energies [114], compared to the Hartree-Fock density.

Figure 4.2 shows difference density plots for the linear nitrogen-bonded HCN-Mg complex (A) and for the hydrogen-bonded Mg-HCN complex (B). Although the minimum for the N-bound isomer is actually bent, we have chosen the linear geometry here for ease of comparison; in any case, the energy difference between the bent and linear geometries on the PES is small (3 cm^{-1}). On each plot, solid contours are used to represent areas where the density is increased in the complex, relative to the fragments, while dashed lines represent areas of decreased density.

In both cases it is clear that the dominant feature in the difference density is the polar-

ization of the magnesium atom. As one would expect, there is a strong induction interaction between the dipole moment of the HCN and highly polarizable electron cloud of the Mg. The induced dipole on the Mg atom changes sign between the H-end and N-end of the HCN, consistent with our expectations. Another thing that is clear from the plots is that these induced dipoles are quite delocalized, indicating that the normal point dipole approximations may not be appropriate. Instead, the induced dipole moment of the entire system can be precisely calculated by multiplying the difference density by the appropriate component of the dipole operator and integrating over all space. This was done for the difference densities in Figure 4.2 using 3D Romberg integration implemented by adapting appropriate algorithms from Numerical Recipes [115]. The induced dipoles calculated by this method are 0.67 D and 0.75 D for the H-end and N-end geometries, respectively. For purposes of comparison, the dipole moments were calculated for both of these geometries and for the HCN monomer at the BCCD(T) level using the method of finite differences, (MOLPRO manual section 24.4). The results are 3.74 and 3.63 Debye for the N-end and H-end complexes respectively, and 2.997 for HCN monomer. Subtracting the latter value from the former two yields 0.636 and 0.744 for the induced dipoles, in good agreement with the values calculated from the difference density. This is one indication that the BOX approach for calculating the difference densities is reliable for these complexes.

Another point that is clear from the difference density plots is that there must be significant p-character mixed into the valence orbitals of the magnesium. The fact that the p-orbitals are energetically available for mixing into the ground state wavefunction is consistent with chemical intuition. Indeed, the magnesium atom is only closed sub-shell, so the 3p orbitals are fairly low-lying. This has been demonstrated previously by Kaplan et al., who showed that there was significant p-orbital character in small Mg clusters, and even a small amount in the free atom [116]. The availability of these p-orbitals explains, at least qualitatively, the large polarizability of Mg atoms, which is the key point for understanding their interactions.

4.3 Nitrogen bound complex

The rotationally resolved spectrum of the nitrogen bonded HCN-Mg complex has been reported previously [66], but is shown here for completeness (Figure 4.3), along with a fit to a linear rotor Hamiltonian. The molecular constants obtained from this fit are summarized in Table 4.1. The primary reason for assigning this spectrum to the nitrogen-bonded complex is that the C-H stretch is only slightly shifted from the HCN monomer in helium [64]. As

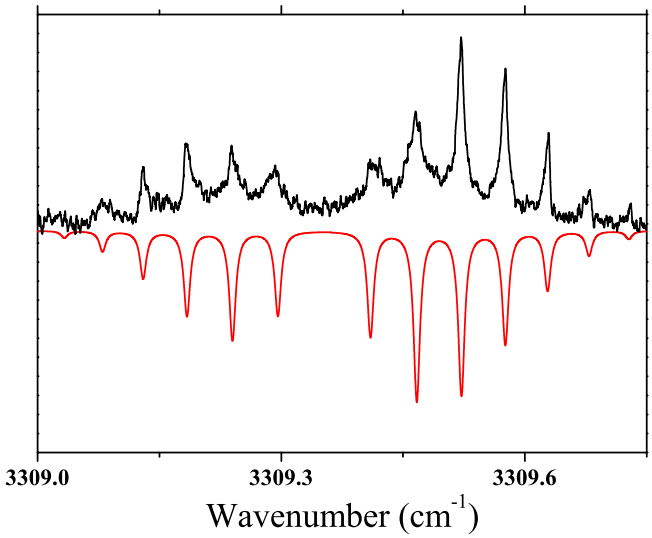

Figure 4.3: A rotationally resolved spectrum of HCN-Mg. The calculated spectrum corresponds to a fit to a linear molecule Hamiltonian with the intensities corresponding to a rotational temperature of 0.37 K. Rotational constants are summarized in table 4.2

shown in the ab initio calculations reported in Table 4.2, the frequency shift for the hydrogen bonded complex is predicted to be much larger (-25.65 cm^{-1}) than that observed for this complex. Indeed, the agreement between the experimental (measured in helium droplets) and calculated frequency shifts, relative to the HCN monomer, is quite good for the nitrogen-bonded isomer, namely -1.86 cm^{-1} and -2.63 cm^{-1}, respectively. It is important to note that we have not explicitly taken the helium into account when calculating the vibrational shifts for either of the complexes we report here. Although the effects of the helium are not known for this particular system, our previous work on other systems [117] leads us to expect that they are minor. The dependence of the signal intensity on the HCN pressure in the pick-up cell confirmed that this complex contains a single HCN molecule. In addition, the signals varied with magnesium oven temperature in a manner that confirmed this species contains a single magnesium atom.

As shown in previous studies [35], rotational constants obtained from helium droplet spectroscopy are smaller than those of the corresponding isolated molecule. Since the latter are not available for this complex, we compare the helium results with those of the ab initio calculations. Using the results from Table 4.2, we obtain a ratio between the gas (ab initio calculated) and helium droplet rotational constants of 2.41. This is typical of molecules

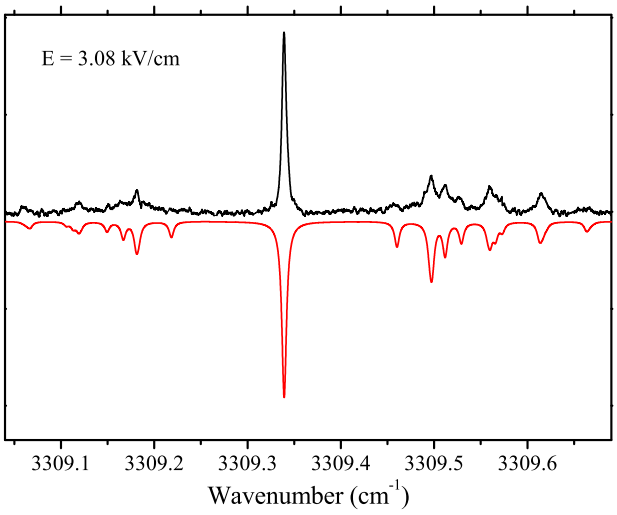

Figure 4.4: The Stark spectrum of HCN-Mg recorded at a field of 3.08 kV/cm. The calculation of the simulated spectrum is based on the diagonalization of the full Stark Hamiltonian matrix.

that have small rotational constants (< 1 cm^{-1}) [118] where rotation is sufficiently slow to enable the helium atoms to follow the molecular motion. Thus, although the rotational constant cannot yet be used to obtain accurate bond lengths, in the absence of a quantitative model that includes the effect of the helium, it does provide further evidence that this spectrum is properly assigned to the HCN-Mg complex. It is evident from Figure 4.3 that the widths of the various P and R branch transitions in the spectrum are quite different. This is also quite common in helium droplet spectroscopy and is the result of the fact that the inhomogeneous broadening is dependent upon the rotational state of the molecule. A dramatic illustration of this point comes from our previous study of HCN in helium [59] where we observed a splitting of the R(0) transition that was interpreted as arising from the anisotropic interactions between the HCN and the helium. This anisotropy gives rise to effects that are similar to those resulting from the Stark effect (although the detailed form of the Hamiltonian is different) [71], which are known to be highly dependent upon the rotational quantum number [119]. The spectrum shown in Figure 4.3 was recorded in rather large helium droplets in an attempt to minimize these effects. Spectra recorded for smaller droplets showed even broader line widths, to the point where the R(0) and P(1) transitions were no longer resolved.

The dipole moment of the HCN-Mg complex was determined by applying an external electric field to the interaction region, as discussed above. Figure 4.4 shows the spectrum of HCN-Mg recorded at an applied electric field of 3.08 kV/cm. At higher electric fields the entire spectrum collapses into the field induced Q branch, leaving very little spectral character with which to fit the dipole moment. At this modest field the higher R and P branch transitions are still visible, although strongly perturbed, along with the field induced Q branch near the band origin. The relative intensities and shifts of these features in the spectrum can be fit to the dipole moment, assuming that the applied electric field is calibrated. The field was calibrated by recording a gas phase molecular beam Stark spectrum of HCN in the same apparatus. Since the dipole moments of HCN are known in both the ground and vibrationally excited states [75], the corresponding Stark spectrum can be used to determine the field strength. The rotational constants obtained from the field free spectrum can then be used to calculate the spectrum in the presence of the field. The calculated spectrum shown in Figure 4.4 was obtained by fitting to a single parameter, namely the dipole moment. Four additional spectra were recorded at fields of 2.04 KV/cm, 1.70 KV/cm, 1.04 KV/cm and 0.745 KV/cm and fit independently. Within the experimental uncertainty, the ground and vibrationally excited state dipole moments were found to be the same, 3.23 0.05 D. In a separate study [120], we showed that the dipole moments measured in helium droplets are somewhat smaller than those of the gas phase molecule. We attributed this decrease in the dipole moment to be due to shielding of the solvated electric dipole moment by the induced dipole moment of the surrounding helium atoms and quantitatively accounted for it by assuming the molecule resides within an elliptical cavity inside the helium droplet. Using this model we calculate a corresponding correction to the measured dipole moment of 0.0993 D, yielding a gas phase dipole moment of 3.33 0.05 D. This value is still considerably smaller than the ab initio equilibrium dipole moment (3.646 D). As we will show below, we attribute this difference to vibrational averaging.

4.4 Hydrogen-bound Mg-HCN complex

As noted above, the Mg-HCN isomer is predicted to have a much larger frequency shift. This is reasonable given that the hydrogen is directly involved in the formation of the intermolecular bond. Using the ab initio frequency shift as a guide, we carried out a search for the hydrogen-bonded isomer. Since this isomer is not as strongly bound as the nitrogen bonded one ($\Delta E_{CCSD(T)} = 13$ cm^{-1}), we would not expect to observe the higher energy isomer if the system were in equilibrium at the droplet temperature (0.37 K). Indeed, even

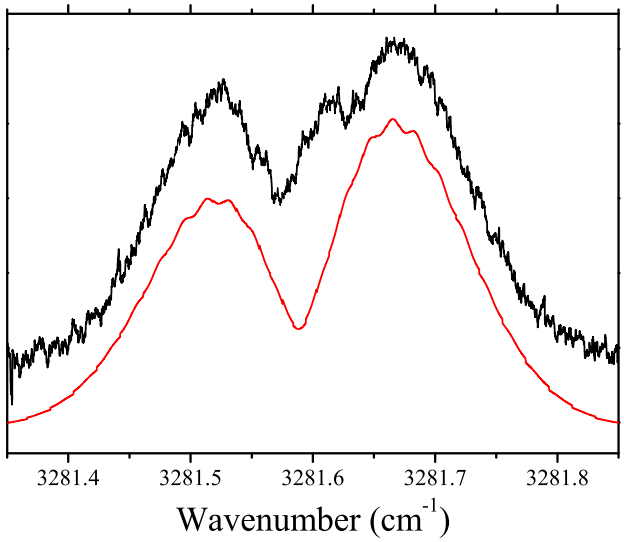

Figure 4.5: A zero field spectrum of Mg-HCN. Rotational fine structure is not observed in the spectrum, presumably due to rapid vibrational relaxation for this hydrogen bonded complex. The estimated rotational constant comes from the separation between the P and R branches, given that the droplet temperature is known.

in free jet expansions where the temperatures are typically an order of magnitude higher than that of the droplets, higher energy isomers are often not observed. As noted above, the growth of clusters in helium is a highly non-equilibrium process. In particular, a magnesium atom approaching the HCN from the hydrogen end may get trapped in the associated local minimum and not be able to surmount the barrier between it and the global minimum.

Figure 4.5 shows the spectrum of a species containing one magnesium and one HCN (based upon the HCN pressure and magnesium oven temperature dependence of the signals) that is in the region of the spectrum consistent with the calculated frequency shift (-25.65 cm^{-1}) for the hydrogen bound isomer. Indeed, this spectrum optimized under the same conditions as used in the HCN-Mg experiments reported above. Fits to the field free, Stark and pendular spectra of this species yield an experimental frequency shift from the HCN monomer of -29.6 cm^{-1}. The experimental shift is somewhat larger than that obtained from the ab initio calculations. This difference may not be entirely due to deficiencies in the calculations, given that we have observed helium induced red shifts of a few wavenumbers for other hydrogen bonded complexes, such as $(HCN)_2$. [59] It should be noted that the structure observed in the R branch is reproducible and may be the result of the relatively

strong perturbation of the low J states of the complex by the helium, as seen for several other species [56].

As is typical for excitation of vibrational modes that are directly coupled to an intermolecular bond11903, the transitions are rather broad, compared to those of the free stretch. This is most likely due to the fact that vibrational relaxation is fast when the vibrational mode is directly coupled to the intermolecular bond, giving rise to substantial homogeneous broadening. Fortunately, we know the temperature of the helium droplets (0.37 K [39]) so that the separation between the P and R branches can be used to obtain an estimate of the corresponding rotational constant. The calculated spectrum shown in Figure 4.5 was obtained with a rotational constant of 0.0095(5) cm^{-1} and a Lorentizian line width of 0.02 cm^{-1}. Using the ab initio rotational constant of the Mg-HCN complex (0.0465 cm^{-1}) as the gas phase value, the resulting ratio with the helium value is 4.9. Although this ratio is larger than that obtained above for the other isomer, this is not the only system for which such a large ratio was observed [121]. Although progress is being made in understanding the influence of the helium on the rotational constants of molecules [35, 69], a quantitative theory is still lacking, hence the best we can do is make this qualitative comparison.

We now turn our attention to the determination of the dipole moment of the hydrogen-bonded isomer. The low resolution obtained for this isomer would preclude the determination of the dipole moment using conventional Stark spectroscopy, based on the measurement of the field induced splitting of individual rotational transitions. However, the present scheme relies on the field dependence of the Q branch and a much more substantial change in the overall shape of the P and R branches. As a result, dipole moment measurement can be carried out even under these conditions. Figure 4.6 shows a Stark spectrum of this complex, obtained at a vacuum field of 3.14 kV/cm. The line width in the calculated spectrum was determined from the width of the Q branch in the experimental spectrum, namely 0.02 cm^{-1}. Fits to the experimental spectra recorded at fields of 3.14, 2.40, 1.76 and 1.40 Kv/cm, yielded a dipole moment for the hydrogen bonded isomer of 3.2 $\pm$ 0.5 D. Correction for the solvent effect yields 3.3 $\pm$ 0.5 D, compared to the ab initio equilibrium dipole moment of 3.690 D. This significant difference is addressed in the next section, where we show that the effects of vibrational averaging are significant.

4.5 Vibrational averaging

The discrepancies between the ab initio and experimental dipole moments are significant for both isomers. The experimental dipoles are both smaller than the equilibrium ones,

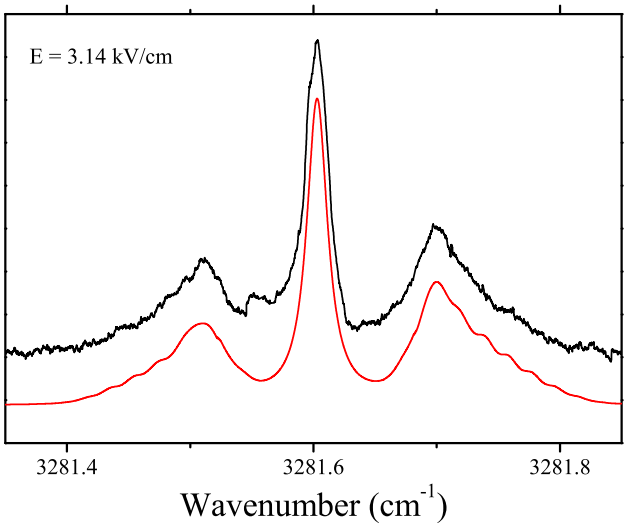

Figure 4.6: Stark spectrum and simulation of Mg-HCN, recorded at a field of 3.14 kV/cm.

which is most likely due to vibrational averaging. Indeed, the effects of vibrational averaging have been observed for many other systems [122, 123, 124, 125, 126]. For an atom-linear molecule system of the type considered here this averaging should be performed on the 2-D intermolecular potential, since the stretching and bending motions are generally coupled. A number of methods are available for calculating the bound state wave functions for such systems [127, 128, 129]. In the present study we chose to use the collocation method [109] to solve the bound state problem in two dimensions. The computer code used in these calculations is a modified version of that used in previous studies of Ar-C_2H_2 [130, 131].

The bound state calculations were carried out using the CCSD(T)/6-311++G(3df,3pd) BSSE corrected potential energy surface discussed above. This potential energy surface was interpolated to match the collocation points using a bicubic spline algorithm. The wavefunctions determined from the collocation method were then used to determine the vibrationally averaged dipole moment using the ab initio MP2/6-311++G(3df,3pd) dipole moment surface. The appropriate wavefunctions, along with their corresponding eigenvalues, are shown in Figure 4.7. Four states lie below the -80 cm^{-1} contour, corresponding to the barrier separating the two minima. These wavefunctions are completely localized on either the nitrogen or hydrogen ends of the HCN. Clearly, the anisotropic barrier between these two minima is sufficiently high to give rise to two, essentially independent, isomers. The first and fourth wavefunctions are clearly assigned as, respectively; the ground state of the

nitrogen bound isomer and the "ground state" of the hydrogen bound isomer. The bound states above the -80 cm^{-1} contour sample both minima, as illustrated by the fact that the wavefunctions are delocalized over both wells.

Table 4.3 contains the calculated values of $\langle R_{cm} \rangle$, $\overline{B}$, $\langle P_1(\cos\theta) \rangle$ and $\langle P_1(\cos\theta) \rangle$ for the ground states of the two HCN-Mg isomers. The large anharmonicity associated with the ab initio intermolecular potential yields a calculated value of for the Mg-HCN complex of 3.78 , 0.17 $\mathring{A}$ larger than the equilibrium geometry. Similarly $\langle R_{Mg-N} \rangle$ is calculated to be 3.97 $\mathring{A}$ for the HCN-Mg complex, an increase of 0.19 $\mathring{A}$ compared to R_e. The effective rotational constants, $\overline{B}$, listed in the table, were calculated using the pseudodiatomic approximation for the moment of inertia of the complex, namely; [132]

$$I_{HCN-Mg} = \mu_d \langle R_{cm} \rangle^2 + \frac{1}{2} I_{HCN} [1 + \langle cos^2\theta \rangle] \tag{4.1}$$

where μ_d is the reduced mass.

The vibrationally averaged dipoles reported in Table 3 were calculated using:

$$\langle \mu_{HCN-Mg} \rangle \cong \frac{\sum \psi \mu \psi \sin\theta}{\sum \psi \psi \sin\theta} \tag{4.2}$$

where ψ the ground state wave function points for HCN-Mg and Mg-HCN (Figure 4.7) and μ is the projection of the ab initio dipole moment onto the A axis of the complex. As expected, the vibrationally averaged dipole moments are considerably smaller than the equilibrium values. In fact, the measured dipoles (in helium) are slightly smaller than the vibrationally averaged values. For the hydrogen bonded isomer the errors in the experimental measurements are sufficiently large to preclude meaningful interpretation of this difference. It is interesting to note, however, that measurements we have made of the HCN dipole moment in helium, where comparisons with the gas phase values can be made, indicate that the effect of the solvent is to give a slightly smaller dipole than in the gas phase [56], due to the anisotropic polarization of the surrounding solvent [79]. If we assume the HCN-Mg complex occupies an elliptical cavity within the helium droplet, the measured dipole moment can be corrected by including the sum of the induced dipole moments of the helium directly surrounding the helium. Using the elliptical shape factor k = 5.37, determined from the calculated vibrationally averaged bond lengths and the van der Waals radii, a helium density of 0.211 g/cm^3 [120], and the molar polarizability of helium (0.123296 cm^3/mole)13721, we calculate a correction of 0.0993 D to be added to the measured dipole moments. Thus the dipole moments provide further convincing evidence for the assignment of the present spectra to the HCN-Mg and Mg-HCN binary complexes.

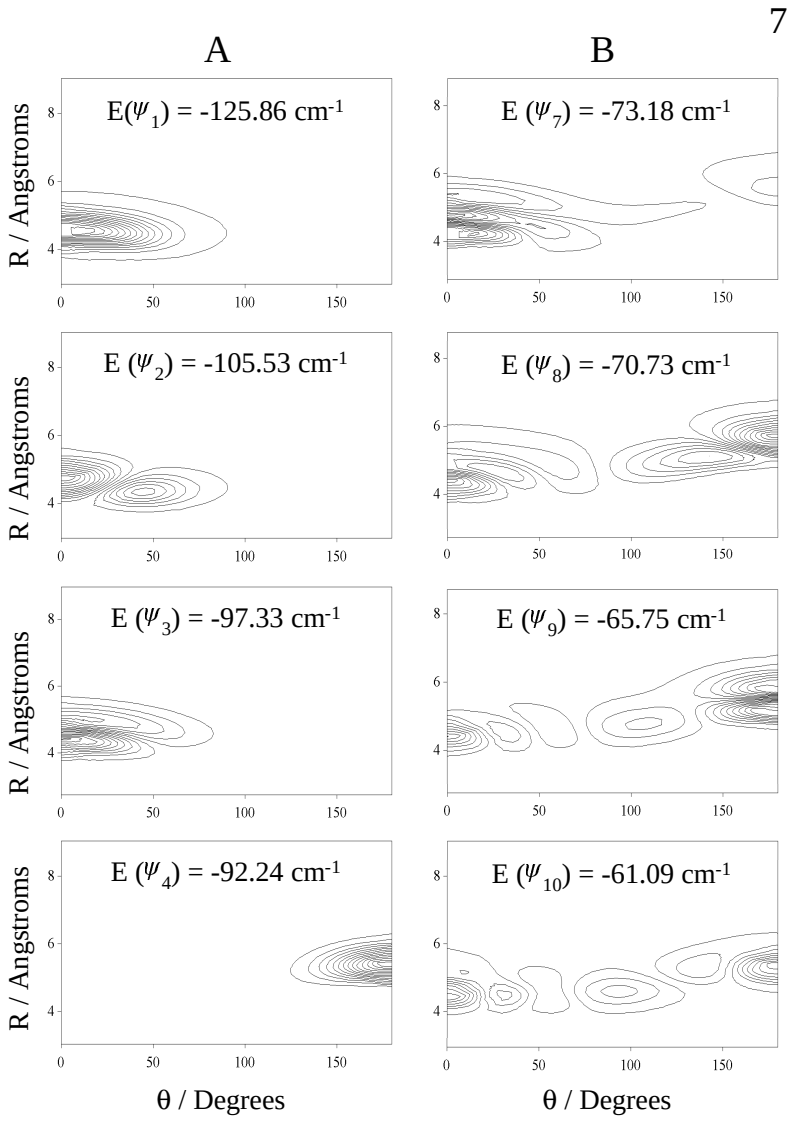

Figure 4.7: Contour plots of (A) the first four intermolecular vibrational state wavefunctions of the HCN-Mg complex, namely (ψ1) the ground state, (ψ2) the first excited bending state, (ψ3) the first excited stretching state, and (ψ4) the ground state of the hydrogen bound Mg-HCN complex. Contour plots of (B) four states that are delocalized over the two wells.

Table 4.3: The results from vibrationally averaging the ab initio results.

	$\langle R_{cm} \rangle$	$\overline{B}$	$\langle P_1(\cos\theta) \rangle$	$\langle P_1(\cos\theta) \rangle$	$\langle\ \mu\ \rangle$
HCN-Mg	4.57	0.0614	0.926	0.800	3.293
Mg-HCN	5.41	0.0441	-0.966	0.903	3.336

4.6 Summary

The experimental and theoretical results presented here give unambiguous evidence for the formation of two isomers of magnesium-HCN, corresponding to the magnesium binding to the hydrogen and nitrogen ends of the molecule. In both cases, the binding is weak, corresponding to van der Waals like interactions. These systems are clearly far from the chemisorption regime, as would be expected from everything that is know about the nature of the interactions of magnesium atoms[133, 116, 134, 135]. Electron difference densities were calculated and reveal simple induction, with no charge transfer between the HCN and magnesium. Calculations of the vibrationally averaged dipole moments for both isomers are in good agreement with measured dipole moments. Here again, the dipole moments of these complexes are well described by the induced dipole on the highly polarizable magnesium atom by the highly polar HCN. These results provide an interesting backdrop for future studies of HCN bound to larger magnesium clusters, which show highly non-additive behavior, much stronger binding, and evidence of charge transfer[73].

Chapter 5

HCN-Mg_n (n = 2-6) complexes

High-resolution infrared laser spectroscopy has been used to determine the structures of HCN-Mg_n complexes formed in helium nanodroplets. The magnesium atoms are first added to the droplets to ensure that the magnesium complexes are preformed before the HCN molecule is added. The vibrational frequencies, structures and dipole moments of these complexes are found to vary dramatically with cluster size, illustrating the non-additive nature of the HCN-magnesium interactions. All of the complexes discussed here have the nitrogen end of the HCN pointing towards the magnesium clusters. For Mg_3, the HCN binds to the "three-fold" site, yielding a symmetric top spectrum. Although the HCN-Mg_4 complex also has C3v symmetry, the HCN sits "on-top" of a single magnesium atom. These structures are confirmed by both ab initio calculations and measurements of the dipole moments. Significant charge transfer is observed in the case of HCN-Mg_4, indicative of charge donation from the lone pair on the nitrogen of HCN into the LUMO of the Mg_4.

5.1 Introduction

Interactions between molecular adsorbates and metal surfaces are of fundamental importance in many fields of science, including catalysis and corrosion, accounting for the extensiveness of the associated literature [136, 137, 138, 139, 140, 141, 142, 143, 144, 145, 146, 147, 148]. These interactions are known to be strongly dependent upon the crystal face and defect density, illustrating the importance of the local structure of the metal atoms. Metal cluster science provides us with the additional variable of size, which is of particular current interest given the unique properties that metals can have on the nanometer scale [149, 150]. Although the interest in metal clusters [5] is, in part, fueled by the idea that they serve as finite [151, 4] model systems for bulk metal surfaces [152, 153, 145, 146, 147, 148], it

is now well known that the properties of nanoscale materials can be qualitatively different from their bulk counterparts [154, 151, 155, 12], suggesting whole new approaches for the design of nanomaterials with novel properties. Consider, for example, the properties of small gold nanoparticles on metal oxide surfaces [12]. Despite the low reactivity of the bulk metal, these systems are known to display strong catalytic activity, particularly in the low temperature oxidation of CO [12]. Considerable experimental and theoretical [10, 12] work has focused on obtaining a molecular level understanding of the associated processes. The catalytic activity of these systems depends strongly upon the defect density at the metal oxide surface [12], prompting theoretical work suggesting that charge donation from F-centers in the metal oxide to the gold nanoparticles (n=8-20 atoms) is at least partially responsible for the enhanced reactivity [12]. These theoretical calculations show that the eight-atom cluster is the smallest one for which significant charge transfer occurs. The sudden onset of charge transfer, with increasing cluster size, is understood in terms of qualitative changes in the electronic structure of the metal cluster. In view of the potential of this approach for the design of new catalysts, there is clear need for new methods for studying the related phenomena.

We report here a study of the size dependence of the structure and polarity of isolated magnesium clusters, to which are bound a single HCN molecule. The premise upon which we compare these systems with the gold nanoparticle-metal oxide systems discussed above is based upon the hypothesis that a strong base might play the role of the F-center, through the donation of electron density to the metal cluster. Although HCN is not a strong base, the present study does show that there is a sudden onset of significant charge transfer with cluster size, at n=4. The experimental method is based upon a new approach developed in our laboratory for determining metal cluster structures from infrared laser spectroscopy [66]. The clusters of interest are grown in helium nanodroplets, a nearly ideal spectroscopic matrix [17, 18, 19]. The homogeneous and non-dissipative nature of the helium solvent results in infrared spectra that are rotationally resolved, from which we can obtain detailed structural information. Stark spectroscopy can also be performed, providing a probe of the extent of charge transfer between the metal complex and the adsorbate molecule. Although we will repetitively refer to the magnesium clusters studied herein as metal clusters, it is important to point out that in this size range they are not metallic [156].

Although infrared spectroscopy has been used extensively in the study of adsorbed molecules on metal surfaces [157], analogous experiments on metal clusters are sparse [15, 16]. In fact, while rotationally resolved spectra have been obtained for a few molecules bound to single metal atoms [102], the corresponding results for metal clusters have not been forth-

coming. The experiments reported here are therefore quite unique, providing us with a new approach for studying these interesting and important systems. Although the focus of the present study is on magnesium clusters, the method is quite general and can be applied to other metals, including gold.

5.2 Experimental

The nozzle was operated at a pressure of approximately 60 bar and temperatures between 23.5 and 17 K. The droplets formed under these conditions have means sizes in the range from 1,000 to 8,000 atoms, respectively [48, 45]. Magnesium atoms were doped into the droplets by passing the latter through a 1.3 cm long oven, operated at a range of temperatures near 350 C (10^{-5} mbar of magnesium) [158], monitored using a J-type thermocouple, depending upon the desired metal-cluster size. The HCN was added downstream of the metal oven in a separate pick-up cell, the pressure of which was optimized for the pick-up of a single molecule. All of the results presented here are consistent with the metal cluster having been formed before the HCN molecule is introduced into the droplet, implying that the time for the metal atoms to find one another within the droplets is short with respect to the flight time between the two pick-up regions.

An electric field could be applied to the laser interaction region using two metal electrodes. A considerable enhancement of the signal levels was obtained by using a large electric field (24 kV/cm) to record pendular spectra [60, 61], which was particularly useful when searching for new species. At more modest electric fields [78] (1-4 kV/cm) the resulting Stark spectra provided an accurate measure of the dipole moments of the HCN-Mg_n complexes.

5.3 *Ab initio* calculations

Extensive ab initio calculations were carried out for both the free magnesium complexes and for HCN-Mg_n. The calculations reported here were carried out using MOLPRO [110], with the 6-311++G(3df,3pd) basis set, at both the MP2 and BCCD(T) levels. Energy convergence and gradient step sizes were set to 10^{-7} and 10^{-5} Hartrees, respectively. The binding energies reported here include the counterpoise correction [111]. The MP2 vibrational frequency shifts were determined by subtracting the harmonic frequency of the C-H stretch in the complex from that of the HCN monomer, calculated using the same level of theory and basis set. Tables 5.1 and 5.2 and Figure 5.1 provide a summary of the ab initio results.

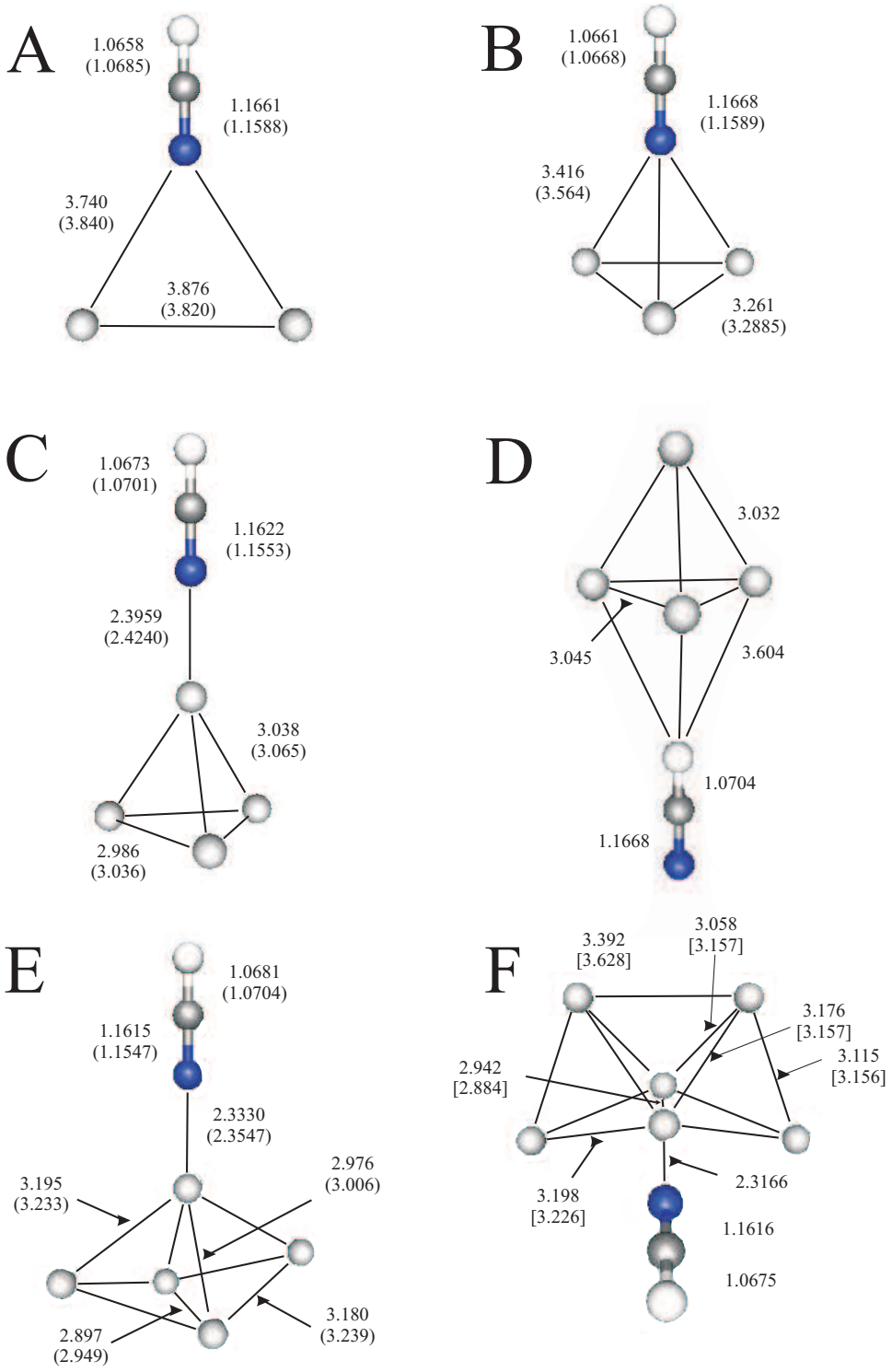

Figure 5.1: Ab initio minimum energy structures for the various HCN-Mg_n complexes, namely; (A) T-shaped HCN-Mg_2, (B) C_3V HCN-Mg_3, (C) the nitrogen bonded, on-top structure for HCN-Mg_4, (D) the hydrogen bonded 3-fold structure for HCN-Mg_4, (E) the nitrogen bonded, on-top structure for HCN-Mg_5 and (F) the global minimum for HCN-Mg_6. The values given in square brackets in (F) correspond to the bond lengths in the free Mg_6 cluster. The BCCD(T) bond lengths are given in parenthesis, where available.

Table 5.1: MP2 and BCCD(T) bond lengths for the bare magnesium clusters, obtained using the 6-311+G(3df) basis set, compared with results from previous studies. The results of the Mg_6 cluster are shown in Figure 5.1F.

	MP2	BCCD(T)	B3PW91	MP2-R12	CCSD(T)	Exp
Mg_2	4.0939	4.0057	3.609	3.891	—	3.891
Mg_3	3.3691	3.3608	3.309	3.387	3.387	
Mg_4	3.0446	3.0988	3.096	3.110	3.110	
Mg_5	2.9574[1]		3.020[1]			
	3.2655[2]		3.337[2]			

Table 5.2: A summary of the calculated MP2 molecular constants, dipole moments and dissociation energies for the HCN-Mg_n complexes, based upon the 6-311++G(3df,3pd) basis set. C-H stretching frequencies are given as red-shifts from the calculated C-H stretch in HCN monomer.

				HCN-Mg_4			
	HCN-Mg	HCN-Mg_2	HCN-Mg_3	On top	3-fold	HCN-Mg_5	HCN-Mg_6
$\Delta\nu/cm^{-1}$	2.63	4.02	6.68	16.30	81.84	20.7	—
A/cm^{-1}	—	0.0928	0.0661	0.078	0.075	0.0376	0.0241
B/cm^{-1}	0.0690	0.0506	0.0452	0.0229	0.0198	0.0241	0.0212
C/cm^{-1}	—	0.0380	—	—	—	0.0178	0.0154
μ /D	3.646	4.066	4.298	8.599	4.297	8.310	7.779
D_e/cm^{-1}	178	445	1157	1721		2641	2907

To supplement the ab initio geometry optimizations, we also calculated various slices through the relevant potential energy surfaces. Electron density difference maps [72] were also calculated for a number of the complexes considered here. These are obtained by taking the difference between the sum of the electron density distributions for the isolated adsorbate and metal cluster and that obtained from the ab initio calculation of the HCN-Mg_n complex. Specifically, BCCD(T) geometry optimizations were performed for HCN, Mg_n and HCN-Mg_n and the corresponding counterpoise corrected BCCD electron density distributions were calculated. The density distributions for the former two systems were summed at the geometry determined for the latter, giving an electron density distribution corresponding to a non-interacting complex. These electron density difference maps provide

[1]Radial-Axial bond length
[2]Radial-Axial bond length

us with a means for visualizing and quantifying the redistribution of electron density resulting from the interaction between the molecule and the magnesium complex.

5.4 Results

5.4.1 Pendular spectra

In our preliminary work on the HCN-Mg_n (n=1-3) complexes [66] we found that the preferred structures had the nitrogen pointing toward the metal complex. As a result, the C-H stretching vibrations are rather weakly affected by complex formation, making the search for the corresponding complexes quite straightforward. Although the ab initio calculations indicate that there are other isomers, we have yet to find spectra associated with these for systems larger than the binary complex [72]. This is despite the fact that we would expect these higher energy isomers to be formed in liquid helium [64, **?**].

All of the complexes considered here have large dipole moments, related to that of the HCN monomer (2.985188 D [159]). As a result, pendular spectroscopy [61, 60] is well suited to their study. Figure 5.2 shows an extended scan recorded with an applied electric field of 24 kV/cm and with the magnesium oven hot enough for the pick-up of multiple atoms. In this case, relatively large droplets (8000 atoms) were made by setting the nozzle temperature at 17.5 K, so that the associated heat capacities are large enough to permit the formation and cooling of the larger magnesium clusters. The peaks in the spectrum are labeled according to the assigned number of magnesium atoms in the corresponding complexes. These assignments are based upon a series of spectra recorded at different magnesium oven temperatures, larger complexes requiring higher magnesium vapor pressures. It is interesting to note that the larger magnesium complexes were not observed when using more typical nozzle conditions (22-23 K), presumably because the smaller droplets have insufficient heat capacity to cool the complexes, and thus are completely evaporated. By recording the HCN pick-up cell pressure dependence of the labeled peaks in the spectrum we were able to establish that they all correspond to complexes containing a single HCN molecule. Indeed, since the pick-up process obeys Poisson statistics [27], the HCN pressure dependence clearly distinguishes complexes containing different numbers of molecules. The signals associated with the weaker bands in the spectrum optimize at higher HCN pressures, indicating that they are associated with complexes containing two or more HCN molecules. As noted above, a detailed study of the binary complex (the highest frequency peak in the spectrum in Figure 5.2) was reported previously 13710. The vibrational origin of the HCN monomer (not

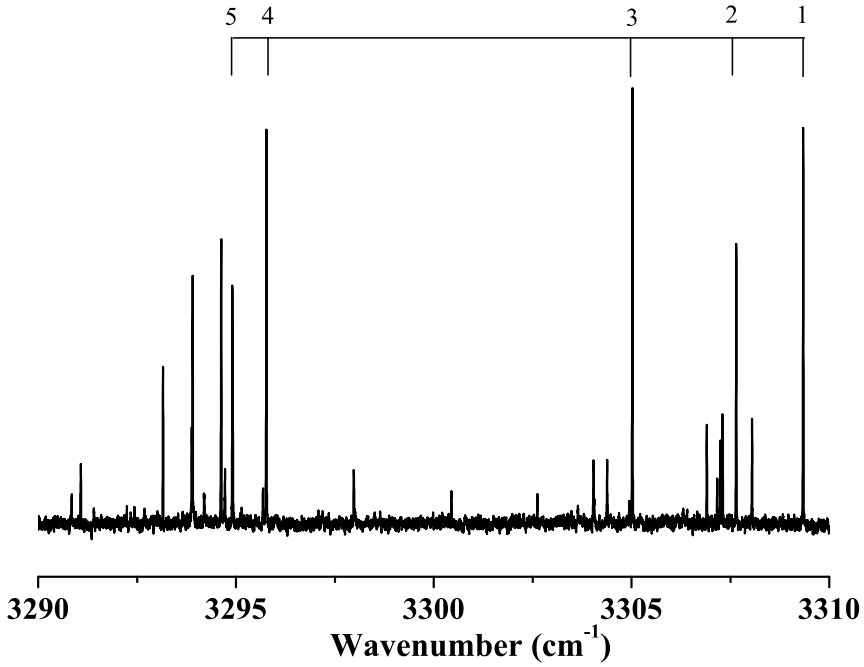

Figure 5.2: A pendular state spectrum showing the C-H stretches of the HCN-Mg_n complexes (n=1-6). The oven temperature and HCN pressure were optimized for the pick-up of multiple magnesium atoms and a single HCN molecule.

shown in the figure) is 3311.11 cm^{-1} (in helium) [64].

Before presenting a detailed discussion of the spectra for the various complexes of interest here, it is worth pointing out the unusual pattern of frequency shifts observed in Figure 5.2. This can be appreciated by noting that the corresponding incremental frequency shifts (from size n to n+1) for hydrogen bonded and van der Waals complexes (for example, HCN chains [64] and Ar_n-HF [56], respectively) decrease smoothly with increasing cluster size. Although this behavior is observed for n=1 and 2, the incremental shift for the n=3 complex is actually somewhat larger than that from n=1 to n=2 and there is a dramatic increase in the incremental shift upon the addition of the fourth magnesium atom. This behavior is inconsistent with a simple two-body description of the interactions between the molecule and the metal atoms and is but one indication that there is a significant change in the bonding going from n=3 to n=4. The incremental shifts for the n=5 and n=6 complexes are then rather small, further illustrating the unusual pattern of vibrational frequencies with size. A detailed understanding of this pattern of frequency shifts will provide us with

Table 5.3: A summary of the experimentally determined vibrational frequency shifts (all to the red) of the C-H stretches (from the HCN monomer). The experimental rotational constants and dipole moments for these complexes are also given (for cases where the excited state rotational constants are not given, they were held equal to the ground state in the fit). In all cases the ground and vibrationally excited state dipole moments were set equal during the fits to the Stark spectra. The dipole moments were empirically corrected for the effects of the helium solvent.

	HCN-Mg	HCN-Mg_2	HCN-Mg_3	HCN-Mg_4	HCN-Mg_5
$\Delta\nu/cm^{-1}$	1.86	3.6	6.2	15.5	16.2
A/cm^{-1}	—	0.03	0.035	0.045	0.015
B''/cm^{-1}	0.02861	0.020	0.01646	0.0113	0.0085
B'/cm^{-1}	0.02851	—	0.01654	0.0112	—
C/cm^{-1}	—	0.017	—	—	0.006
μ /D	3.33	—	4.2	8.5	—

important insights into the nature of the associated adsorbate-metal cluster interactions. Although we do not have a firm assignment of all the peaks to the red of n=6, the magnesium oven temperature dependence of these suggest that they are associated with even larger complexes.

5.4.2 HCN-Mg_2

The bond length and binding energy of the free magnesium dimer have been accurately determined [160] to be 3.891 Å and 0.025 eV per atom, respectively. Given that the Mg-Mg bond strength in the bulk metal is 1.53 eV [161], it is not only clear that the isolated dimer is a van der Waals complex, but also that the character of the bonding must change qualitatively with cluster size. The former is consistent with the fact that the incremental frequency shift from n=1 to n=2 is smaller than that from n=0 to n=1. Indeed, a very similar frequency pattern is observed for molecules bound to rare gas atoms [162]. In fact, the ratio of the frequency shifts (from the monomer) for HCN-Mg_2 and HCN-Mg is 1.8, which is the same as for Ar_2-HCCCN and Ar-HCCCN [163]. (Unfortunately, the analogous data for the Ar_n-HCN complexes (which would provide a more direct comparison) is not available, owing to the fact that they are strongly overlapped by the spectra of $(HCN)_n$ clusters.) For van der Waals systems we expect that the shift due to the dimer will be less than double that for a single atom, simply due to the fact that the molecule is unable to interact with two atoms with the same efficacy as with one, due to steric effects, even though the interactions

may be approximately additive. Although argon and magnesium both interact as van der Waals systems in this size regime, the relative energies of the local minima at the two ends of the HCN molecule are reversed in the two systems. In particular, the global minima correspond to the magnesium binding to the nitrogen end of the HCN, while argon binds to the hydrogen end. This difference can be understood in terms of the polarizabilities of the two atoms, namely 10.6 $Å^3$ and 1.64 $Å^3$ for magnesium and argon, respectively [158]. As a result, the dipole-induced dipole interaction is more important in HCN-Mg, favoring the geometry that brings the polar C-N group closest to the magnesium.

The ab initio calculations for HCN-Mg_2 give the T-shaped geometry shown in Figure 5.1A as the global minimum. The ab initio bond lengths are given in Figure 5.1A, while Table 5.2 summarizes the other important results from the calculations. It is interesting to note that the calculated vibrational frequency shift for the C-H stretch is 4.02 cm^{-1} (to the red), compared to the experimental red shift of 3.6 cm^{-1}. This is compared with the experimental and calculated shifts for HCN-Mg of 1.9 cm^{-1} and 2.63 cm^{-1}, respectively. As discussed in detail elsewhere [72], much of the difference between the experimental and calculated results for the binary complex comes from the fact that the calculations do not include the effects of vibrational averaging, particularly the contribution from intermolecular bending. Even in the case of the HCN-Mg_2 complex the calculated shift is somewhat larger than the experimental value, consistent with the same mechanism. The agreement is presumably better in this case due to the fact that the bending amplitude is smaller, owing to the stronger interaction between the HCN and the Mg_2, compared with that of a single magnesium atom. It is important to state that in making the comparison between the ab initio and experimental results we have assumed that the effects of the helium solvent are small, which is consistent with previous studies on other systems [162, 117, 56]. Of course in making these comparisons we are relying on the cancellation of errors in the vibrational frequency calculations that occurs when differences or shifts are determined. Even with this cancellation, we may already be over interpreting these differences and perhaps should be satisfied with the rather good qualitative agreement between theory and experiment. It is interesting to note that the MP2 Mg-Mg bond length in the T-shaped HCN-Mg_2 complex is 3.917 Å, significantly shorter than that of the isolated dimer, namely 4.095 Å. Similarly the BCCD(T) calculations give 3.8187 Å and 4.0057 Å for HCN-Mg_2 and Mg_2, respectively.

Further experimental evidence for the T-shaped structure can be obtained from the rotationally resolved spectrum obtained in the absence of an electric field. Unfortunately, this was complicated by the fact that the corresponding spectrum is overlapped by that of $(HCN)_2$-Mg. As a result, we had to lower the HCN pick-up cell pressure to minimize the

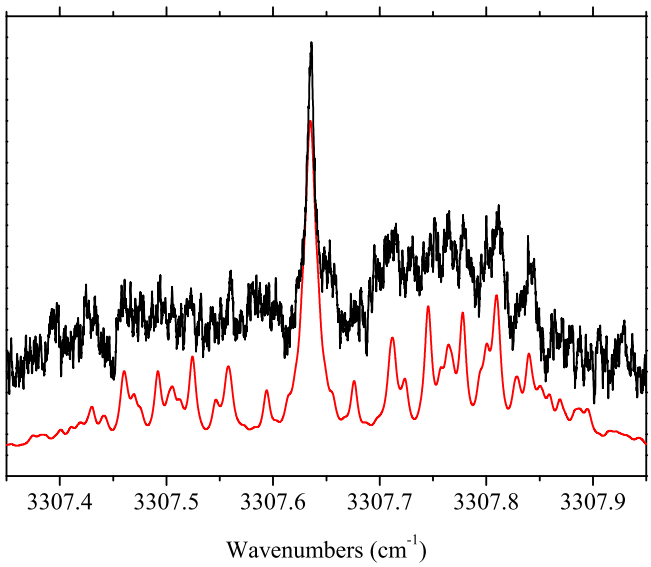

Figure 5.3: A partially resolved electric field free spectrum of HCN-Mg_2. The calculated spectrum is the result of a fit using an asymmetric top Hamiltonian. The low signal to noise ratio is the result of using low HCN pick-up pressures to reduce the contribution from the overlapping $(HCN)_2$-Mg vibrational band.

contribution from the $(HCN)_2$-Mg complex, resulting in a considerable loss in signal for the HCN-Mg_2 complexes as well. The spectrum in Figure 5.3 represents a compromise between signal levels and spectral purity. Although precise rotational constants are difficult to obtain from this spectrum, the simulated spectrum (based upon a T-shaped geometry) clearly supports its assignment to a T-shaped HCN-Mg_2 complex. In fact, the lack of clear and regular structure in the P and R branches of the experimental spectrum is consistent with the complex being an asymmetric top; the asymmetry splitting resulting in poorly separated transitions.

As indicated in Tables 5.1 and 5.2, the ratios of the ab initio rotational constants to those used to fit the experimental spectrum are approximately 2.5, consistent with other systems studied in helium droplets. Unfortunately, the low signal levels prevented us from carrying out Stark measurements of the molecular dipole moment for this system. Nevertheless, the ab inito dipole moment is incrementally larger than that of the binary complex [72], suggesting that simple induction is sufficient to describe this system. This point will be discussed in more detail, along with the dipole moments of the higher order clusters, in the discussion

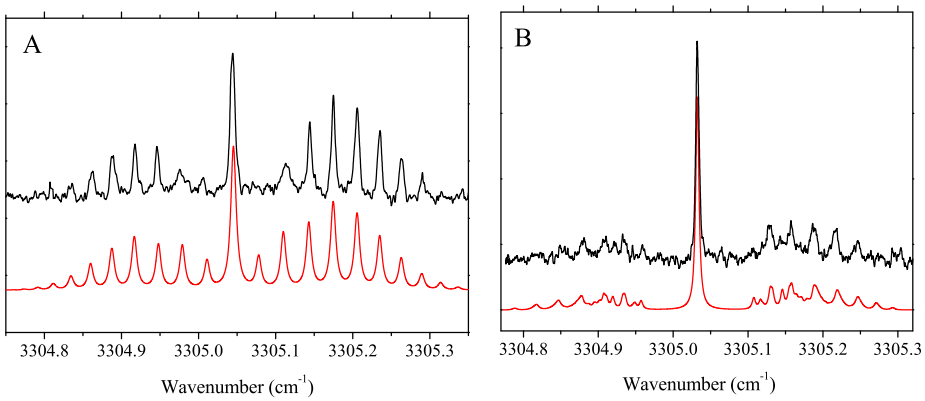

Figure 5.4: (A) A field free, rotationally resolved spectrum and (B) Stark spectrum of HCN-Mg_3. The calculated field free spectrum correspond to a fit to a prolate symmetric top Hamiltonian at a temperature of 0.4 K. The calculated Stark spectrum was generated by diagonalizing the full Stark Hamiltonian for a prolate symmetric top, in the presence of a 1.60 kV/cm electric field.

section of this paper.

5.4.3 HCN-Mg_3

From Figure 5.2 we see that the frequency shift for the C-H stretch of the n=3 complex is also quite small, namely 6.2 cm^{-1} (from the monomer). Such a small frequency shift is only consistent with the nitrogen bonded HCN complex. Assuming that the magnesium continues to behave as a van der Waals system, we would expect (from the rare gas studies12851) that the frequency shift from HCN-Mg_2 to HCN-Mg_3 would be smaller than that from n=1 to 2 [162], which is clearly not the case (see Figure 5.2). Although the effect is quite small for this system, the even larger incremental shift observed for the n=4 complex suggests that we are seeing the onset of non-additive interactions. It is important to note that this effect is also reproduced by the ab initio calculations, which give a frequency shift (from the monomer) for the nitrogen bonded complex of 6.68 cm^{-1}.

The field free spectrum of the n=3 complex, first reported in our preliminary study [66], is reproduced here in Figure 5.4A for completeness, along with a symmetric top fit to the data, the corresponding constants being summarized in Table 5.2. The experimental spectrum

is well reproduced by a parallel band of a prolate symmetric top, indicating that the HCN lies along the C3 axis of the magnesium trimer (see Figure 5.1B). In fact, the nuclear-spin statistics associated with such a C_3v structure were taken into account in the calculated spectrum, based upon the most abundant ^{24}Mg isotope.

Ab initio calculations confirm that the nitrogen bonded C3v structure, shown in Figure 5.1B, is the global minimum on the potential surface, the results for which are summarized in Table 5.2 and Figure 5.1B. As note above, the experimental and calculated frequency shifts for the C-H stretch are in excellent agreement for this structure. In addition, the ratio of the ab initio rotational constant (equivalent to the gas phase value) to the experimental value in helium is 2.8, again typical of molecules in helium [118].

Further evidence for the non-additivity of the interactions in this system comes from noting that the BCCD(T) binding energy of HCN-Mg_3 is De = 835 cm^{-1}, more than 5 times that of the corresponding value for the binary complex, namely 143 cm^{-1}. This issue is further illustrated in Figure 5.5, which compares a pair additive potential (A) with the results of a scan of the HCN-Mg_3 potential (B). The potentials used in this figure were calculated at the MP2/6-311++G(3df,3pd) level, with counterpoise correction [111] being performed at each point, resulting in systematically stronger binding compared to BCCD(T). The pair additive potential was generated by summing all of the pair contributions with the three magnesium atoms held fixed at the geometry determined from the full geometry optimization, namely RMg-Mg=3.3690 Å. The MP2 pair potential used in this calculation was reported previously 13710. The potential scans shown in Figure 5.5 were obtained by also freezing the HCN bond lengths (at the values determined from the complete optimization), while varying the separation between the HCN and Mg_3 and the angle that carries the system from the nitrogen bonded (00^o) to the hydrogen bonded (180^o) structures, through the plane which bifurcates two of the magnesium atoms and contains the third, as indicated by the inset in Figure 5.5.

The two surfaces clearly have qualitative differences, with the global minimum on the pairwise additive surface being much shallower (approximately 550 cm^{-1}) than the supermolecule calculation (approximately 1140 cm^{-1}). The pairwise additive potential also has a second minimum at 180^o (H-end down) that is not present on the ab initio surface. The minimum on the pair potential occurs at a much larger separation between the center-of-mass of the HCN and the center of the Mg_3 (namely 4 Å at the global minimum) than that for the minimum on the supermolecule surface(namely 3.5 Å). All of these results suggest that the HCN-Mg_3 system is the first in the series to display strongly non-additive interactions. Although the ab initio N-Mg bond length is considerably shorter than that expected from

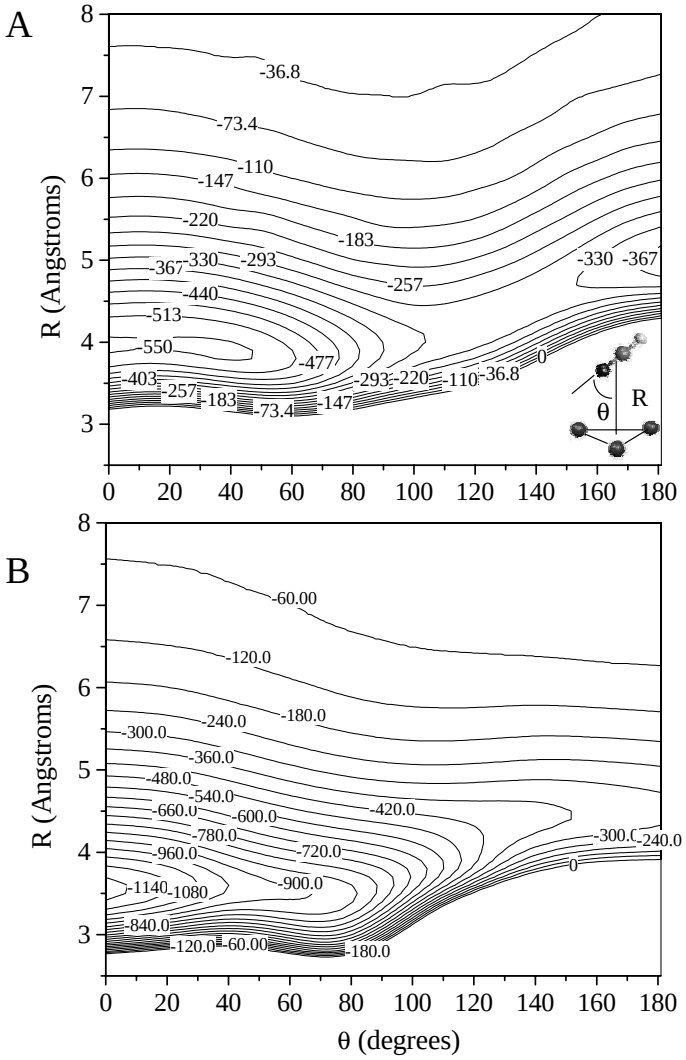

Figure 5.5: Two MP2/6-311++G(3df,3pd) potential energy surfaces for HCN-Mg_3. (A) is the result of summing three HCN-Mg pair potentials at the optimized geometry for the HCN-Mg_3 complex (Figure 5.1B). (B) is the same slice through the ab initio surface for the entire complex. The quoted distances are between the centers-of-mass of the HCN and Mg_3 and the angle is defined in the inset.

the pair potential, the Mg-Mg distances obtained from the ab initio calculations are only slightly smaller than those of the free trimer, namely by 0.08 Å and 0.07 Å at the MP2 and BCCD(T) levels of theory, respectively.

In the limit of very large electric fields, such as used to obtain the spectrum in Figure 5.2, the entire ro-vibrational spectrum of a polar molecule collapses into a single peak. Although this provides considerable improvement in the signal levels, spectra of this type are not useful for determining the dipole moment of the molecules. At more modest electric fields, the Stark spectrum shows considerable structure that can be fit to obtain an experimental dipole moment. Figure 5.4B shows a Stark spectrum of the HCN-Mg_3 complex, recorded with an applied electric field of 1.60 kV/cm. The calculated spectrum was obtained by using the field free rotational constants in a matrix diagonalization of the full Stark Hamiltonian, based upon a symmetric top. The dipole moment was fit by assuming that the ground and vibrationally excited state dipoles are the same. The electric field was calibrated by recording a Stark spectrum of gas phase HCN under identical conditions [72], for which the rotational constants and dipole moments are well known. As discussed elsewhere [120], the effect of the helium solvent on the dipole moment is quite small (a few percent) and can be empirically corrected. The dipole moments reported here are all corrected for the effects of the helium solvent and can be compared directly with the ab initio values. The experimentally determined dipole moment for HCN-Mg_3 is 4.2 D, compared to the ab initio value of 4.297 D. The dipole moments of these complexes provide important information on both the structure and charge distribution in these complexes, as discussed in more detail below. Given the large polarizability of Mg_3 and the large dipole moment of HCN (approximately 3 D), a dipole for the complex of 4.2 D is reasonable, based on simple induction. As we will see in the next section, this is not the case for HCN-Mg_4.

5.4.4 HCN-Mg_4

As noted above and obvious from Figure 5.2, the vibrational frequency shift for the HCN-Mg_4 complex is anomalously large, given our expectations from studies of rare gas complexes. This does not come as a complete surprise, given that the isolated magnesium tetramer already has quite interesting properties, relative to the dimer and trimer. Indeed, numerous theoretical studies have shown that the magnesium tetramer is much more strongly bound (approximately 0.25 eV per atom) than the smaller complexes [164, 165, 133, 166].

The field free spectrum of HCN-Mg_4 is shown in Figure 5.6, along with a fit based on the assumption that the complex is again a symmetric top, with C3v symmetry. In light of the above results for the HCN-Mg_3 complex, our expectation was that the structure of this

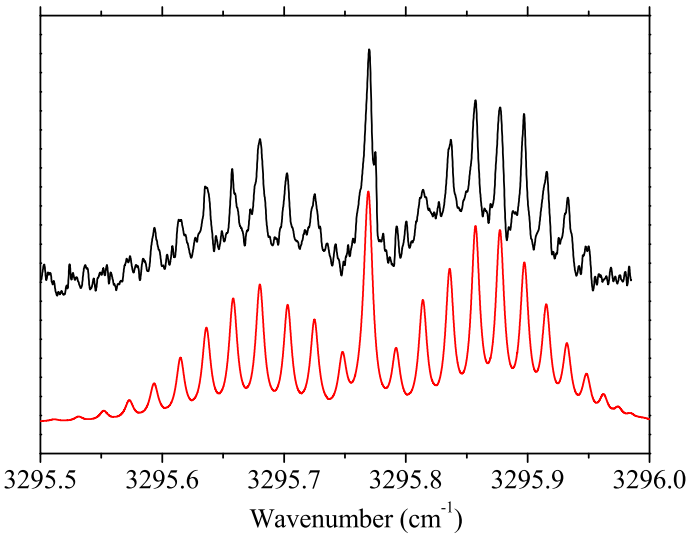

Figure 5.6: A rotationally resolved zero electric field spectrum of HCN-Mg_4. The calculated spectrum corresponds to a fit to a prolate symmetric top Hamiltonian at a temperature of 0.4 K.

complex would have the HCN bound to a three-fold site on the tetrahedral Mg_4. One idea for why the frequency shift is so large in this case is that the hydrogen end of the HCN is pointing into the three fold site. Although we find that there is a local minimum in this geometry, as discussed in detail below, the calculated frequency shift and dipole moment for this isomer are inconsistent with the experimental results. The results of extensive ab initio calculations for this system revealed that the global minimum on the potential energy surface corresponds to a geometry in which the HCN is bound to a single magnesium atom (an on-top binding site), as shown in Figure 5.1C. This complex also has C_3v symmetry and is therefore consistent with the experimental spectrum. It is particularly interesting to note that the analogous geometry to that of the HCN-Mg_3 complex, namely nitrogen down on the three-fold binding site, is not even a local minimum on the HCN-Mg_4 surface.

Figure 5.7 shows a number of cuts through the ab initio potential energy surface for HCN-Mg_4, as a function of the intermolecular separation between the HCN and Mg_4. In Figure 5.7A the HCN is oriented along the axis correlating with the on-top binding site, with either the nitrogen or hydrogen end pointing towards the Mg_4. Figure 5.7B shows the corresponding cuts with the HCN oriented along the axis corresponding to the three-fold binding site. As expected from the geometry optimizations, the global minimum on the

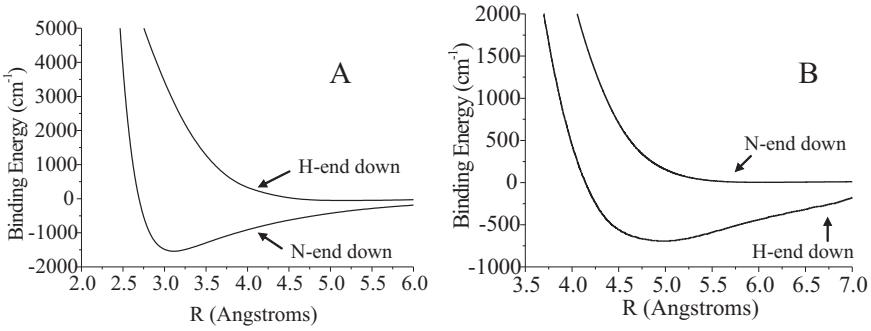

Figure 5.7: Radial cuts through the ab initio potential energy surface for the various C3v geometries of HCN-Mg_4. In (A) the HCN approaches along the on-top axis, while in (B) the HCN is aligned along the axis defining the 3-fold binding site. The quoted distances are between the centers-of-mass of the two sub-units. The calculations were performed at the MP2/6-311++G(3df,3pd) level.

potential surface corresponds to the on-top site, with the nitrogen atom down (Figure 5.1C) (-1600 cm^{-1}). The nitrogen down, three-fold binding site (the global minimum on the HCN-Mg_3 surface) is indeed repulsive for HCN-Mg_4, as is the hydrogen down, on-top geometry. As noted above, the hydrogen down, three-fold binding site is a local minimum on the potential surface (Figure 5.1D) (-700 cm^{-1}). Since the structures in Figures 5.1C and 5.1D both have C_3v symmetry, the observation of a symmetric top spectrum alone can not be used to differentiate between them. A unique structural assignment therefore requires the experimental results that differentiate between these two structures.

The traditional place to turn for a unique assignment is to the rotational constants obtained from the experimental spectrum. Unfortunately, the ab initio rotational constants for these two isomers are rather similar and cannot be used to distinguish between them, particularly given the uncertainties that exist in the corrections for the effects of the helium. Indeed, the ratios of the experimental and calculated rotational constants are approximately the same (namely 3) for both isomers.

As noted above, the vibrational frequency shift for the HCN-Mg_4 complex is rather anomalous (compared to the smaller clusters), so that it might provide information on the structure. Indeed, as shown in Table 5.2, the calculated frequency shift for the hydrogen bonded isomer is much larger (81.8 cm^{-1}) than what is observed experimentally (15.5 cm^{-1}), while the calculated frequency shift for the nitrogen bonded, on-top isomer is 16.3 cm^{-1}, in good agreement with experiment. The large shift for the hydrogen bonded complex makes sense, given that the C-H stretch is directly coupled to the intermolecular bond.

Further progress can be made towards a definitive assignment through the measurement

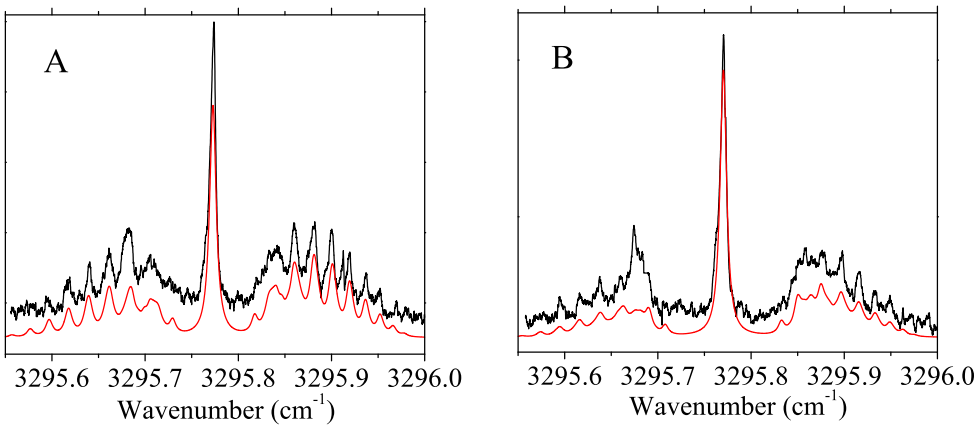

Figure 5.8: Stark spectra of the HCN-Mg_4 complex, corresponding to fields of (A) 0.42 kV/cm and (B) 0.91 kV/cm. The peak at 3295.68 cm^{-1} appears to be a Q branch (which intensifies with increasing field) of an unassigned complex.

of the dipole moment of the complex. In particular, we note from the results in Table 5.2 that the hydrogen bonded Mg_4-HCN complex has an MP2 dipole moment of 4.297 D, while the corresponding value for the nitrogen bonded isomer is 8.593 D. This qualitative difference in the dipole moments can therefore provide us with a more definitive assignment of the spectrum.

Two Stark spectra of the HCN-Mg_4 complexes are shown in Figure 5.8, corresponding to electric fields of 0.42 kV/cm and 0.91 kV/cm. The fitted spectra shown in the figure were obtained using the rotational constants determined from the field free spectrum, with the dipole moment as the only adjustable parameter (assuming the ground and excited vibrational state dipoles are the same), yielding 8.5 0.6 D. This measurement provides definitive evidence that the isomer observed here is indeed the nitrogen bonded structure, shown in Figure 5.1C. Although we have searched extensively for the spectrum of the hydrogen-bonded complex, no such spectrum has yet been observed. This is in contrast with HCCCN-Mg_4[167], where both of the analogous isomers were detected. At the present time we are uncertain if this is still a search problem or if there is some form of anomalous broadening for the hydrogen bonded complex, making it difficult to observe, or if it simply is not populated in the helium environment. Further work is currently underway to help resolve these questions.

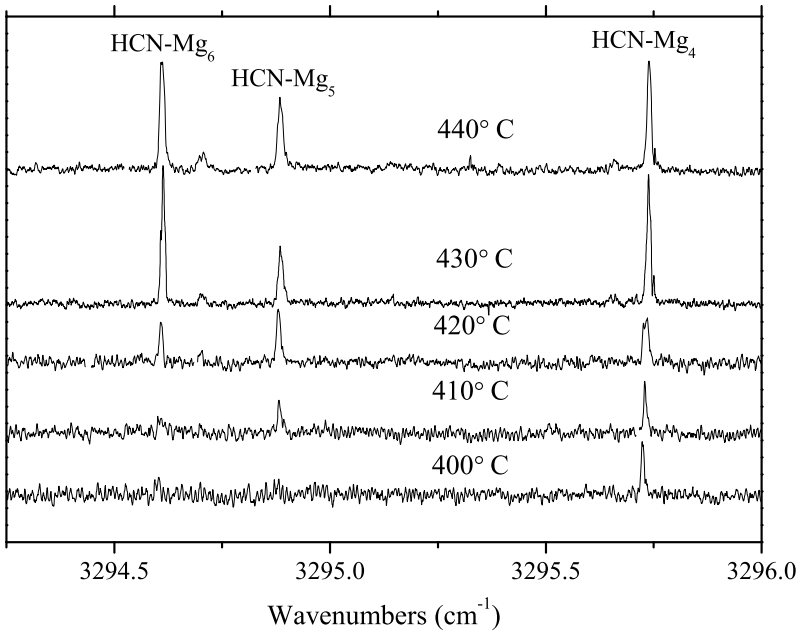

Figure 5.9: Oven temperature dependence of the pendular transitions assigned to HCN-Mg_4, HCN-Mg_5 and HCN-Mg_6. The nozzle temperature and helium backing pressure were kept at 18 K and 50 bar, respectively. HCN pressures were kept relatively low (1.5 x 10-6 Torr) to optimize for the pick-up of a single HCN molecule.

5.4.5 HCN-Mg_5 and HCN-Mg_6

The pendular spectrum in Figure 5.2 shows a number of bands that are shifted further to the red, compared to HCN-Mg_4. To aid in the assignment of these vibrational bands, we carried out a series of pendular scans, at different pick-up pressures, corresponding to different oven temperatures. Figure 5.9 shows five pendular spectra recorded with relatively large droplets (18 K and 50 bar nozzle conditions) and low HCN pressures (1.5 x 10^{-6} Torr), with incrementally increasing oven temperatures. At the lowest temperature (400 C) the only peak observed in the spectrum corresponds to HCN-Mg_4. At higher oven temperatures a second band appears, followed by a third at even higher temperatures. The smooth dependence of the intensities of these bands, as a function of oven temperature, suggests that the two new bands correspond to HCN-Mg_5 and HCN-Mg_6, as labeled in Figure 5.9.

Figure 5.10 shows the zero field spectrum corresponding to the peaks in Figure 5.2, tentatively assigned to HCN-Mg_5 and HCN-Mg_6. Although the signals in this spectrum are quite

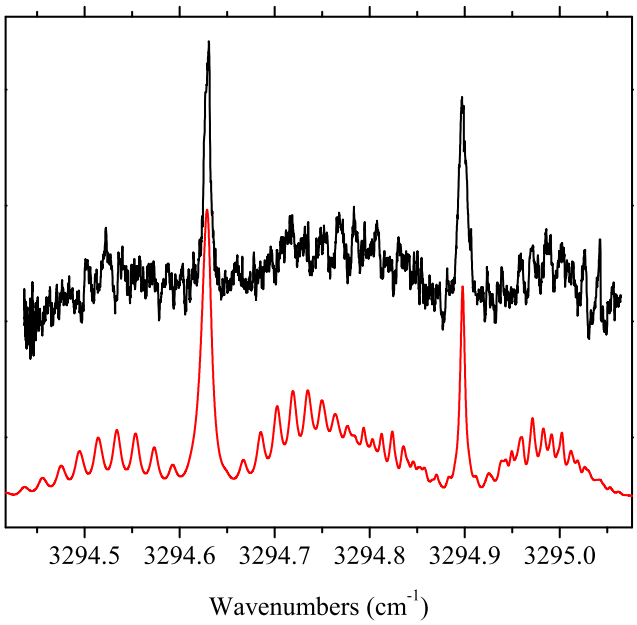

Figure 5.10: A field free spectrum showing the ro-vibrational bands assigned to HCN-Mg_5 (centered at 3294.9 cm^{-1}) and HCN-Mg_6 (centered at 3294.64 cm^{-1}). The simulated spectra are based upon asymmetric top Hamiltonia.

low, the fitted spectra provide reasonable estimates of the associated rotational constants. The best fit to the higher frequency band was obtained using an asymmetric top Hamiltonian, the resulting experimental rotational constants being summarized in Table 5.3. As expected for HCN-Mg_5, the rotational constants are incrementally smaller than those of the n=4 and n=3 complexes. The experimental rotational constants are also approximately three times smaller than those obtained from the ab initio calculation (Table 5.2), corresponding to the structure shown in Figure 5.1E. It is interesting to note that the MP2 frequency shift for the nitrogen-bonded n=5 complex (Figure 5.1E) is 20.7 cm^{-1}, compared to the experimental shift of 16.2 cm^{-1}. The agreement here is not as good as that for the smaller system, a point that is certainly worthy of further study.

Due to the low signal levels associated with the band tentatively assigned to HCN-Mg_6 only an overall fit to the shape of the P, Q, and R branches was possible, yielding 0.01 cm^{-1}, 0.009 cm^{-1}, and 0.008 cm^{-1} for the A, B and C rotational constants, respectively. These rotational constants are quite reasonable, given that they are approximately a factor of three

smaller than the ab initio values given in Table 5.2. Combined with the oven temperature dependence of the band intensities (Figure 5.10), we feel confident in the assignment of HCN-Mg_6, but we realize that more work is needed for an unambiguous assignment.

5.5 Discussion

For all of the complexes discussed above we found that the ab initio rotational constants were approximately a factor of three larger than the experimental values in helium, thus allowing us to make qualitative statements concerning the associated molecular structures. Indeed, this scaling factor is more than sufficient to differentiate between clusters of different size. Nevertheless, there were a number of cases where the differences between the rotational constants of the various isomers of a given system were so small that this qualitative correction was insufficient to differentiate between them. Fortunately, the vibrational frequency shifts and the dipole moments provide additional information that is highly isomer specific. Indeed, the measurement of the dipole moment of HCN-Mg_4 provided the critical information needed to unambiguously determine its structure. The dipole moments are particularly powerful as a structural probe given that they are affected by only a few percent by the helium solvent [120].

In a previous study [72] of the binary HCN-Mg complexes, we found that the associated intermolecular interactions were best described as van der Waals in nature and that the dipole moment was well determined by simple induction associated with the highly polarizable magnesium atom. As noted above, the ab initio calculations for the HCN-Mg_2 complex suggest that this is also the case for this system. We explored this further by calculating the induced dipole moment on the magnesium clusters, assuming that the HCN acts as a point dipole. The magnesium atoms are treated individually, simply summing the induced dipole on each, while keeping the magnesium atoms in the supermolecular equilibrium geometry. As noted previously [158] and evident from the results in Table 4, this simple comparison for the HCN-Mg binary complex is problematic because of the large zero point bending amplitude. Thus, even though the bond length is quite large, suggesting that the point dipole approximation should be quite reasonable, we see in Table 4 that the calculated induced dipole moment (0.662 D) is considerable larger than the experimental value (0.32 D). Nevertheless, the agreement with the ab initio calculation (0.6235 D), which does not include the effects of bending, is quite good. For HCN-Mg_2 we find that the simple point dipole approximate works quite well, yielding an induced dipole of 1.10 D, compared to the ab initio value of 1.0225 D. This is despite the fact that the nitrogen-magnesium bond

lengths are somewhat shorter in this complex, making the dipole approximation somewhat less valid.

The results presented above suggest that the magnesium trimer is the first to show significant non-additivity, resulting in a somewhat anomalous frequency shift. The results in Table 4 show that the simple point dipole approximation, based upon atomic polarizabilities, yields a total induced dipole moment that is too large (1.70 D), compared to both experiment (1.22 D) and ab initio theory (1.2745 D). This trend is consistent with the even shorter intermolecular bond length in this case, suggesting a further breakdown in the point dipole approximation. Although this simple picture does not provide quantitative agreement with experiment for this system, we present it here to provide a backdrop for considering the HCN-Mg_4 complex. Indeed, the results in Table 4 show that the point dipole approximation strongly underestimates the induced dipole moment (3.21 D) for HCN-Mg_4, compared to both experiment (5.6 D) and ab initio theory (5.5705 D), as is also the case for HCN-Mg_5. The sudden deviation from the trend, which for the smaller clusters was to overestimate the induced dipole moment, gives further support that this large dipoles in HCN-Mg_4 and HCN-Mg_5 originates from something other than simple induction.

The origin of the large induced dipoles for the larger systems can be better appreciated by examining the electron difference density maps for the trimer and tetramer. Figure 5.11A shows such a plot for HCN-Mg_3, corresponding to the mirror plane containing the HCN molecule and one magnesium atom. In this plot we have calculated the BCCD electron density for the complex at its optimized BCCD(T) geometry and then subtracted out the BCCD electron density of each subunit (HCN and Mg_3) in the same geometry (BCCD(T) densities were unavailable). The solid/dashed lines represent regions of enhanced/depleted electron density resulting from the interaction between the two sub-units. Integrating the difference densities above and below a dividing surface between the two sub-units shows that there is essentially no charge transfer in this system. The map clearly shows that electron density is "pushed out" of the intermolecular space between the two sub-units, corresponding to simple polarization of the magnesium trimer. This is quite similar to what was observed previously in the binary HCN-Mg complex [158].

It is clear from all of the above data that simple induction cannot be used to explain the dipole moment of HCN-Mg_4. It is interesting to note that the transfer of 0.2 electrons over 4.5 Å (the appropriate center of mass separation of the HCN and Mg_4 sub-units) would result in a dipole moment of 4.32 D, sufficient to explain the large dipole of this system. This can be investigated using the ab initio calculations by calculating the partial charges on the two sub-units. Although several methods exist for estimating these, including Mulliken, Lowdin,

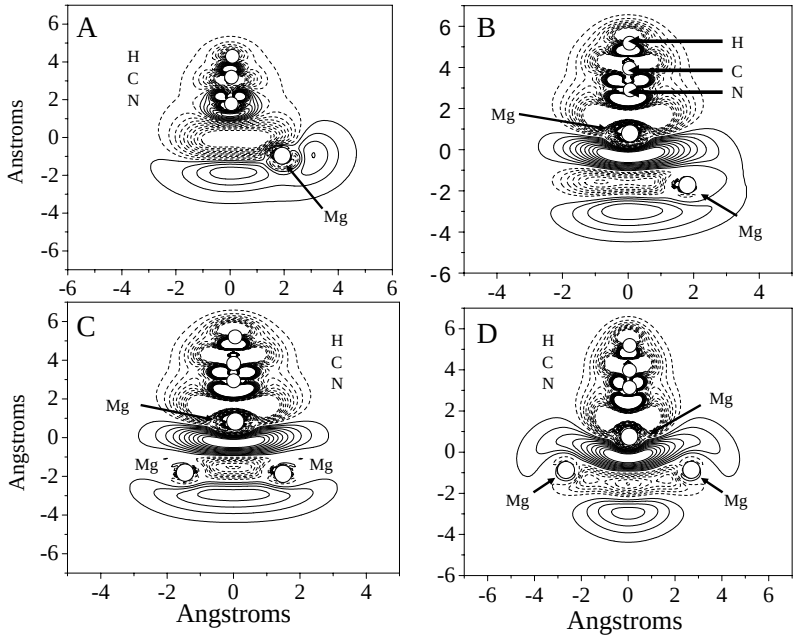

Figure 5.11: Density difference plots for (A) HCN-Mg_3 (a slice containing one magnesium atoms and the HCN that bifurcates other two magnesium atoms), (B) HCN-Mg_4 (a slice containing two magnesium atoms and the HCN sub-unit), (C) HCN-Mg_5 (a slice through the plane containing the three radical magnesium atoms) and D) HCN-Mg_5 (a slice through the plane containing one radical and two axial magnesium atoms). The solid/dashed contours correspond to regions where the electron density increases/decreases due to complex formation. For HCN-Mg_3 the contours span densities from +0.005 e/Å^3 to -0.005 e/Å^3, at 0.0005 e/Å^3 intervals, while for the remaining plots, the contours run from +0.01 e/Å^3 to -0.01 e/Å^3, at 0.001 e/Å^3 intervals.). The simulated spectra are based upon asymmetric top Hamiltonia.

and Morokuma charge analysis, we felt that the method due to Hirschfeld [168] was more appropriate for the present purposes. The calculation of these partial charges begins with the determination of the electron density differences.

Figure 5.11B shows an electron density difference map for the HCN-Mg_4 complex, corresponding to a cut through the mirror plane containing the HCN molecule and two of the Mg atoms. Here again we see significant depletion of the charge density in the region between the two sub-units. Qualitatively, we note that the contours are much more closely spaced in this case, compared to those in Figure 5.11A for HCN-Mg_3, consistent with a much larger perturbation of the electron density due to the intermolecular interactions. The nodal pattern in the difference densities on the Mg_4 is also quite interesting, the most significant charge enhancement occurring between the magnesium atoms. Most surprising is the fact that there is appreciable charge transfer in this system, which is more difficult to see in the difference density plot, but can be quantified using the Hirshfeld analsysis.

In brief, the Hirshfeld method is similarly based upon a "non-interacting" reference density and the partial charges are calculated relative to this, based upon the ab initio calculation for the entire complex. Here we focus on the aspects of the method that are specific to our current task. First we define the reference density as:

$$\rho(\vec{r}) = \rho^0_{HCN}(\vec{r}) + \rho^0_{Mg_4}(\vec{r}) \tag{5.1}$$

where and are the (counterpoise-corrected) densities for the non-interacting fragments. The partial charges are then defined as:

$$q_{Mg_4} = \int \rho_{tot}(\vec{r}) \frac{\rho^0_{Mg_4}}{\rho^0_{REF}} d(\vec{r}) \tag{5.2}$$

$$q_{HCN} = \int \rho_{tot}(\vec{r}) \frac{\rho^0_{HCN}}{\rho^0_{REF}} d(\vec{r}) \tag{5.3}$$

where is the total density of the HCN-Mg_4 complex. These integrals for the HCN-Mg_4 complex yield qMg_4 and qHCN values of -0.15 and +0.15, respectively, implying that 0.15 electrons are transferred from the HCN to Mg_4.

By setting the partial charges at the charge centers of the HCN and Mg_4 fragments, as is standard [168], we can use this analysis to separate the charge-transfer and induction components of the dipole moment for each fragment. In particular, we find that charge transfer contributes 3.30 D, while the additional 2.30 D comes from the polarization of the Mg_4 complex. This is in reasonable agreement with the results from the point dipole

treatment given in Table 4 (3.21 D, based upon atomic polarizabilities) and even better when compared with a point dipole calculation that uses the ab initio polarizability of the isolated Mg_4 complex, giving 2.47 D from induction. The sum of these two terms, along with that of the HCN monomer, yields 8.61 D, as obtained from the ab initio calculations.

The MP2 dipole moments for the two isomers of the HCN-Mg_5 complex were calculated to be 8.310 D and 4.229 D for the on-top and bridging structures, respectively. Figure 5.11C and 5.11D show electron density difference plots, corresponding to slices containing (A) the HCN and the three equatorial magnesium atoms and (B) the HCN with the longitudinal axis of the complex. Here again, the charge density analysis indicates that 0.145 electrons are transferred from the HCN to the Mg_5 cluster.

5.5.1 Molecular orbitals

We now turn our attention to the diversity of structures observed in this study, including the three-fold binding in the trimer and the on-top site for the tetramer. In addition, we find that the HCN preferentially binds to the on-top site associated with one of the radial magnesium atoms in the bipyramid of the pentamer, rather than an axial atom, while the ab initio calculations suggest that the hydrogen bonded isomer of n=5 has a bridging structure. In searching for a simple way of justifying this diverse behavior, we considered the LUMOs and HOMOs of the isolated magnesium clusters, shown in Figure 5.12. Indeed, Mills et al. [169] have used such an approach to discuss the binding of O2 on gold nanoparticles and rough surfaces. Since the nitrogen bonded complexes clearly involve interactions with the nitrogen lone pair, we expect that the LUMO will play an important role here. Indeed, it is clear from Figure 5.12 that the LUMO for the trimer is located on the three-fold binding site, while that of the tetramer peaks on the on-top sites. It is also interesting to note that the LUMOs for Mg_5 and Mg_6 are located primarily on the radial magnesium atoms, consistent with the experimental observation of this isomer.

In contrast, we might expect the HOMOs to play an important role for the hydrogen bonded complex, the electropositive hydrogen seeking out the regions of high electron density. Although somewhat more difficult to visualize from Figure 5.12, due to orbital degeneracies, the locations of the HOMOs in these complexes are consistent with the hydrogen bonded HCN-Mg_4 complex discussed above. The generality of this simple model, as a guide to structure, is clearly something that needs to be further tested.

It is interesting to note that the growth pattern for the magnesium clusters is simple addition to the three-fold sites of the smaller complexes. Three atoms obviously make a triangular structure, four results in a tetrahedron. Since all four faces of the tetramer are

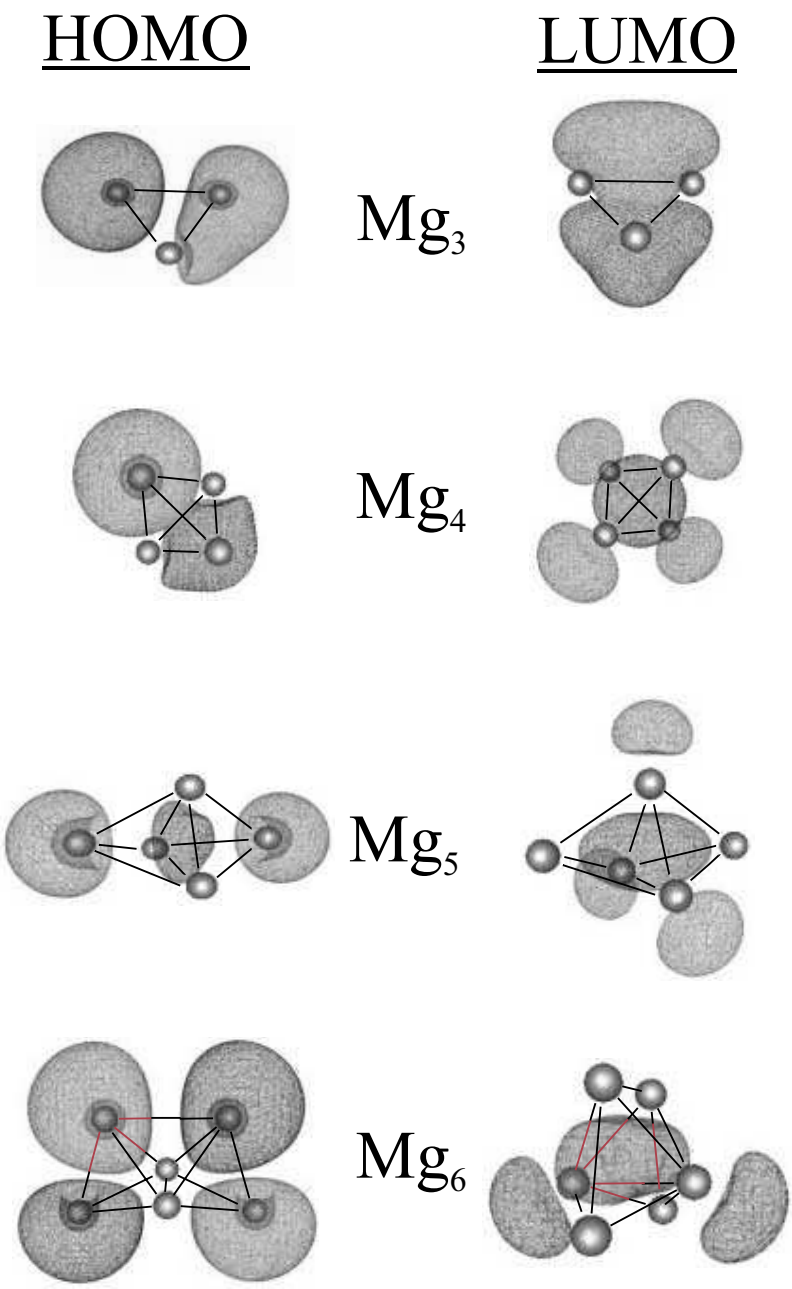

Figure 5.12: Plots of the HOMOs and LUMOs for the bare Mg_3, Mg_4, Mg_5 and Mg_6 complexes, used to rationalize the structures observed for HCN-Mg_n (see text). For Mg_4 the HOMO is a sum of the three degenerate orbitals.

equivalent, the addition of a fifth magnesium atom gives rise to only a single isomer, namely a trigonal bipyramidal structure (see Figure 5.12). Again, all six faces are equivalent, so only one isomer of the hexamer is expected. Thus in all of the systems discussed herein, we did not have to consider multiple isomers of the metal complexes themselves. This situation changes for the n=7, which is something we will have to contend with in studies of the larger clusters.

5.6 Summary

In the present study we reported rotationally resolved infrared spectra for a range of HCN-Mg_n (n=2-6) complexes. The combination of rotational constants, vibrational frequency shifts, dipole moment measurements and extensive ab initio calculations has yielded unambiguous structure assignments for the complexes from n=1-4, with preliminary results for n=5 and 6. The results show a wide range of behavior, varying from van der Waals interactions in the smaller systems to much stronger binding, with significant charge transfer, for the larger complexes. There is good agreement between the experimental and calculated results for all of the systems reported here. The structures obtained from both experiment and theory are consistent with charge donation into the LUMOs of the complexes, for the nitrogen bonded species, and bonding to the HOMOs for the hydrogen bonded complexes. Further experimental work is needed to identify the latter systems. The metal clusters studied here are generally believed to be much too small to display metallic behavior 13816 and one of our goals is to extend these studies to even larger systems. Further theoretical work is also needed to fully quantify the nature of the bonding in these systems. In particular, SAPT calculations would be helpful in sorting out the various contributions to the associated intermolecular interactions.

In the introduction to this paper we presented the idea that a strong base might be a reasonable surrogate for an F-center, as a source of electrons that could activate a metal nanoparticle. We indeed find a sudden onset of charge transfer at n=4, the magnitude of which (0.15 e) is significant, although somewhat smaller than that calculated for gold nanoparticles on metal oxide surfaces (0.5 e) [12]. Given that HCN is not a strong base, there is clear need for studies with different adsorbates, including NH3. Further theoretical work is clearly needed to test these ideas, however, we are also encouraged by the fact that the same HOMO/LUMO picture has also been used to discuss adsorption on gold nanoparticles [169].

Chapter 6

HCN-Zn_n (n = 1-4) complexes

High-resolution infrared laser spectroscopy has been used to obtain rotationally resolved spectra of HCN-Zn_n (n=1-4) complexes formed in helium nanodroplets. In the present study the droplets passed through a metal oven, where the zinc vapor pressure was adjusted until one or more atoms were captured by the droplets. A second pick-up cell was then used to dope the droplets with a single HCN molecule. Rotationally resolved infrared spectra are obtained for all of these complexes, providing valuable information concerning their structures. Stark spectra are reported and used to determine the corresponding permanent electric dipole moments. Ab initio calculations are also reported for these complexes for comparison with the experimental results.

6.1 Introduction

The main driving force for the study of metal clusters has been the detailed characterization of the transition in bonding that takes place as a cluster increases in size. This change in binding is especially relevant in the divalent groups of metals, where the smallest clusters are dominated by van der Waals forces, the intermediate cluster sizes by covalent bonds, and the bulk by metallic bonds. One of the benchmarks for such studies is that of the group 12 Hg_n clusters, for which there is considerable experimental and theoretical [170, 171, 172, 173, 174] literature. The isovalent Cd_n clusters have also been studied [175, 176], although to a somewhat lesser degree, while there is very little theoretical work [177, 178, 179] and virtually no experimental data on the Zn_n clusters [180]. In this series of divalent group 12 atoms, theory predicts that the transitions from van der Waals to covalent to metallic bonding will occur at progressively smaller sizes for the lighter atoms [177]. Thus, zinc atoms seem like prime targets for studying these transitions in a size range that is amenable to study with high-resolution spectroscopy methods.

In this paper we present the experimental structural determinations for clusters containing multiple zinc atoms. The zinc clusters are formed in helium nanodroplets at 0.37 K, after which a single HCN molecule is added to make a metal cluster-adsorbate complex. These experiments were undertaken in a manner similar to that used in a previous study of HCN-Mg_n [181], in which we showed that the magnesium clusters, ranging from 2-6 atoms in size, could be formed and their overall structure left relatively unperturbed by the addition of a single HCN molecule.

The use of helium droplets as an ultracold spectroscopic medium has been thoroughly demonstrated, and it is well known that molecular complexes can freely rotate within the superfluid helium matrix [39, 19], allowing for the measurement of vibrational spectra with full rotational resolution. This free rotation is particularly useful in the study of metal cluster-adsorbate complexes. For example, in our previous HCN-Mg_n study [181], the symmetry of the ro-vibrational spectrum of the C-H stretch gave direct insight into the overall symmetry of the complex. Although this symmetry within the droplet remains unaffected, a small fraction of the helium solvent rotates along with the complex, resulting in a slight increase in the measured moment of inertia. The quantification of this fraction has proven to be very difficult and aside from a few model systems [33, 182, 70, 118], the determination of bond lengths via ro-vibrational spectroscopy remains beyond the current state of the art. Empirically, it has been found that heavy rotors [118] have rotational constants reduced by a factor of 2.5 ± 0.5 in helium when compared to their corresponding gas phase values. This factor of 2.5 will be referred to throughout this paper when comparing ab initio/gas phase rotational constants to those measured in helium droplets.

In addition to structural information, infrared spectroscopy can provide information on the nature of the interaction between the metal cluster and the adsorbate. For instance, the C-H stretching frequency in HCN was found to be very sensitive to the changing magnesium cluster size [181]. Specifically, we observed a dramatic vibrational red-shift for the HCN-$Mg_{n\geq 4}$, when compared to the $n \leq 3$. This shift pointed to a fundamental change in bonding between the HCN and magnesium cluster when going from HCN-Mg_3 to HCN-Mg_4 and was characterized by the measurement of each complex's dipole moment with Stark spectroscopy. The dipole moments of the n 3 complexes were small and only slightly larger than the dipole moment of HCN, indicating a weak dipole induced dipole interaction. On the other hand, the dipole moment of HCN-Mg_4 was found to be 8.5 Debye, which is more than double the dipole moment of HCN. Through the use of charge density calculations it was found that HCN donated 0.15 electrons to the Mg_4 cluster, thus accounting for the very large dipole moment.

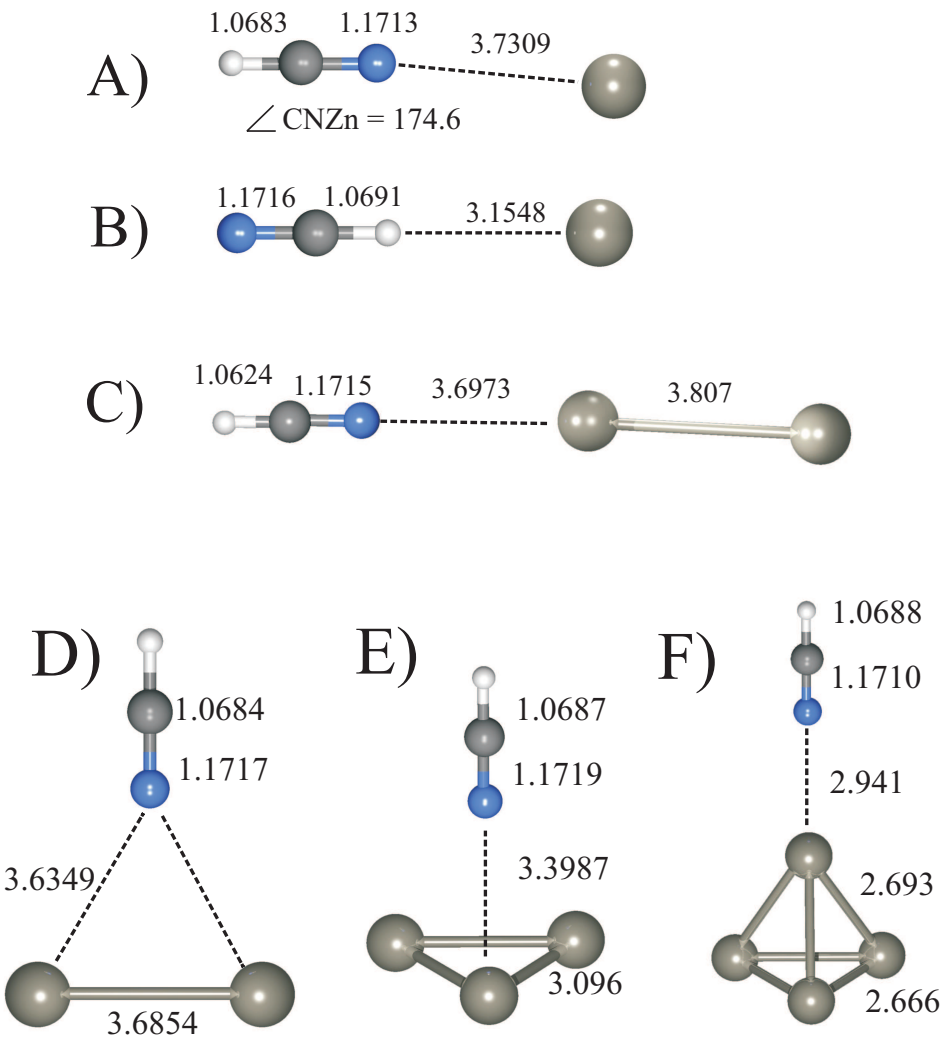

Figure 6.1: Calculated minimum energy structures and relevant bond lengths for the various HCN-Zn_n (n=1-4) complexes, using the ECP10MDF ECP and MP2 level of theory. (A) The HCN-Zn; (B) hydrogen bound linear Zn-HCN; (C) the near-linear HCN-Zn_2; (D) the T-shaped HCN-Zn_2; (E) the C_3V HCN-Zn_3; and (F) the C_3V HCN-Zn_4 complexes are shown. The bond lengths are given in angstroms. The HCN-Zn_2 T-shaped structure contains one imaginary frequency upon vibrational analysis.

In the previous HCN-Mgn study, we performed very high level ab initio calculations on the various metal cluster-adsorbate complexes. This investigation was simplified by the fact that magnesium is quasi-closed shell and has relatively few electrons, which is presumably why such a large volume of theoretical literature exists [183, 134]on which to compare our calculations. The situation with the zinc clusters, however, is quite different because, as noted above, there exists little theoretical data on the small zinc clusters and no data on small zinc cluster's interactions with adsorbates. With very little work on which to compare our calculations the appropriate method had to be chosen with great care. Using the density functional methods of Wang, Wang, and Zhao [179] seemed an unlikely candidate due to the poor performance of DFT when calculating weakly bound structures. Indeed, Zhao comments on the poor agreement between his calculations on Zn_2-Zn_4 when compared to the coupled cluster calculations of Flad [177] and Yu [178] and only includes these results to compare their overall bonding patterns to the higher order clusters. The HCN-Zn_n clusters reported here involved this very same weakly bound cluster size regime in addition to another weak bond between the cluster and the HCN molecule. We attempted the CCSD(T) methods of Flad and Yu but quickly found it to be unfavorable due to the large computational cost of such calculations. In the end we decided to approach the HCN-Zn_n cluster calculations with MP2 methods along with the use of relativistic effective core potentials (ECP), which will be discussed further below.

The large number of electrons associated with zinc atoms make all electron calculations very time consuming. The standard method for reducing the computational cost of systems that contain large numbers of electrons is to replace the core electrons that do not actively participate in bonding with a potential. This potential mimics the behavior of the innermost electrons while drastically cutting the amount of basis functions required for electronic structure calculations. An important advantage that accompanies the use of an effective core potential (ECP) is the ability to include scalar and spin-orbit relativistic effects within the potential itself14590, which becomes increasingly important as the mass of the atom increases. The primary disadvantage is the omission of core polarization, which becomes important when calculating the geometries of van der Waals type complexes [177]. In the case of zinc clusters, this disadvantage can be minimized by using a "small core ECP", which replaces the inner 10 electrons, as opposed to using a "large core ECP", which replaces 28 of the 30 electrons [184]. Alternatively, a core polarization potential (CPP) can be added to the large core ECP. The CPP reproduces the core-valence correlation on the valence electrons and has the tendency to contract the valence electrons [185]. CPPs are available in Molpro [186] but not in the Gaussian [187] ab initio package.

Table 6.1: Bond lengths (angstroms) for the zinc dimer, trimer and tetramer, calculated at the MP2 and CCSD(T) level, using the Stuttgart-Dresden ECP10MDF effective core potential and the (8s7p6d2fg) [6s5p3d2fg] valence basis set. These are compared to previous CCSD(T) calculations using the same small core ECP, in addition to calculations using the large core ECP28MWB potential. The difference between the two small core CCSD(T) calculations are due to our omission of a counterpoise correction in the geometry optimization and the use of a slightly smaller valence basis set.

	MP2	CCSD(T)	Small Core [177] ECP/CCSD(T)	Large Core [190] ECP/CCSD(T)
Zn_2	3.8291	4.1927	3.959	4.150
Zn_3	3.3896	3.9508		3.75
Zn_4	2.7080	2.9358		2.94

6.2 Computational details

Gaussian 2003 [187] was used for all calculations presented in this paper. Geometry optimizations were set with the tight convergence settings. The approach taken here was guided by previous zinc cluster studies [177, 188, 178]and recommendations taken from an earlier study based upon ECPs [189]. In the end, we chose to use the ECP10MDF small core ECP, with an accompanying (8s7p6d)[6s5p3d] valence basis set, which was further augmented with 2f and 1g functions [189]. The HCN was treated using a 6-311++G(d,p) basis set.

In an effort to benchmark the present calculations against those of previous studies, we began by carrying out calculations for neat zinc complexes. Table 6.1 summarizes the results of these calculations, along with those from earlier studies by Flad et al. [177, 190]. Although we omitted the core polarization potential and have used a slightly smaller basis set, the agreement is quite reasonable. Indeed, our MP2 and CCSD(T) calculations show the same trends in bond lengths with cluster size. Notice the large contraction in bond length when going from Zn_3 to Zn_4. This increase in stabilization for Zn_4 is analogous to those seen in the magnesium clusters, and will be addressed later in this paper.

Ab initio calculations for HCN-Zn_n (n = 1-4) were carried out at the MP2 level, the results of which are summarized in Figure 6.1 and Table 6.2. The CCSD(T) calculations were simply too expensive for the adsorbate-metal cluster systems. Fortunately, the comparisons for the naked metal clusters suggest that the structures obtained at the MP2 level are reasonable, although the zinc inter-atomic bond lengths were systematically smaller than those obtained from the CCSD(T) calculations. Harmonic frequencies were also calculated at the MP2 level for these HCN-Zn_n complexes. In all cases, no imaginary frequencies were obtained at the

Table 6.2: Comparison of the calculated and experimental vibrational frequency shifts (all to the red) of the C-H stretches (from the HCN monomer). The calculated and experimental dipole moments are also given. The excited and ground state dipole moments were set to equal during the fit to the Stark spectra. The MP2 calculations used the same valence basis set and ECP that was used for the bare zinc clusters. The two entries for HCN-Zn_2 correspond to the linear (L) and T-shaped (T) structures. (Frequency calculations of the T-shaped structure contain one imaginary vibration.)

	MP2		Experiment	
	$\Delta\ \nu$ (cm^{-1})	μ (Debye)	$\Delta\ \nu$ (cm^{-1})	μ (Debye)
HCN-Zn	2.05	3.51	1.3	3.20 0.05
Zn-HCN	20.4	3.44	30.2	—
HCN-Zn_2	2.46	3.74	2.53	3.7 ± 0.5
HCN-Zn_3	7.17	3.97	4.33	3.85 ± 0.05
HCN-Zn_4	7.80	5.34	7.60	—

optimized geometries. Table 6.2 summarizes the vibration frequency shifts (from the HCN monomer) for the C-H stretching mode, along with the ab initio values for the permanent electric dipole moments. The calculated rotational constants are summarized in Table 6.3.

6.3 Experimental

The apparatus used in the present study has been discussed in detail previously [119, 59, 191]. The droplets are formed by expanding ultra-pure helium through a 5 m diameter nozzle, cooled by a closed-cycle helium refrigerator. The nozzle was operated at a pressure of approximately 60 bar and temperatures between 21.5 and 17 K, corresponding to mean droplet sizes of 1,000 and 8,000 atoms, respectively [48, 45]. Zinc atoms were doped into the droplets by passing the latter through a 1.3 cm long oven, operated at a range of temperatures near 280 C, monitored using a J-type thermocouple, (10^{-5} mbar of zinc) [158]. HCN was added downstream of the metal oven in a separate pick-up cell, the pressure of which was optimized for the capture of a single molecule.

The seeded droplets then pass through a laser interaction region, where the C-H stretch of the HCN is excited by an F-center laser (Burleigh FCL-20), operating on crystal #3 (RbCl:Li). Subsequent vibrational relaxation to the helium droplet results in the evaporation of approximately 600 helium atoms. The resulting depletion of the droplet beam is then detected by a liquid helium cooled bolometer [192]. The laser is amplitude modulated and

Table 6.3: A summary of the experimentally determined rotational constants (cm^{-1}). The MP2 "gas-phase" rotational constants are also given.

	HCN-Zn	Zn-HCN	HCN-Zn_2	HCN-Zn_3	HCN-Zn_4
Experiment					
A /cm^{-1}	—	—	0.021	0.0108	0.005
B /cm^{-1}	0.0236	0.004	0.0155	0.0107	0.00490
C /cm^{-1}	—	—	0.0089	—	—
D /cm^{-1}	1.3x10-5	—	—	5.3x10-6	3x10-7
MP2					
A /cm^{-1}	—	—	—	0.02776	0.03710
B /cm^{-1}	0.04545	0.03766	0.01265	0.02776	0.01487
C /cm^{-1}	—	—	—	0.02751	0.01487

the corresponding bolometer signals are measured using phase sensitive detection methods. The details associated with tuning and calibrating the laser can be found elsewhere [193].

An electric field can also be applied to the laser interaction region, using two metal electrodes. A considerable enhancement of the signal levels is obtained by using a large electric field (24 kV/cm) to collapse the entire ro-vibrational band into a single "pendular" peak 43384339. The added sensitivity is particularly useful when searching for new species. At more modest electric fields (1-4 kV/cm), Stark spectra are recorded to obtain experimental dipole moments 10965 for the HCN-Zn_n complexes.

6.4 Results

The experimental conditions required for the formation of the various HCN-zinc complexes were optimized by first adjusting the HCN pressure to achieve the best possible monomer signals. The zinc oven temperature was then slowly increased, while monitoring the HCN monomer signal 888610818. The pick-up of zinc atoms from the vapor resulted in a corresponding decrease in the HCN monomer signal, which was typically reduced by a factor of two before scanning was commenced. The initial search for the spectra corresponding to the C-H stretches of the HCN-Zn_n clusters was performed with a large DC electric field applied to the laser interaction region.

Figure 6.2 shows a series of pendular spectra, recorded over a range of zinc oven temperatures and helium droplet sizes. In particular, large droplets are required to form the

larger zinc complexes, owing to the considerable condensation energy that is dissipated to the droplets. In the spectra shown in Figure 2 the HCN pickup cell pressure was deliberately kept below that required to optimize the HCN monomer signal to ensure that contributions from the HCN dimer, trimer, etc. were minimized, although these bands are still weakly visible. From the oven temperature dependence of the various peaks in these spectra (see Figure 6.2), we tentatively assign the peaks labeled n = 1 - 4 to the corresponding HCN-Zn_n complexes. In particular, the larger complexes are not seen at the lowest oven temperature (350 C), given that they require higher zinc vapor pressures and larger mean droplets size. The oven temperature and droplet size dependence of these bands is consistent with our previous observations of the corresponding magnesium clusters 14432. Indeed, the pattern of vibrational frequency shifts (from the HCN monomer) is also reminiscent of that observed for the HCN-Mgn complexes 14432. Of particular note is the relatively large frequency shift in going from HCN-Zn_3 to HCN-Zn_4, which was also observed for the corresponding magnesium complexes. This behavior is quite different from that observed in van der Waals complexes 12851 and is indicative of strongly non-additive interactions. The tentative assignments given here can now be further tested by examining the individual bands in the absence of the strong DC electric field.

6.4.1 HCN-Zn binary complex

Figure 6.3 shows a zero field spectrum obtained in the region centered on the band labeled as 1 in the pendular spectrum shown in Figure 6.1. This spectrum is consistent with that of a linear molecule, showing well resolved R and P branch transitions. A linear rotor fit to the experimental spectrum is shown in the Figure 6.3, from which the rotational constants and vibrational origin given in Table 6.3 are determined. As expected, the experimental rotational constant for the ground vibrational state (0.0236 cm^{-1}) is much smaller than the ab initio value for the binary complex (0.04545 cm^{-1}), corresponding to a ratio of 1.9, well within the range of values observed for a wide range of molecules in helium [52]. The small frequency shift of this band from the monomer suggests that the complex is nitrogen bound, in agreement with the ab initio structure shown as an inset in Figure 6.3.

As is typical of helium solvated molecules, the low J transitions are rather broad compared to those associated with higher J states. This is consistent with the fact that low J states are more sensitive to the anisotropic interactions that might result from the surrounding solvent [71].

Figure 6.4 shows an experimental Stark spectrum of the HCN-Zn binary complex, recorded at an electric field of 2.02 KV/cm. A fit obtained by diagonalizing the full Stark Hamiltonian

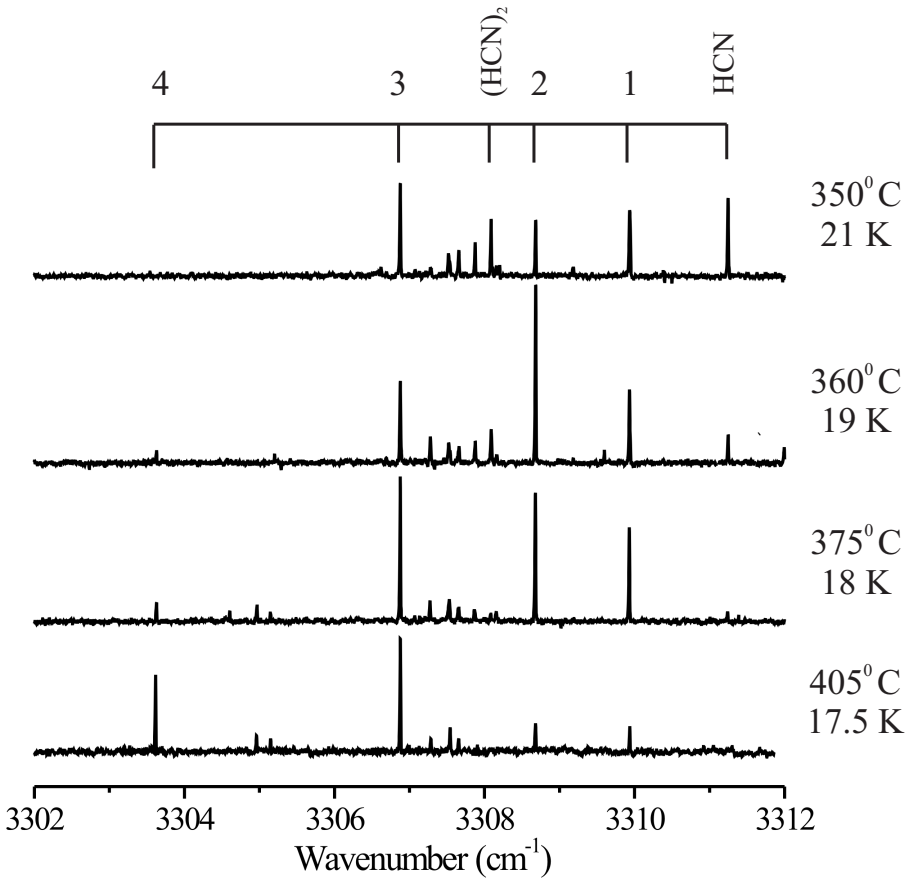

Figure 6.2: A series of pendular state spectra taken at various zinc oven temperatures and droplet sizes. HCN-Zn_n are labeled as well as the HCN and HCN dimer pendular peaks. The small, unlabeled peaks are due to higher order HCN clusters. The higher oven temperatures and larger droplets were required to form the larger clusters. The HCN pick-up cell pressure was kept below the optimal pressure for the pick-up of a single HCN molecule per droplet in order to decrease peak intensities arising from HCN dimmers and trimers.

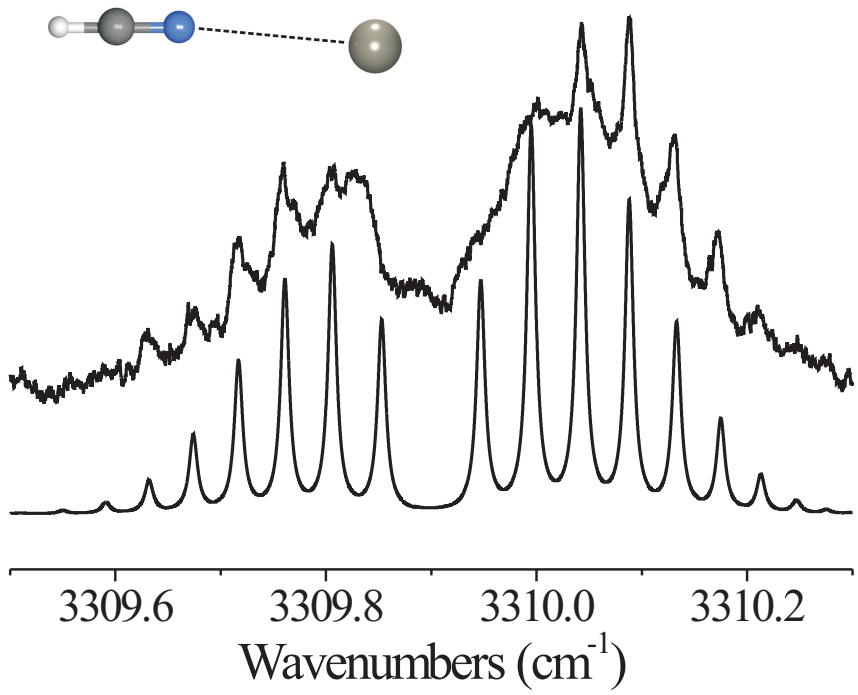

Figure 6.3: The full rotationally resolved spectrum of HCN-Zn. The simulated spectrum, plotted below the experimental spectrum, was generated with a linear rotor Hamiltonian (equilibrium structure is given in the inset).

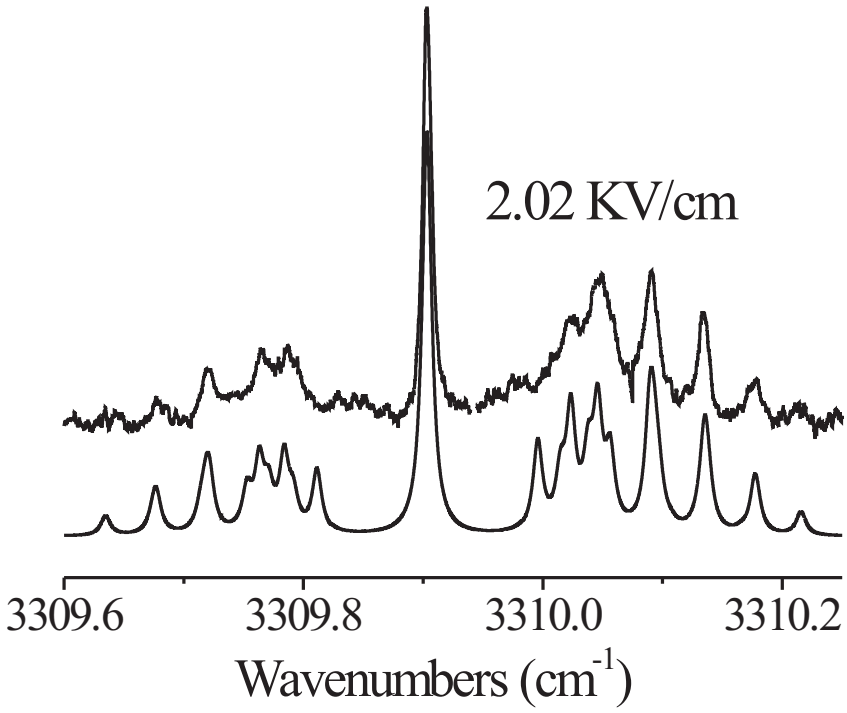

Figure 6.4: The fitted constants, along with the dipole moment, were used to fit the Stark spectrum. Diagonalizing the full Stark Hamiltonian generated the simulated Stark spectrum at 2.02 KV/cm (below experimental spectrum).

matrix [194] is shown below the experimental spectrum in Figure 6.4, based upon the rotational constants and band origin obtained from the zero field spectrum. The only adjustable parameter in this fit is the permanent electric dipole moment, which was assumed here to be the same in the ground and vibrationally excited states. As discussed in detail elsewhere [120], the dipole moments determined by fitting a helium nanodroplet Stark spectrum require only minor corrections (1-2%) to account for the polarization of the solvent atoms. The dipole moment obtained from this analysis is 3.20 Debye, which is in reasonable agreement with the results from the ab initio calculations, namely 3.51 Debye. It should be pointed out that the latter value corresponds to the equilibrium structure of the HCN-Zn complex, while the experimental value includes the effects of vibrational averaging. As discussed previously for the HCN-Mg complex [72], intermolecular bending of the complex results in an experimental dipole moment that is smaller than that for the equilibrium structure, which is in agreement with the difference observed here. These effects have also been discussed for a number of weakly bound van der Waals complexes [122, 125, 123]. The ab initio calculations give a binding energy for the HCN-zinc complex of only 116 cm^{-1} (uncorrected for zero-point energy), again suggesting that this system will undergo wide amplitude bending motion.

In the previous study of the HCN-Mg complex [181, 72] we showed that the increase in the dipole moment upon complex formation (the dipole moment of HCN is 2.979 D [195]) can be explained in terms of the polarizability of the metal atom. Not surprisingly, HCN-Zn behaves similarly. The ab initio dipole moment of HCN-Zn is somewhat smaller (3.51 Debye) than that of HCN-Mg (3.71 Debye), consistent with atomic polarizabilities of Zn and Mg, namely 7.1 $Å^3$ and 10.6 $Å^3$, respectively [158]. In contrast, the experimental dipole moments for these two complexes are the same, within the experimental uncertainty, suggesting that the HCN-Zn complex is somewhat stiffer than HCN-Mg. This seems inconsistent with the fact that the ab initio HCN-Mg binding energy between the HCN and Mg atom is about 140 cm^{-1}, while that of HCN-Zn is about 120 cm^{-1}. However, considering the size of both metal atoms, one observes that the van der Waals radii for Zn and Mg are 1.39 Å [196] and 1.73 Å [196], respectively. This smaller size of zinc allows it to interact more closely with the lone-pair on the nitrogen of HCN, thus reducing amplitude of the bending motions and reducing the effects of vibrational averaging. It should also be pointed out that we neglected the core polarization in the calculations and therefore probably underestimated both the binding energy and induced dipole moment of the HCN-Zn complex. A high-level all-electron two-dimensional potential energy surface would be extremely helpful in the analysis of the vibrational averaging taking place in this complex but, at the moment, is beyond the scope of this study.

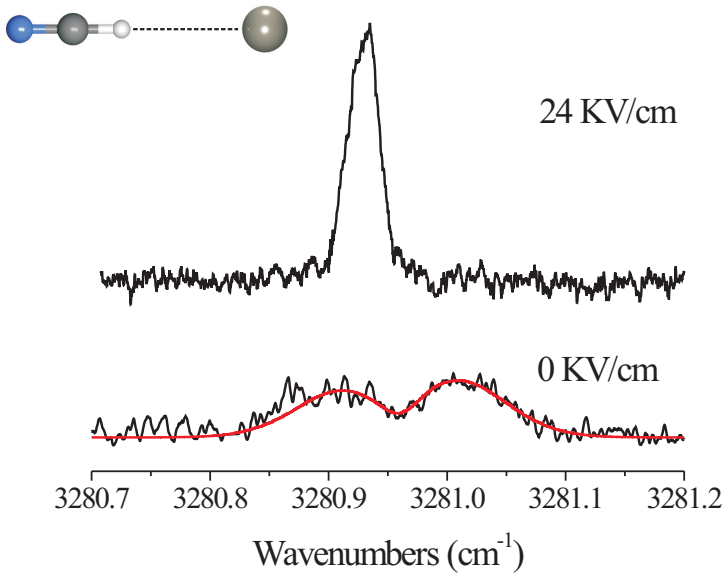

Figure 6.5: Pendular spectrum of the hydrogen bound Zn-HCN complex (upper plot). The poorly resolved zero-field Zn-HCN spectrum (lower plot) is shown along with the crude fit. The calculated structure is shown in the inset.

Although the calculation of the full 2D intermolecular potential energy surface for the HCN-Zn complex has not been carried out, we concluded from a large number of geometry optimizations that the nitrogen bound complex discussed above corresponds to the global minimum on the ab initio surface. In addition to this complex, calculations revealed that a hydrogen-bound linear isomer exists in a local minimum on the surface. The corresponding geometry, vibrational frequency shift, and rotational constant are given in Figure 6.1 and Tables 6.2 and 6.3. Previous studies [197, 65] have shown that the growth of complexes in helium nanodroplets (in the absence of strong dipole-dipole interactions) can result in the formation of these higher energy isomers. Owing to the hydrogen bonded nature of this isomer, we expect that the corresponding spectrum will be more strongly shifted from the HCN monomer.

Figure 6.5 shows a pendular spectrum, along with the corresponding field free spectrum, shifted from the HCN monomer by 30.2 cm^{-1}. This is to be compared with the ab initio frequency shift for the hydrogen-bonded Zn-HCN complex of 20.4 cm^{-1}. Although the agreement is not quantitative, in both cases the shifts are qualitatively larger than the corresponding values for the nitrogen bound complex. Given that these calculations do not

include the effects of anharmonicity, we are satisfied with the agreement between theory and experiment. In part, owing to that fact that the line widths associated with the observed spectra are much broader than those of the nitrogen bonded complex, the signal levels in the zero field spectrum are quite low. Fortunately the pendular spectrum could be used to optimize the signal levels. In particular, we found that the pendular spectrum optimized at the same zinc oven temperature and HCN pressure as used for the nitrogen-bound binary complex, giving further support to the assignment of this band to the hydrogen bonded binary complex.

The low resolution of the zero field spectrum would appear to prevent the determination of a rotational constant for this complex. However, since the rotational temperature can be assumed to be in equilibrium with the droplet temperature (0.37 K), the separation between the P and R branches can be used to estimate the rotational constant of this complex. The fitted spectrum shown in Figure 4 was generated using the line width determined from the pendular spectrum, using a linear rotor Hamiltonian. The resulting B rotational constant is given in Table 6.3. Although the uncertainty in this value is considerably larger than that for the nitrogen bound complex (due to the lack of fine structure), it is still apparent that reduction in the rotational constant due to the helium is much greater than the usual factor of three (closer to 9) that has been observed for many other systems [121]. It is interesting to note that we observed the same anomaly for the hydrogen bound Mg-HCN complex [72]. Indeed, it is clear from a large number of studies that the ratio of the gas phase and helium nanodroplet rotational constants depends on the details of the intermolecular potential between the solute molecule and the helium, which have not been calculated for the HCN-Zn binary system.

6.4.2 HCN-Zn_2

We now turn our attention to the peak labeled 2 in Figure 6.2, which we have tentatively assigned to the HCN-Zn_2 complex. Here we note that the ECP/MP2 calculations gave the linear complex in Figure 6.1 as the only stable complex. We expected and did find a T-shaped geometry using ECP/MP2 methods, but upon harmonic vibration calculations, the structure returned a single imaginary frequency indicating that the T-shaped structure was a transition state. This conclusion is clearly in poor agreement with the experimental data, displayed in Figure 6.6, which shows the spectrum of an asymmetric top (notice the Q branch). As a double check, a series of all-electron calculations (6-31+G(d) basis set for zinc and 6-311++G(d,p) for HCN) were performed, revealing both a linear and T-shaped isomer (with all real frequencies), the latter being the most stable. As stated above, Figure 6.6

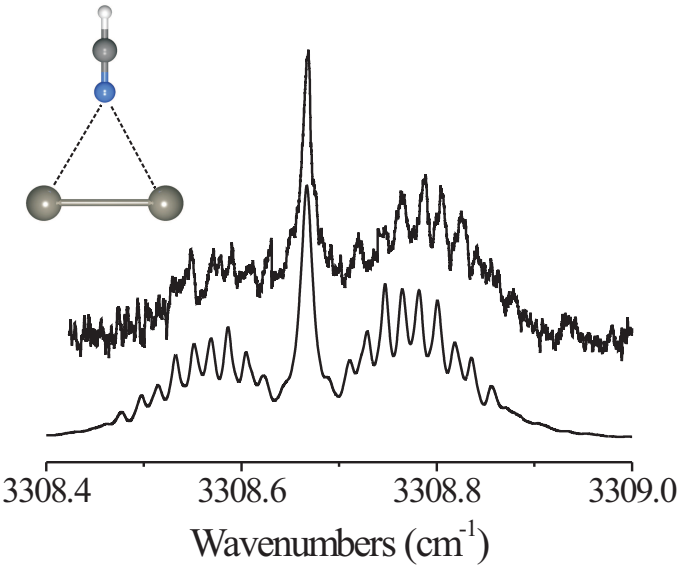

Figure 6.6: Partially resolved ro-vibrational spectrum of HCN-Zn_2. Although theory predicted a linear structure, the experimental spectrum that of an asymmetric top.

immediately suggests that that the complex observed in the experiment is T-shaped, given the presence of the strong Q branch. In fact, the fit shown just below the experimental spectrum in Figure 6 was obtained by first using the rotational constants given by the calculations for the T-shaped structure (divided by 2.5) and then by fine tuning the rotational constants to get the best agreement with experiment. The resulting rotational constants and vibrational band origin are given in Table 3. Although considerable effort was expended in searching for a linear isomer of the HCN-Zn_2 complex, no such features were observed in the spectrum. At this point we are uncertain as to whether this means the all-electron calculations are in error (perhaps due to the minimal basis sets) or if the barrier between the two isomers is simply too small to support the linear complex.

The Stark spectrum of the HCN-Zn_2 complex is given in Figure 6.7. A direct comparison of the experimental (3.7 Debye) and theoretical dipole moment was problematic for reasons stated above. Does one compare the experiment with ECP/MP2 calculations that give an imaginary frequency or does one compare it with all-electron calculations that utilize inferior basis sets? We chose to use the T-shaped geometry calculated via ECP/MP2 methods that contained a single imaginary frequency (11 cm^{-1}). This was done primarily because the HCN-Zn_2 complex is bound by weak van der Waals forces and large polarizable basis sets are

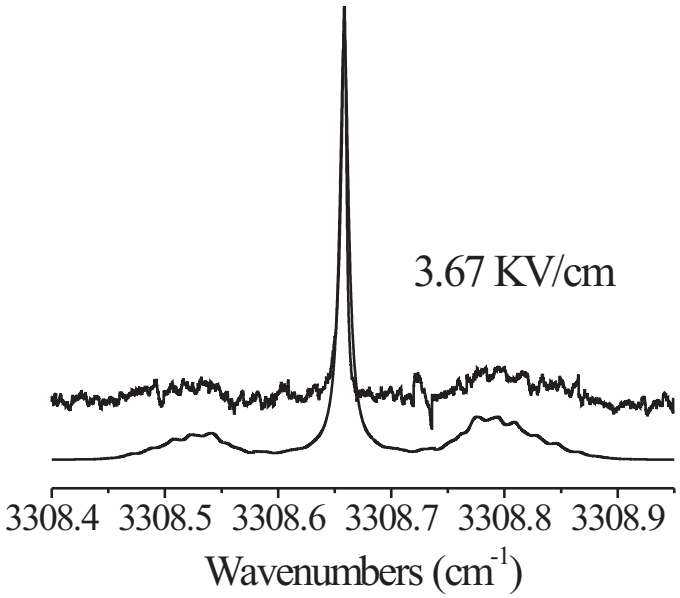

Figure 6.7: The Stark spectrum of HCN-Zn_2 recorded at 3.67 KV/cm using the T-shaped rotational constants determined from the field free spectrum.

required to reproduce the dipole induced dipole interactions that dominate the intermolecular forces. Table 6.2 gives the dipole moments of both the T-shaped and linear isomers of the calculated HCN-Zn_2 structures, which are very close to each other. Due to the uncertainty involved in fitting the asymmetric top Stark spectrum and the uncertainty in the calculated dipole moments, we are forced to concede that the measurement of the dipole moment of HCN-Zn_2 gives no help determining the correct calculated structure, and we must rely solely on the measured field free asymmetric top spectrum.

6.4.3 HCN-Zn_3

A zero field spectrum for the HCN-Zn_3 complex is shown in Figure 6.8. This well resolved spectrum appears to be that of a symmetric top complex, consistent with the ab initio structure shown in Figure 6.1. From the relatively small red-shift (relative to that expected for hydrogen-bound structures, namely ¿ 25 cm^{-1}), we conclude that the HCN-Zn_3 complex has C_3V symmetry, with the nitrogen of HCN pointing towards the center of the zinc trimer. The calculated spectrum (lower spectrum) in Figure 6.8 was generated using the rotational constants and vibrational band origin given in Table 6.3. Determining the A rotational

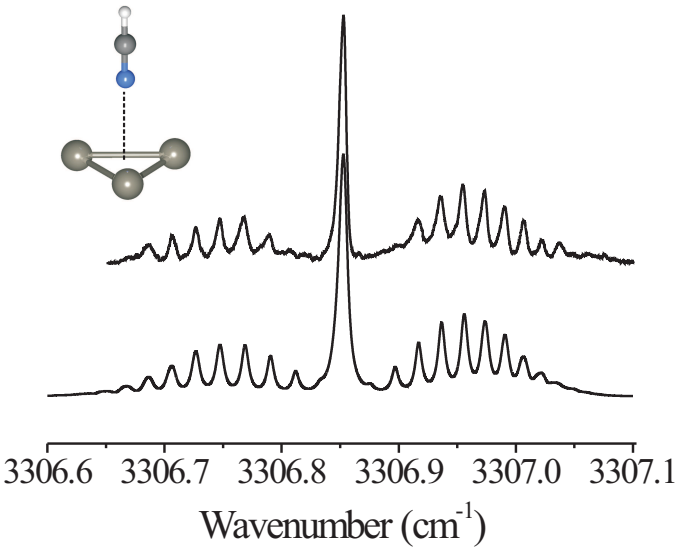

Figure 6.8: The fully resolved ro-vibrational spectrum of HCN-Zn_3. The symmetric top spectrum can only be due to the C_3V structure shown in the inset. The simulated spectrum was initially generated with a linear rotor Hamiltonian to fit the P- and R- structure. The A constant was obtained by fitting the relative intensities.

constant from a parallel band is always problematic, given that K is conserved in all of the observed transitions. As a result, we were able to use the relative intensities of the P, Q and R branches (knowing the rotational temperature) to estimate A. Nevertheless, this estimate was also complicated by the fact that the broadening in the spectrum is dependent upon the rotational states in question, the lower J state transitions again being broader than those associated with higher J. As a result, the uncertainty in the A rotational constant is considerably larger than that for B. The corresponding ab initio data are given in Tables 6.2 and 6.3 and are in good agreement with experimental data. Indeed, the ratio of the ab initio (gas phase) (0.0278 cm^{-1}) to helium droplet (0.0107 cm^{-1}) B rotational constant is 2.6.

Figure 6.9 shows one of several Stark spectra recorded for the HCN-Zn_3 complex. The dipole moment obtained from fitting a number of such spectra (and used to generate the calculated spectrum shown in Figure 6.9) is 3.8 0.1 D. Once again, this is slightly smaller than the ab initio value (3.97 D), consistent with the smaller complexes. Once again, all of the dipole moments quoted here have been corrected for the small effect of the helium solvent polarization 13762. It is interesting to note the trend of increasing dipole moment

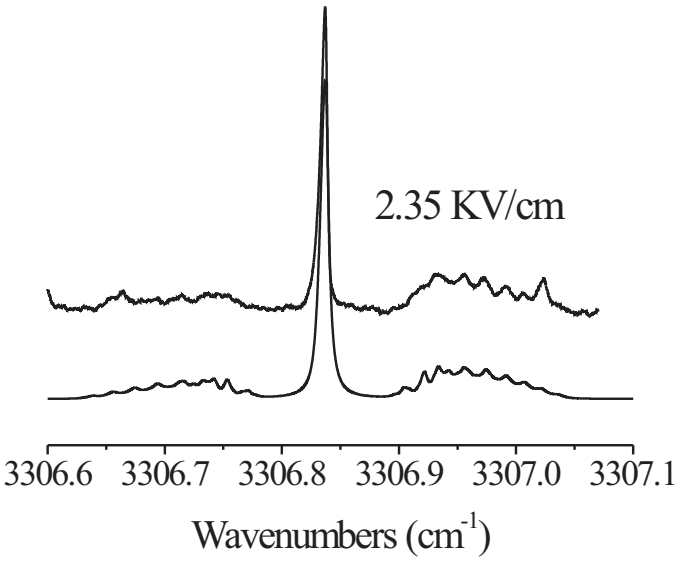

Figure 6.9: Stark and simulated (below) spectrum of HCN-Zn_3 recorded at 2.35 KV/cm.

with increasing cluster size in both the experimental and ab initio results. This incremental increase is consistent with simple induction, given that the polarizability of the zinc cluster increases with size.

6.4.4 HCN-Zn_4

Based upon our previous HCN-Mg_n work [181], where the largest clusters were optimized with the highest oven temperatures and largest droplets sizes, the spectrum shown in Figure 6.10 was assigned to HCN-Zn_4. This trend is clearly shown in Figure 6.2, where the pendular spectrum is weighted towards the largest clusters at an oven temperature of 405°C and nozzle temperature of 17.5 K. Turning our attention to the symmetry of the field free spectrum shown in Figure 6.10, it is clear that this is due to the parallel band of a symmetric top. Assuming that this complex is due to a single HCN molecule bound to a Zn_4 cluster, only four possible geometries can exist that give rise to the symmetric top spectrum shown in the figure. The first two possible geometries are the HCN molecule bound to the three-fold site of the Zn_4 tetrahedron, either H-end down or N-end down; the second two possible geometries are with the HCN bound to the on-top site of the tetrahedron, again, either N- or H-end down. Due to the relatively small frequency shift from HCN monomer

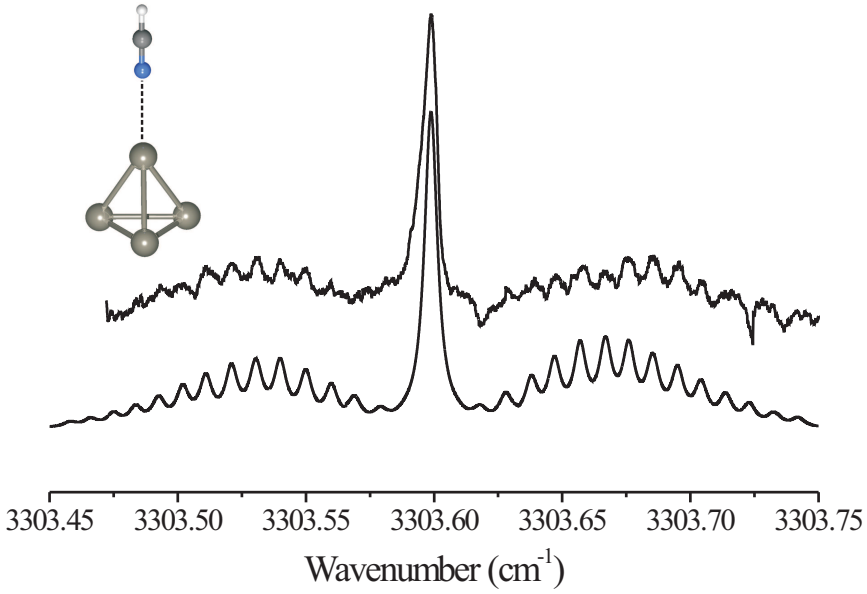

Figure 6.10: The ro-vibrational spectrum of the HCN-Zn4 complex. Poor signal-to-noise prevented the precise measurement of dipole moment through Stark spectroscopy. The symmetric top simulated spectrum is given below the experimental and is consisted with the proposed structure shown.

and on the basis of our previous experience with weakly bound complexes, we can rule out the two hydrogen bound species giving rise to the spectrum in Figure 6.10. For example, in the HCN-Zn results discussed above, a single zinc atom bound to the hydrogen side of HCN shifted the C-H stretch by 30.2 cm^{-1}. We are now left to consider the remaining two nitrogen bound complexes.

The results of the our ab intio calculations for the HCN-Zn_4 complex are summarized in Tables 6.2 and 6.3, in addition to the structure shown in Figure 6.1. The structure that corresponds to the nitrogen-end of the HCN molecule bound to the on-top site of the Zn_4 tetrahedron is the only possible structure to explain the spectrum shown in Figure 6.10. In fact, a test calculation of the HCN bound (N-end down) to the three-fold site of the Zn_4 cluster was found to be totally repulsive, just as it was found in the case of HCN-Mg_4. Furthermore, there is excellent agreement between the experimental vibrational shift (7.6 cm^{-1}) and the calculated shift (7.80 cm^{-1}) from the HCN monomer.

The Stark spectra for HCN-Zn_4 have a very poor signal-to-noise ratio and despite our best efforts, only limited dipole moment information was attainable. Through considerable experimental effort, we were able to determine an upper and lower limit of 6 Debye and 4 Debye, respectively.

6.5 Discussion

Up to this point, we compared the individual HCN-Zn_n complexes with their corresponding counterparts in the previous HCN-Mgn study. In the remainder of this paper, we will report the overall pattern similarities and differences between the two metal cluster-adsorbate systems. Let us begin by inspecting the overall frequency shift pattern of the HCN-Zn_n complexes. Figure 11 shows the plot of two different properties of HCN-Zn_n and HCN-Mgn as a function of metal cluster size, namely the experimental frequency shift from the n$-$1 cluster, and the calculated dipole moment as a function of cluster size. The similarity in the frequency shift patterns is immediately apparent. The $n = 1 - 3$ clusters follow a pattern of increasing frequency shift with the addition of subsequent metal atoms. The larger frequency shift of the magnesium clusters are due to the larger polarizability of the magnesium atoms when compared to zinc. This behavior is well known in weakly bound complexes and is explained by the increased interaction between the polarizable metal atom and the increased dipole moment of the vibrationally excited HCN molecule. In the previous HCN-Mg_n study we showed that the primary means of interaction between the HCN and magnesium clusters with n$= 1 - 3$ was a result of a dipole induced polarization, i.e. physical bonds, whereas the

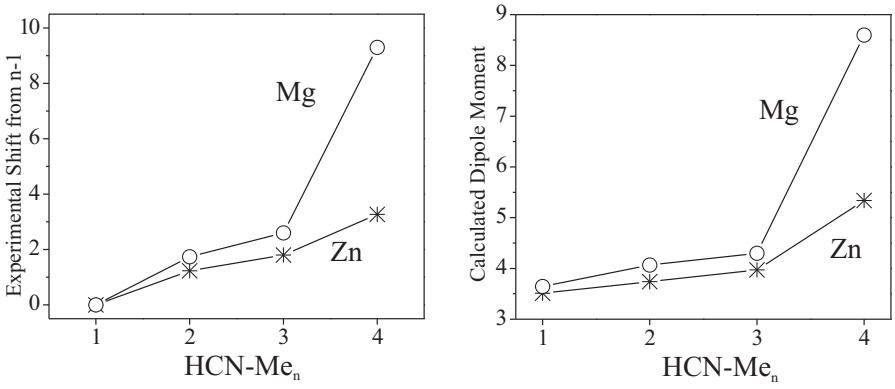

Figure 6.11: A comparison of the relative frequency shift (a) and calculated dipole moment (b) of HCN-Zn$_n$ and HCN-Mg$_n$. The both plots illustrate the similarity for the n=3 complexes and difference for the n=4 complex.

HCN-Mg$_4$ began to show the signs of a dative bond through the transfer of charge from the lone-pair on the nitrogen and to the atop site of the Mg$_4$ cluster.

The HCN-Zn$_n$ clusters, while retaining the overall structure of the magnesium clusters, do not interact with the HCN as strongly. It appears that the HCN-Zn$_4$ complex follows a monotonic trend with increasing n. For example, as shown in Figure 11, the smooth increase in frequency shift and dipole moment for the HCN-Zn$_n$ clusters is in sharp contrast to the large "jump" in frequency shift and dipole moment for the HCN-Mg$_4$ cluster. The mechanism for this weaker interaction lies primarily in the smaller polarizability of zinc (6.4 Å^3) [158] as compared to magnesium (10.6 Å^3) [158], but also can be traced to the more weakly bound nature of the bare zinc clusters themselves. For example, the extremely large dipole moment of HCN-Mg$_4$ (8.6 D) was attributed to the charge donation of the lone-pair in HCN to the LUMO of the Mg$_4$ cluster, a LUMO that was the direct result of the increased hybridization of the 3s and 3p orbitals in magnesium. Indeed, this large degree of hybridization has been determined to be the cause of Mg$_4$'s small bond length and large atomization energy when compared to the smaller clusters [198].

Both magnesium and zinc have very similar electronic configurations and it is this connection that is at the heart of the overall similarity of the spectra presented here and previously [181]. Does the smaller dipole moment and smaller relative frequency shift of HCN-Zn$_4$ point to a smaller degree of hybridization of the 4s and 4p orbitals of zinc?

In order to investigate the difference between the HCN-Zn$_n$ and HCN-Mgn clusters it is useful to first look to the bare clusters. First, let us examine the atomic spectroscopy

data available for the two metals under discussion. Magnesium's lowest electronic transition (3s3p⟵3s2) is 21850 cm^{-1} 15068, compared to zinc's (4s4p⟵4s2), which is 32311 cm^{-1} [199]. Already it is apparent that zinc must overcome a larger energy gap to hybridize with the first available empty orbital when compared to magnesium. The effect of this band gap has been addressed previously when comparing the small alkaline earth metal clusters [198]. In particular, Bauschlicher et. al. [198] pointed out, in comparing Be_4, Mg_4 and Ca_4, that this gap is important in understanding the degree of ns np hybridization, and thus the relative bond energies of each alkaline earth metal cluster. However, Bauschlicher also pointed out that one could not disregard the effects of size in understanding the relative hybridization patterns in each cluster. For example, although Be and Mg have very similar atomic excitation energies (2s2p 2s2 = 21979 cm^{-1} for beryllium and 3s2p 3s2 = 21850 cm^{-1} for magnesium), Be_4 is the more strongly bound than Mg_4 as well as having a greater degree of hybridization [198]. This difference in bonding strength is a result of the extremely diffuse nature of the 3p orbital relative to the 2p orbital in magnesium, so there is a larger energy "tax" to pay for the increased stabilization offered by hybridization.

We can now turn our attention back to the zinc and magnesium clusters. Table 4 displays the natural populations calculated at the MP2 level for both metal clusters. The populations support our previous conclusions, namely for clusters of $n < 3$ in size there is little hybridization and are therefore predominately van der Waals in nature. Notice, however, that both metals increase their levels of p population in the $n = 4$ clusters. This is certainly no surprise for Mg_4, which has been calculated many times before [165, 133, 198, 200, 201, 135], but considering the much larger gap between the 4s and 4p orbitals in zinc, the degree to which the Zn_4 hybridizes seems anomalous. If, however, one considers the much smaller size of zinc due to its larger nuclear charge, it seems reasonable that zinc is able overcome its larger "energy penalty" for hybridization and form a relatively stable complex, just as Be4 was calculated to be more stable than Mg_4 [198].

It is interesting to note that even though Zn_4 has a relatively large bond energy per atom and a relatively high degree of hybridization, the interaction with HCN is much less than what was observed in HCN-Mg_4. This is evident in the frequency shift data and the dipole moment data shown in Figure 11. Although our experiments were only able to provide an estimate of the dipole moment of HCN-Zn_4, the calculated dipole moment of 5.34 D is consistent with the weak interaction between HCN and Zn_4. It appears that the charge transfer that accounted for the large dipole moment in HCN-Mg_4 does not occur in HCN-Zn_4 and we can conclude that Zn_4 has a smaller electron affinity than Mg_4. Recently this conclusion has been given further weight through the private communication of Kit

Table 6.4: The natural populations for Zn_n and Mg_n, n=1-4. Both were calculated using the MP2 density. Calculations on Zn clusters used the ECP and associated valence basis set given in the text and Mg clusters used the 6-311++G(3df,3pd) basis set.

	4s	4p		3s	3p
Zn	1.95	0.05	Mg	1.95	0.05
Zn_2	1.95	0.06	Mg_2	1.94	0.05
Zn_3	1.93	0.07	Mg_3	1.88	0.1
Zn_4	1.83	0.16	Mg_4	1.75	0.21

Bowen, where his work on the photoelectron spectroscopy of negatively charged Mg_n and Zn_n clusters have shown that singly charged Zn_4 anions are less stable than their anionic Mg_4 counterparts [202].

6.6 Conclusions

The experimental vibrational shifts and bonding patterns of the HCN-Zn_n (n = 1-4) complexes are very similar to those determined for HCN-Mg_n (n=1-4). The similarity between these two systems is primarily a result of the electronic configurations of magnesium and zinc. Both have closed s orbitals along with low-lying empty p orbitals. This characteristic is what determines the relatively small binding energies in all of these clusters and the fact that all bonds between the HCN and metal cluster are van der Waals in nature.

The differences between the HCN-Zn_n and HCN-Mgn clusters are due to the differences in the polarizability of zinc and magnesium. The smaller polarizability results in a weaker dipole induced polarization of the zinc clusters and therefore a smaller vibrational red-shift. Although we were unable to acquire a precise dipole moment measurement for HCN-Zn_4, the calculated dipole moment was significantly smaller than that of the HCN-Mg_4 complex, indicating that little or no charge transfers from the lone pair on the nitrogen in HCN to the LUMO of the Zn_4 cluster. This is most likely a result of zinc's energy gap between the filled 4s valence orbital and the empty 4p orbital, which is larger than the gap between the 3s and 3p orbitals in magnesium. The larger gap results in Zn_4's LUMO having less p character, which in turn makes Zn_4 a weaker electron acceptor than Mg_4.

Chapter 7

HCN-Cu$_n$ (n=1-3)

The structures, C-H stretching frequencies, and dipole moments of HCN-Cu$_n$ (n=1-3) clusters are determined through high-resolution infrared spectroscopy. The complexes are formed and probed within superfluid helium droplets, whereby the helium droplet beam is passed over a resistively heated crucible containing copper shot and then through a gas HCN pickup cell. All complexes are found to be bound through the nitrogen end of the HCN molecule and on the "atop site" of the copper cluster. Through the experimental C-H vibrational shifts of HCN-Cu$_n$ and *ab initio* calculations, it was found that the HCN-metal interaction changes from a strong van der Waals bond in n=1 to a partially covalent bond in HCN-Cu$_2$ and HCN-Cu$_3$. Comparisons with existing infrared data on copper surfaces show that the HCN-Cu$_n$ bond must begin to weaken at very large copper cluster sizes, eventually returning to a van der Waals bond in the bulk copper surface case.

7.1 Introduction

The study of metal clusters and their interactions with small molecules is motivated, in large part, by the possibility of using these smaller, more computationally manageable, clusters as models for the interactions that take place on bulk metal surfaces [153, 152, 151, 4, 203, 15, 16, 102]. A fundamental understanding of such interactions would have great value to many areas, including catalysis, materials and corrosion science. It is well documented, however, that metal clusters, transition metal clusters in particular, have properties that can vary wildly with cluster size and often share no similarities with their bulk counterparts [4, 88]. Arguably, the most famous example of this behavior is found in small gold clusters [6, 12]. When finely dispersed onto a metal-oxide support, these nanoscale gold particles exhibit a previously unanticipated low-temperature catalytic activity for the combustion, oxidation,

reduction and hydrogenation of numerous molecules [204]. Understanding the fundamental causes for this dramatic size dependence of metal clusters is a major driving force in cluster science.

In this paper we present the high-resolution infrared spectra of HCN-Cu_n (n=1-3). The monoligated copper clusters were formed in superfluid helium droplets, which are at a temperature of 0.4 K. The use of superfluid helium droplets as a "nanoscale laboratory" has been well demonstrated in the last decade [51, 118, 205, 206, 52]. In one of many applications of this technique, we have shown the particular usefulness of superfluid helium droplets as applied to the study of metal cluster-adsorbate systems [66, 181]. One of the unique aspects, and greatest advantages, of helium droplets is that the free rotation of solvated molecules is permitted, due to the weakly interacting nature of the quantum fluid [39, 207]. The resulting rotationally resolved spectra, when acquired using the appropriate high-resolution spectroscopic techniques, give valuable structural information about the molecular complex solvated with the droplet. Although the rotational constants measured within the droplets are typically reduced by a factor of 2.5 $\pm$ 0.5 [32, 33, 30, 34] relative to their gas-phase counterparts, the symmetry of the spectra are unaffected [39].

In addition to structural data, infrared spectroscopy can also provide valuable information about the nature of the interaction between metal cluster and adsorbate. While many types of spectroscopy have been applied to molecules solvated within helium droplets [51, 118, 205, 206, 52], infrared spectroscopy is particularly well suited, because vibrational transitions are only slightly perturbed (< 1 cm^{-1}) [208] from their corresponding gas-phase values. The resulting data can therefore be reliably compared to *ab initio* calculations and to previous experiments. One such experiment was performed in the laboratory of Michael Trenary at the University of Illinois, Chicago [1]. Celio et al. [1] used both temperature-programmed reaction spectroscopy (TPRS) and reflection absorption infrared spectroscopy (RAIRS) to investigate the properties of HCN on a Cu(100) surface. They found that HCN was weakly bound, nitrogen-end down, perpendicular to the copper surface and on an atop site. In this geometry and at temperatures below 90 K, the C-H stretch was measured to be 3294 cm^{-1}. This study was a major inspiration for our choice of copper in the experiments to be presented below. It offers the opportunity to compare the H-CN stretches in clusters, [HCN-Cu_n (n=1-3)] and adsorbed on surfaces [HCN-Cu(100)], thus gaining valuable insight into the evolution of the metal cluster-adsorbate interaction as a function of metal cluster size.

7.2 Experimental

The experimental apparatus has been discussed elsewhere [119, 59]. Helium droplets were formed by expanding ultra-pure helium through a 5 μm nozzle. The nozzle was cooled to temperatures in the range of 19 K to 16 K and backed with 60 bar of helium pressure. These conditions corresponded to average droplet sizes of about 6000 to 12000 helium atoms, respectively. After droplet formation and skimming, the droplet beam was passed just over the top of a resistively heated alumina crucible that contained copper shot. Experimental conditions for pickup of one copper atom, on average, required temperatures of about 1130° C (vapor pressure = 1 x10^{-3} Torr) , with increasing temperatures for higher order clusters, not exceeding 1250° C. After the copper pickup, the droplets were then passed through a gas pick-up cell containing HCN gas. The pressure inside this cell was maintained at pressures below 4 x 10^{-6} Torr to ensure the pickup of a single HCN molecule/droplet, on average.

The HCN-Cu_n seeded droplets were passed through the laser interaction region, where the C-H stretch of HCN was excited by an F-center laser (Burleigh FCL-20), operating on crystal 3 (RbCl:Li). Subsequent vibrational relaxation to the helium droplet resulted in the evaporation of approximately 600 helium atoms. The depletion of the droplet beam was then detected by a liquid helium cooled bolometer [192]. The laser was amplitude-modulated, and the corresponding bolometer signals were measured using phase sensitive detection methods. The details associated with tuning and calibrating the laser can be found elsewhere [193].

An electric field was applied to the laser interaction region, using two metal electrodes, in order for the acquisition of pendular or Stark spectra. A considerable enhancement of the signal levels was obtained by using a large electric field (24 kV/cm) to record pendular spectra [60, 61], which was particularly useful when searching for new unknown species like those presented here. At more modest electric fields [78] (1-4 kV/cm), the resulting Stark spectra provided accurate measurements of the dipole moments of the HCN-Cu_n complexes.

7.3 Results

7.3.1 Computational details

All MP2 calculations were performed with Molpro [186]. All DFT calculations were performed with Gaussian 03 [187]. The relatively large number of electrons associated with copper clusters required the use of effective core potentials (ECP) in order for manageable calculations. We chose to use the small core Stuttgart-Dresden ECP (ECP10MDF) [184] due to its familiarity and availability within Molpro. The Stuttgart-Dresden valence basis

Table 7.1: The bond length (R_e), harmonic frequency (ω_e) and binding energy (D_e) are compared with previous work.

Cu_2 $^1\Sigma_g^+$	R_e(Å)	$\omega_e(cm^{-1})$	D_e(eV)
RMP2	2.2178	277.01	1.74
Expt [212]	2.2193	266.46	2.08
CASPT2+RC [213]	2.215	276.8	1.97

Table 7.2: The $^2B_2$ electronic state of copper trimer is a Jahn-Teller distorted obtuse triangle. The bond length of legs (R_e) and bond angle (θ) of the triangle are given. The symmetric stretch ($\omega_{S.S.}$), asymmetric stretch ($\omega_{A.S.}$) and bend frequency (ω_{bend}) are also given.

Cu_3 $^2B_2$	R_e(Å)	$\theta(^o)$	$\omega_{S.S.}(cm^{-1})$	$\omega_{A.S.}(cm^{-1})$	$\omega_{bend}(cm^{-1})$
RMP2	2.271	66.79	271	152	123
Schaefer [214]	2.31	68	253	159	107
Berces [215]	2.335	65.6	293	142	158

set for copper [6s,5p,3d] was augmented with 2f functions and 1g function, as optimized by Martin and Sundermann [189]. The 6-311++G** basis set was used for HCN.

In order for a better comparison between each cluster, we chose to use restricted open-shell MP2 (ROMP2) methods for HCN-Cu and HCN-Cu_3 as implemented in Molpro. RMP2 methods were used to calculate HCN-Cu_2. It should be noted that with the open-shell systems of HCN-Cu and HCN-Cu_3, restricted open shell MP2 (ROMP2) methods gave much better harmonic frequency results than methods using unrestricted open shell (UMP2). In fact, preliminary calculations that used UMP2 gave large blue shifts in the C-H stretch frequency for HCN upon complexation with a single copper atom as well as returning unrealistic IR intensities. Being that we were armed with the experimental C-H stretch in the HCN-Cu complex, we disregarded the UMP2 calculations.

The abundance of DFT calculations on copper clusters [209, 210, 211] prompted us to perform our own DFT calculations on the HCN-Cu_n clusters. DFT methods were also chosen because of the possibility of comparing the calculations reported here with future calculations on larger copper cluster sizes that will almost certainly require the computational savings offered by DFT. The B3LYP functional was used for all cluster calculations along with the same basis sets that were used for the MP2 calculations.

Comparisons of our bare copper calculations with previous work [214, 215, 213, 212]

Table 7.3: The RMP2 and DFT harmonic vibrational red-shifts (from HCN monomer), dipole moments and binding energy between HCN and Cu_n.

	$\Delta\nu$ (cm^{-1})	μ (Debye)	D_e (kcal/mol)
HCN-Cu			
ROMP2	11.64	7.957	1.73
B3LYP	17.28	5.941	2.92
$HCN-Cu_2$			
RMP2	7.28	6.322	16.2
B3LYP	5.95	6.323	14.4
$HCN-Cu_3$			
ROMP2	6.14	6.780	23.1
B3LYP	4.99	5.760	20.6

and direct comparisons with our experimental data led us to believe that our choices for computational methods were sound. Table 7.1 gives the results of our MP2 calculations (closed shell) on Cu_2, along with previous experiments and theory. There is near quantitative agreement between our calculated bond length and Bernath's experimentally determined bond length of copper dimer [212]. The calculated frequency is in excellent agreement as well. Looking to the other best calculation available [213], one can see that we have quantitative agreement with the CASPT2+RC calculation of Pou-Amrigo et. al [213]. The near perfect agreement of our MP2 calculations with experimental results is most likely due to a fortuitous cancelation of errors and should not be taken as evidence for MP2's superiority over other methods. Table 7.2 compares our bond lengths, bond angles and frequencies with some previous Cu_3 calculations. Overall, the Jahn-Teller distorted trimer calculated with ROMP2 methods is in excellent agreement with previous work [214, 215].

The results of our RMP2 and DFT calculations for the HCN-Cu_n clusters are given in Figure 7.1 and in Table 7.3. There are no existing calculations on such clusters, but HCN should share many bonding similarities with the widely calculated model ligand, CO. HCN and CO are isoelectronic and both sp hybridized ligands interact with metal clusters through a sigma donation mechanism as well as accept charge through the anti-bonding pi orbitals. Fournier [211] has reported the theoretical structures of CO-Cu_n (n=1-3) and compared them to the available matrix isolation infrared data [216]. Our global minimum structures

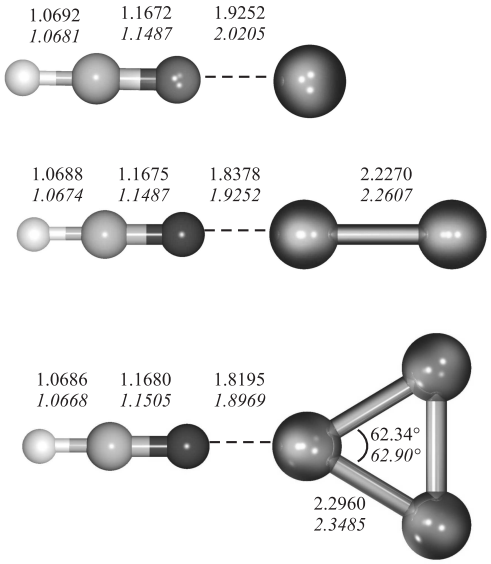

Figure 7.1: Calculated structures of three HCN-Cu$_n$ complexes. The bond lengths of the MP2 (upper) and DFT (lower) calculations are shown. See text for basis set information.

are all consistent with these previous studies.

7.3.2 Pendular Spectrum

We begin the presentation of our experimental results with a long pendular survey scan of the free stretch region of HCN (Figure 7.2). The well-known HCN monomer and dimer pendular peaks [64] are labeled and are extremely weak due to the relatively low HCN pressure used for this scan. The peaks not due solely to HCN multimers were initially assigned with the use of signal optimization techniques and are labeled explicitly in Figure 7.2. The pickup of dopants within the helium droplet beam is determined by the helium droplet size distribution and the conditions of the pickup cell, both of which are known [48, 49, 27, 51, 52]. Therefore, while "parking" the laser on top of a particular pendular peak we can vary the pick-up cell pressure and oven temperature (metal vapor pressure) while watching the signal increase or decrease, depending on that particular system's optimum conditions. Table 7.4 gives the oven temperature, average droplet size, and HCN pick-up cell pressure for each of the assigned peaks in Figure 7.2. The conditions for the optimal signal for HCN are shown for comparison purposes. The relatively large droplet sizes required for the HCN-Cu$_n$ complexes are due primarily to the large bond energy released when the complexes are formed within the droplet. It is important to note that our detection method requires that, after the complex has been formed within the droplet, a portion of that droplet must remain in

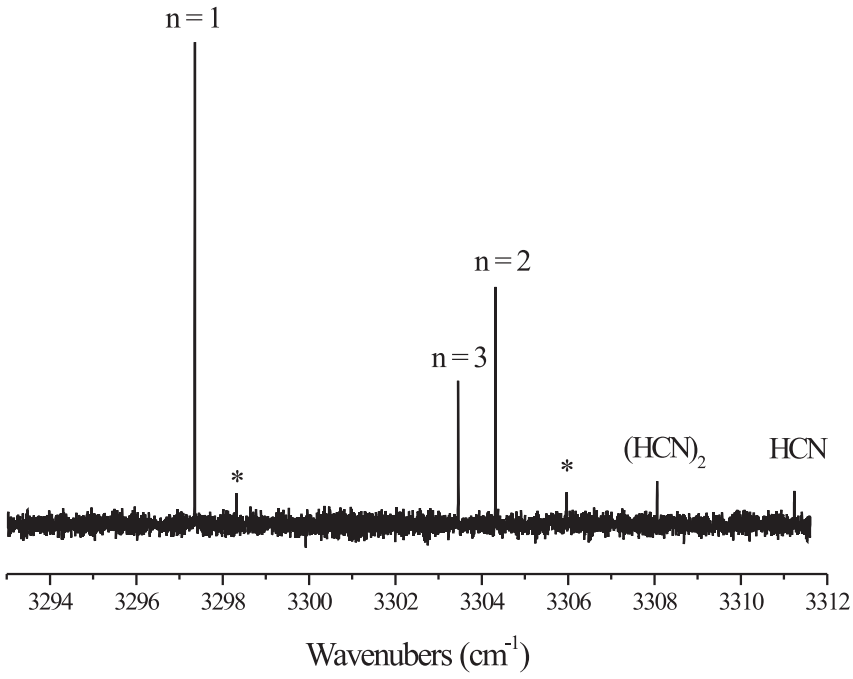

Figure 7.2: Pendular survey scan of the free C-H stretch region of HCN in the presence of copper. The bands assigned to the three HCN-Cu$_n$ complexes are labeled. The asterisks designate species due to $(HCN)_2$-Cu complexes

Table 7.4: The optimal oven temperature, droplet size ($\overline{N}$), and HCN pressure for HCN and the HCN-Cu_n complexes.

	Oven Temp (°C)	$\overline{N}$	HCN Pressure (Torr)
HCN	—	2300	8.0 x 10^{-6}
HCN-Cu	1030	5700	3.8 x 10^{-6}
HCN-Cu_2	1130	7200	3.4 x 10^{-6}
HCN-Cu_3	1200	12000	2.8 x 10^{-6}

order for a signal to be detected by the bolometer. For example, the formation of copper dimer from two copper atoms releases about 46 kcal/mol of energy [158]. Additionally, the subsequent complexation energy between Cu_2 and HCN releases another 16 kcal/mol of energy (Table 7.3). This large energy release results in the evaporation of about 4000 helium atoms from the droplet (assuming 5 cm^{-1} per helium atom) [27], and means that any droplet below the critical size of about 4000 He atoms will contribute nothing to the phase sensitive bolometric detection method . Notice also in Table 7.4 that a much lower HCN pressure was required for the optimization of each signal. The low pressure requirements are due to the fact that larger droplets have larger pick-up cross sections.

In previous work we noted that the C-H frequency red-shifts increased with increasing metal cluster-adsorbate interaction energy [181, 162]. Interestingly, here we find that the largest frequency shift is due to the HCN-Cu complex, which has the smallest binding energy (Table 7.3), while the larger binding energy complexes such as HCN-Cu_2 and HCN-Cu_3 are red-shifted to a lesser degree. This vibrational pattern is inconsistent with what would be expected within Dykstra's theory [217] of vibrational frequency shifts due to hydrogen bonding and hints at a fundamental change in bonding when going from HCN-Cu to HCN-$Cu_{n\geq 2}$. This unexpected frequency shift pattern will be discussed further below.

7.3.3 HCN-Cu

In addition to the signal optimization methods reported above, definitive spectral assignments as well as direct structural evidence of each complex was obtained through high-resolution infrared spectroscopy. Figure 7.3 shows the field-free, rotationally resolved IR spectrum of HCN-Cu. The spectrum is that of a linear rotor (no Q-branch). The simulated spectrum shown below the experimental spectrum in Figure 7.3 was obtained by fitting B (rotational constant) and D (centrifugal distortion constant), in the ground and excited state, of a linear rotor Hamiltonian. The results of the fit are given in Table 7.5 and are

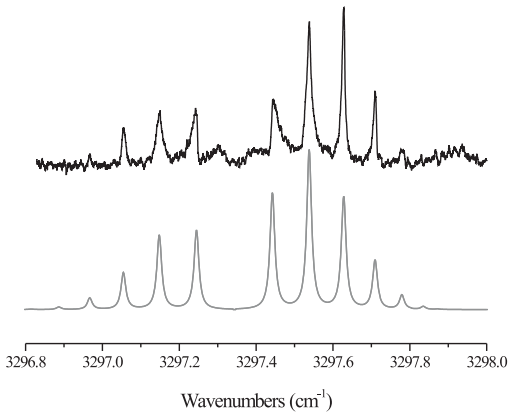

Figure 7.3: The field free spectrum of HCN-Cu. The simulated spectrum, shown below the experimental, was fit using a linear rotor Hamiltonian. This spectrum was acquired with an average droplet size of 5700 He atoms.

consistent with the calculated structure shown in Figure 7.1.

As this complex has never been observed in the gas-phase, the only comparison that can be made with our results is with theoretical calculations. The experimental ground rotational constant, B″, is reduced by a factor of 2.56 and 2.42 for the MP2 and B3LYP equilibrium B constants, respectively. This reduction factor is typical for molecules solvated within helium and is due to the adiabatic following of helium density in the first solvation shell around the solvated molecule [30, 35, 218]. The degree to which the helium density increases the moment of inertia is a very challenging theoretical problem that has yet to be quantitatively resolved [118, 219, 220, 70]. Fortunately, enough rotational constants of molecules that are known in the gas-phase have been measured within helium droplets, and it has been found that the constants typically are reduced by a factor of 2.5 $\pm$ 0.5 [118]. The distortion constants, D, given in Table 7.5 are very large, which is consistent with previous work in helium droplets [51, 118, 52].

The Stark spectrum of HCN-Cu is shown in Figure 7.4. The simulated spectrum shown below the experimental spectrum was generated using our "pendular rotor" program, which diagonalizes the Stark Hamiltonian, using an asymmetric top basis set up to j=15, m=12, and k=15. The previously determined rotational constants are combined with the known electric field present during the spectrum's acquisition, and the dipole moment was adjusted until a good fit was obtained. Several spectra were taken at varying fields with the average

Table 7.5: The experimental vibrational frequency (ν_0), vibrational red-shift from HCN-monomer ($\Delta\nu_0$), linear rotor rotational constants (B and D) and dipole moment (μ) of HCN-Cu. The calculated rotational constants, helium droplet to gas phase rotational constant ratio, and calculated dipole moments are also given. The dipole moment is reported in Debye, while all other units are given in wavenumbers (cm^{-1})

	Expt		ROMP2	B3LYP
ν_0	3297.34			
$\Delta\nu_0$	13.9	$\Delta\nu_0$	11.64	17.28
B″	0.0495	B_e	0.1270	0.1201
B′	0.0493			
D″	$9.1x10^{-5}$			
D′	$1.0x10^{-4}$			
μ	6.40 ± 0.08	μ	7.957	5.941

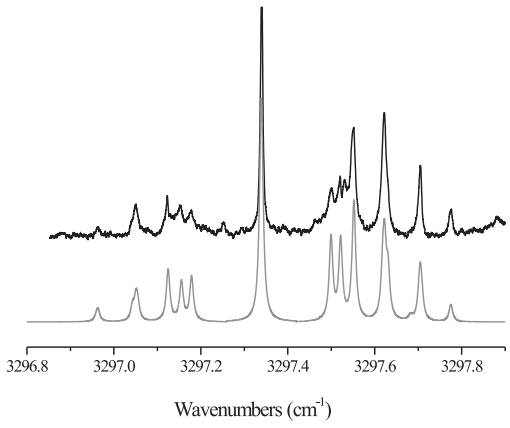

Figure 7.4: The Stark spectrum of HCN-Cu taken at a field of 1.184 kV/cm.

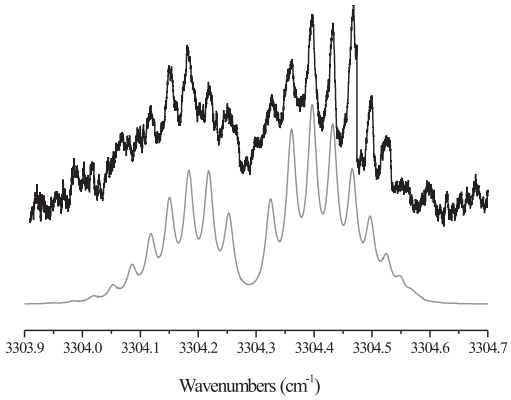

Figure 7.5: The field free spectrum of HCN-Cu_2. The simulated spectrum, shown below the experimental, was fit using a linear rotor Hamiltonian. This spectrum was acquired with an average droplet size of 7200 He atoms.

dipole moment of all fits being 6.40 ± 0.08 Debye. As expected, the experimental dipole moment is somewhat smaller than the ROMP2 dipole moment(6.780 D) which has been explained by the shielding effect the helium solvent has on the electric field experienced by the solvated molecule [120]. The DFT dipole moment (5.760 D) underestimates the dipole moment but, considering DFT's poor performance with weakly bound clusters [221], this is not surprising.

7.3.4 HCN-Cu_2

Having convincingly assigned the HCN-Cu complex, we now move on to the remaining bands shown in Figure 7.2. The field free spectrum of the band assigned to HCN-Cu_2 is shown in Figure 7.5. This spectrum was acquired with a higher copper oven temperature (1150°C) and a larger average droplet size (7200 He atoms) than the HCN-Cu spectrum, indicative of a complex of larger size. The symmetry of the spectrum gives conclusive evidence that it is due to a linear rotor (no Q-branch), which is consistent with our calculated structure for HCN-Cu_2 (Figure 7.1).

The simulated spectrum shown in Figure 7.5 was generated using a linear rotor Hamiltonian. The rotational constants determined from the fit are given in Table 7.6. The experimental B″ rotational constant, 0.0178 cm^{-1}, is reduced from the calculated rotational constant (0.03741 cm^{-1}) by a factor of 2.1 and 2.0 for the RMP2 and DFT calculations,

Table 7.6: The experimental vibrational frequency (ν_0), vibrational red-shift from HCN monomer ($\Delta\nu_0$), linear rotor rotational constants (B and D) and dipole moment (μ) of HCN-Cu_2. The calculated rotational constants, helium droplet to gas phase rotational constant ratio, and calculated dipole moments are also given. The dipole moment is reported in Debye, while all other units are given in wavenumbers (cm^{-1})

	Expt		RMP2	B3LYP
ν_0	3304.29			
$\Delta\nu_0$	6.92	$\Delta\nu_0$	7.28	5.95
B″	0.0178	B_e	0.03741	0.03601
B′	0.0181			
D″	$8.4x10^{-5}$			
D′	$1.4x10^{-5}$			
μ	6.7 ± 0.3	μ	6.322	6.313

respectively. As stated above, this reduction in rotational constants in helium droplets is consistent with previous experiments.

Figure 7.6 gives the Stark spectrum of HCN-Cu_2 taken at a field of 1.05 kV/cm. The result of the fit gave a dipole moment of 6.7 ± 0.3 Debye. This value is in fair agreement with both the MP2 and DFT theoretical dipole moments, calculated to be 6.322 Debye and 6.323 Debye, respectively. (Table 7.6). As it was stated above, we typically measure slightly smaller dipole moments (1-2%)in helium droplets, due to the shielding effect of the helium solvent [120]. In this case we measure a dipole that is larger than the calculated "gas-phase" dipole and attribute. Considering the unambiguous assignment of this band and our confidence in the given Stark spectrum, we attribute the discrepancy to failings in the calculation.

7.3.5 HCN-Cu_3

The final peak associated with copper and HCN examined in this study is HCN-Cu_3. Its field free spectrum is given in Figure 7.7. This band optimized at very large average droplet sizes and high oven temperatures(Table 7.4). The rotational structure of Figure 7.7 is closely spaced and somewhat unresolved, nevertheless, the overall P-, Q- and R-branch structure is clearly that of a parallel band of an asymmetric top. The result of a fit to the A, B, C, and D_j constants of the asymmetric top Hamiltonian is shown below the experimental spectrum. A line width of 0.014 cm^{-1} was used. The collected rotational constants are given in Table 7.7 and, when compared to the calculated values, are all within the expected factor of 2.5 ± 0.5, further providing evidence for the assignment of HCN-Cu_3.

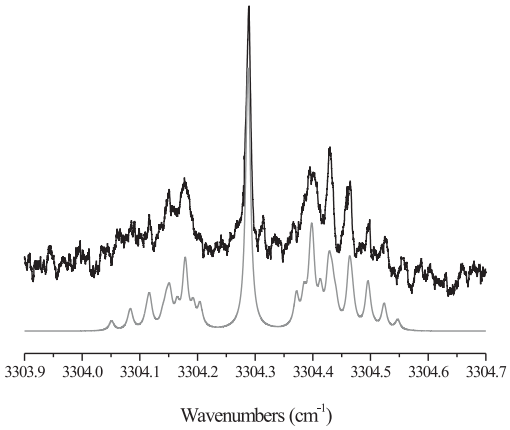

Figure 7.6: The Stark spectrum of HCN-Cu_2 taken at a field of 1.049 KV/cm.

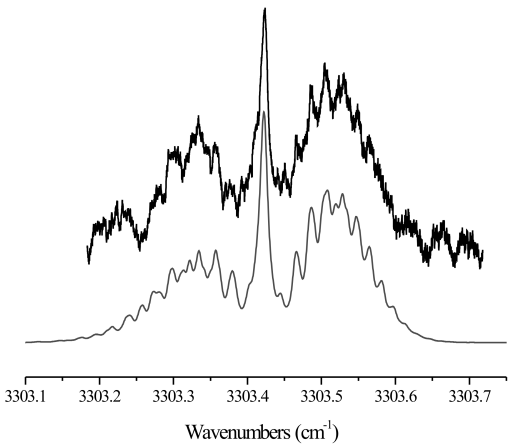

Figure 7.7: The field free spectrum of HCN-Cu_3. The lower spectrum was generated using an asymmetric top Hamiltonian.

Table 7.7: The experimental vibrational frequency (ν_0), vibrational red-shift ($\Delta\nu_0$), asymmetric top rotational constants averaged over the ground and vibrationally excited states ($\overline{A}$, $\overline{B}$, $\overline{C}$, D_j) and dipole moment (μ) of HCN-Cu_3. The calculated equilibrium rotational constants (A_e, B_e,C_e) and calculated dipole moments are also given.

	Expt		ROMP2	B3LYP
ν_0	3303.42			
$\Delta\nu_0$	7.79	$\Delta\nu_0$	6.14	4.99
$\overline{A}$	0.045	A_e	0.09347	0.08920
$\overline{B}$	0.013	B_e	0.03332	0.03207
$\overline{C}$	0.0091	C_e	0.02456	0.02359
$\overline{D_j}$	2 x 10^{-7}			
μ	5.5 $\pm$ 0.5	μ	6.780	5.764

Although the rotational structure of the field free spectrum of HCN-Cu_3 is unresolved, an accurate fit was still possible through the fitting of the overall shape of the spectrum. This course of action was possible because we have knowledge of the droplet's temperature, namely 0.4 K. Using the resulting rotational constants, the fitting of the overall shape of the Stark spectrum was used to determine the dipole moment of HCN-Cu_3, which is shown in Figure 7.8. The dipole moment of HCN-Cu_3 was determined to be 5.5 $\pm$ 0.5 D. This value is in much better agreement with the B3LYP calculated dipole moment (5.764 D) than the ROMP2 dipole moment (6.780 D).

7.4 Discussion

The structures of the HCN-Cu_n clusters presented in this report all share a consistent bonding property, namely that the HCN binds to the copper monomer, dimer, and trimer through the nitrogen end of the HCN and on the "atop" site. This similarity in bonding not only offers the opportunity to more easily compare each cluster with one another, but also allows for the meaningful comparison with HCN bound to a Cu(100) surface, since HCN is known to bind (nitrogen-end down) to bulk Cu(100) perpendicularly to the surface and at an atop site. As mentioned above, RAIRS and TPRS was used to determine the binding geometry of HCN to Cu(100) at low temperature [1], so comparisons of the C-H stretching frequency of HCN at the bulk copper limit (3294 cm^{-1}) are possible. In a related theoretical study [222], the perpendicular binding geometry to the Cu(100) surface was corroborated through DFT calculations of HCN on a Cu_{13} model cluster. The theoretical study also reported the binding

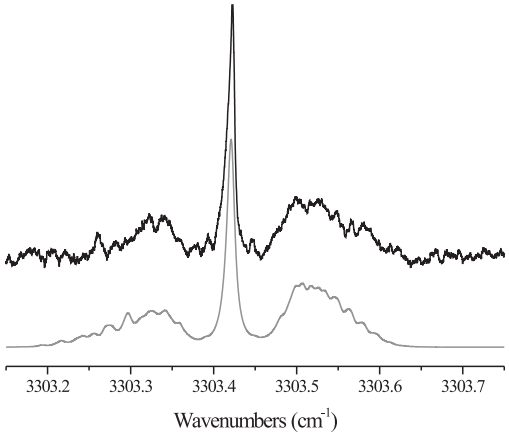

Figure 7.8: The Stark spectrum of HCN-Cu_3 taken at a field of 1.041 KV/cm.

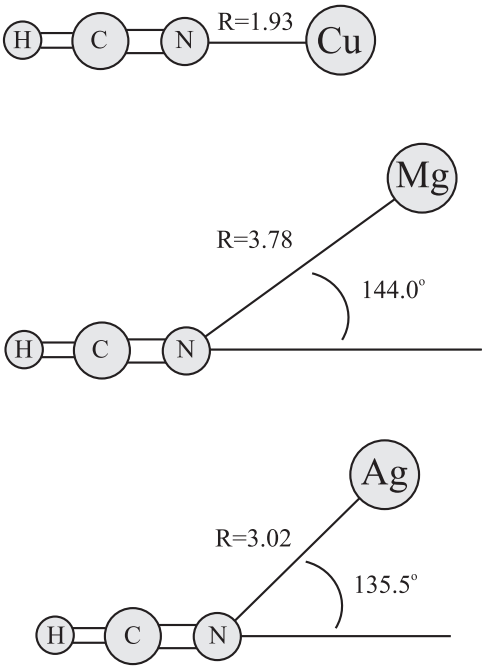

Figure 7.9: Representative geometries of several HCN-Metal complexes calculated using MP2 methods.

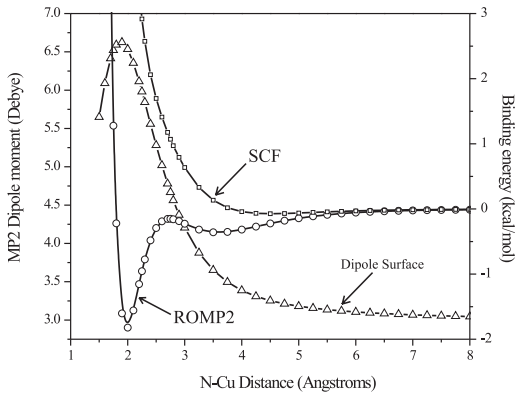

Figure 7.10: The 1-D UMP2 potential energy surface (red) of HCN-Cu calculated at distances between the nitrogen on HCN and the nearest Cu atom (See Figure 7.3). The PES of the SCF energy is given in black.

energy of HCN on copper as 3.54 kcal/mol and concluded, like Celio and coworkers, that HCN is physisorbed to the copper surface.

It is interesting to note that in our previous [72] and current studies [223], all of the binary HCN-metal atom complexes were calculated to be bound to the nitrogen in a bent geometry and at large bond lengths, while in the HCN-Cu case, a relatively short, linear bond was calculated. These differences are summarized in Figure 7.9. The unique geometry for HCN-Cu can be rationalized by examining the van der Waals radii of each metal atom. The copper atom radius (1.40 Å) is much smaller than Mg (1.73 Å) or Ag (1.72 Å) [196], and, as a result, the nitrogen and copper atom can approach more closely. This close proximity permits the donor-acceptor interaction to take place between the copper atom and the HCN molecule [224]. The energy of the bond between HCN and Cu remains relatively weak (ROMP2=1.73 kcal/mol) in HCN-Cu, due to the balance between the attractive donor-acceptor energy and the repulsive steric interaction [224]. In the case of the Mg and Ag atoms, Pauli repulsion dominates the interaction potential at nitrogen-metal atom distances required for significant charge transfer. In other words, the more diffuse nature of electron density around Mg and Ag prevents significant donor-acceptor interactions from taking place and the atoms are forced to balance their dipole-induced dipole polarization interaction and dispersion interaction by bending closer to the C-N triple bond.

The donor-acceptor viewpoint presented above is consistent with the counterpoise corrected [111] ROMP2 potential energy surface shown in Figure 7.10. Coming in from large

N-Cu distances, the first shallow minimum is located at about 3.6 Å; distances reminiscent of the HCN-Mg and HCN-Ag bond distances shown in Figure 7.9. Moving in to smaller distances, the potential rises and peaks at approximately 2.8 Å. It is here that the steric repulsion begins to be overtaken by the attractive charge transfer interaction, caused mainly by the donation of charge from the nitrogen lone pair to the half-filled 4s orbital on Cu. The importance of electron correlation in the HCN-Cu complex is demonstrated by the SCF potential energy surface given in Figure 7.10, given that there is virtually no binding at the SCF level.

Due to the extremely cold temperature (0.4 K) and rapid cooling capacity of the droplet, the trapping of complexes in local minima on the potential energy surface has been clearly demonstrated in helium droplets [44, 65, 64]. The dipole moment surface (calculated using the method of finite fields [186]) is therefore, shown along with the potential energy surface to further convince the reader that we have indeed captured and measured the ro-vibrational spectrum of the structure shown in Figure 7.9. Consider, for example, the possibility that the HCN-Cu complex was trapped in the shallow minimum calculated in Figure 7.10. The measured dipole moment would be closer to 4.2 D, instead of the measured dipole moment of 6.40 D. This dipole moment is convincing evidence for the reported linear structure.

Although the bonding between HCN and Cu is relatively strong (ROMP2 = 1.73 kcal/mol), compared to binding energies between HCN and other metal atoms ($<$ 0.5 kcal/mol), it is still within the van der Waals regime. Indeed, the PES shown in black in Figure 7.10 predicts virtually no bonding between HCN and Cu at the SCF level. The physical bond between HCN and Cu is visualized through the use of a difference density plot in Figures 7.11A and B. ROMP2 densities were unavailable in Molpro so the optimized geometry and densities at the UMP2 level were calculated in Gaussian 03. The electron density difference plot using the DFT density is also given (Figure 7.11B).

Generation of the electron difference density plots involves taking the difference between the electron density of a molecular complex (HCN-Cu), and the densities of a set of non-interacting molecular subunits (HCN and Cu) in the same geometrical arrangement. By looking at the changes in the density between the two cases, one can gain insight into the nature of the intermolecular bonding. In the case of HCN-Cu, Figure 7.11 clearly shows an overall decrease in the electron density between the nitrogen and copper atom for both the UMP2 and B3LYP densities. This decrease is consistent with a non-covalent interaction, and we conclude that HCN is bound to the copper atom through a strong van der Waals bond.

Much of the interest in metal clusters lies in their ability to change their properties with

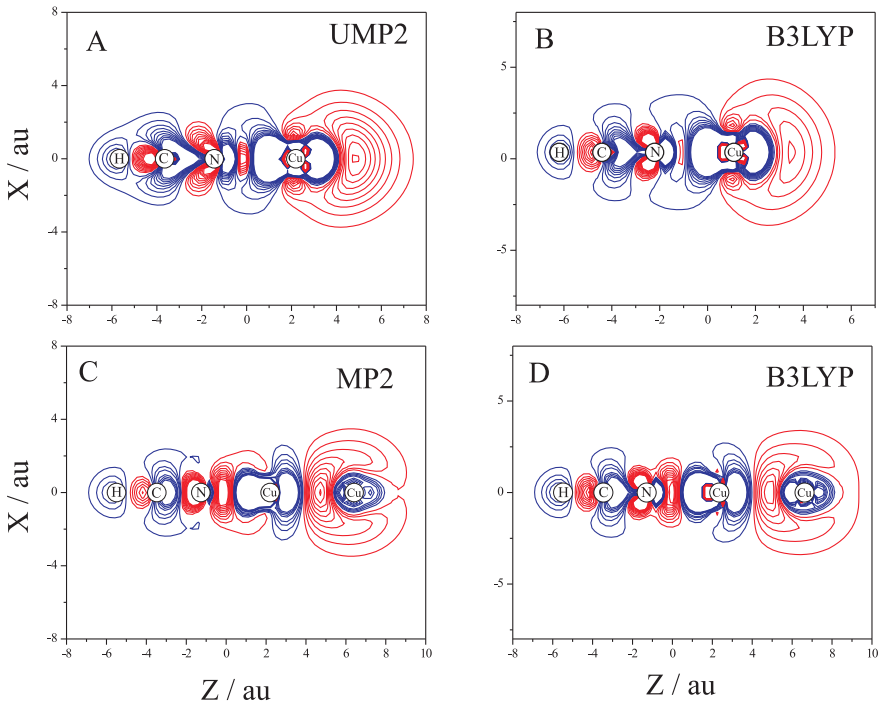

Figure 7.11: Density difference plots for (A) HCN-Cu using the UMP2 density, (B) HCN-Cu using the DFT density, (C) HCN-Cu_2 using the MP2 density and (D) HCN-Cu_2 DFT density. Contours range from -0.005 e/au^3 to +0.005 e/au^3 and are spaced at 0.0005 e/au^3 intervals. Positive and negative contours are given in red and blue, respectively. ECP and basis set information can be found in the text.

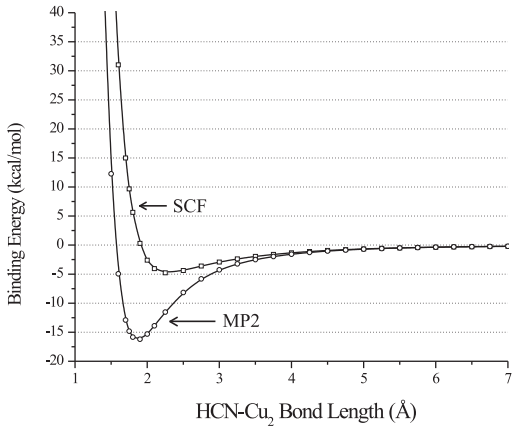

Figure 7.12: The 1-D MP2 potential energy surface (red) of HCN-Cu_2 calculated at distances between the nitrogen on HCN and the nearest Cu atom (See Figure 7.3). The PES of the SCF energy is given in black.

the addition or subtraction of a single atom. As it will be shown below, this is indeed the case when comparing metal-adsorbate interaction in HCN-Cu_2 and HCN-Cu. Figure 7.12 shows the 1-D potential energy surface (PES) of the interaction of HCN and Cu_2. The MP2 PES was calculated at distances between the nitrogen on HCN and the nearest Cu atom on Cu_2 in order for more convenient comparisons among the HCN-Cu_n complexes.

Table 7.1 gives the equilibrium binding energy of HCN-Cu_2 calculated at the MP2 level (16.2 kcal/mol). The same binding energy is reproduced in the PES given in Figure 7.12 and represents an extremely large increase in binding energy relative to the binary HCN-Cu complex. What is particularly interesting is the Hartree-Fock PES curve shown along with the MP2 surface, which shows just under 5 kcal/mol of binding at a N-Cu distance of 2.25 Å. The significant binding at at the SCF level demonstrates that the interaction between HCN and Cu_2 is not as dependent on electron correlation as the HCN-Cu complex was. Furthermore, it is interesting to note that the total MP2 binding energy is more than 3 times greater than the binding energy of a typical hydrogen bond (5 kcal/mol).

The electron density difference maps of HCN-Cu_2, calculated using MP2 and DFT methods, are given in Figures 7.11C and D, respectively. The density in both plots is qualitatively different from those calculated for HCN-Cu. In particular, the density contours in the intermolecular bond area between the nitrogen and copper, exhibit a large increase in density near the nitrogen, in contrast to the overall decrease in density for the HCN-Cu complex. The polarization of the Cu_2 metal bond is apparent in both the MP2 and DFT density

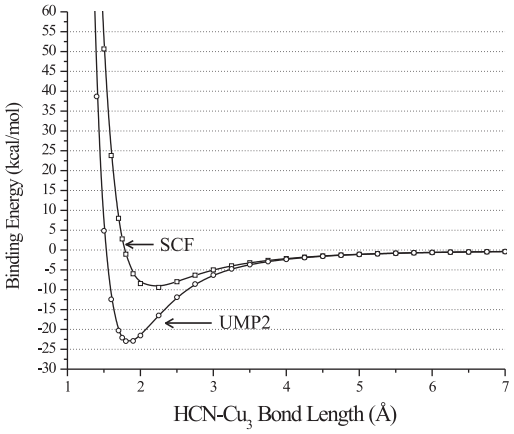

Figure 7.13: The 1-D UMP2 potential energy surface (red) of HCN-Cu_3 calculated at distances between the nitrogen on HCN and the nearest Cu atom (See Figure 7.3). The PES of the SCF energy is given in black.

plots and offers a clue to the dramatic increase in binding energy in going from HCN-Cu to HCN-Cu_2.

Fournier calculated the bonding of several ligands, including CO, to small Cu_n (n=1-3) clusters, using DFT [211]. In addition to the bonding geometry, Fournier found that the CO-Cu_n clusters share similar binding energies with the HCN-Cu_n complexes reported here. A large increase in binding energy was calculated when going from CO-Cu (19 kcal/mol) to CO-Cu_2 (29 kcal/mol) and it was concluded that this was due to the decrease in Pauli repulsion between CO and the 4s-derived molecular orbital (MO) on Cu_2. The mechanism for this decrease in repulsion was determined to be due to the mixing of the (4s + 4s)σ orbital with the (4s - 4s)σ^* orbital which allows the electron density to polarize away from the CO ligand. Qualitatively, this is what is seen in the electron density difference plot shown in Figures 7.11C and D. The nodal structure of the the (4s - 4s)σ^* is clearly present in the Cu_2 fragment along with the polarization away from the HCN fragment.

We now turn our attention to the HCN-Cu_3 complex and to the potential energy surface for this cluster given in Figure 7.13. This plot shows another large increase in binding energy between HCN and the Cu_3 cluster at both the MP2 and SCF level. The total binding energy has now increased to 23.1 kcal/mol. Like the HCN-Cu_2 complex, the SCF binding suggests that the interaction is fundamentally different from the HCN-Cu case.

The electron density difference plots (UMP2 and DFT) of HCN-Cu_3 are given in Figure 7.14 and show two views of the planar complex. Figures 7.14A and B give the view

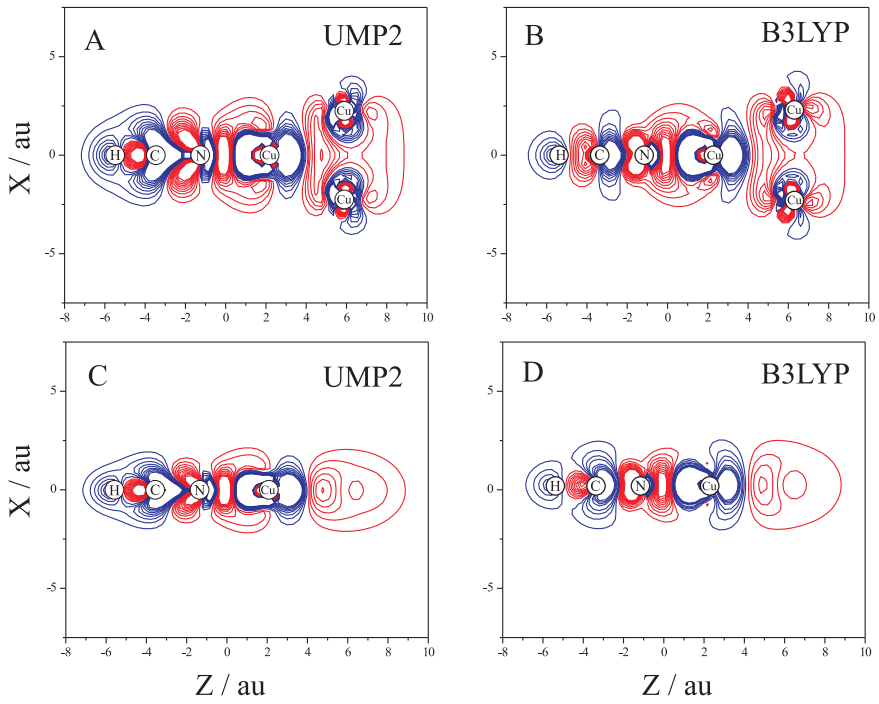

Figure 7.14: UMP2 and DFT Density difference plots for HCN-Cu3. (A) and (B) show the view normal to the Cu3 plane for the UMP2 and DFT densities, respectively. (C) and (D) show the in-plane view of the UMP2 and DFT densities, respectively. Contours range from -0.005 e/au^3 to +0.005 e/au^3 and are spaced at 0.0005 e/au^3 intervals. Positive and negative contours are given in red and blue, respectively.

of the complex normal to the plane, while Figures 7.14C and D view the complex in the plane formed by the Cu_3. Before we discuss the features of the density difference plots it is helpful to again revisit the CO-Cu_n calculations of Fournier. Like the CO-Cu_2 cluster, CO-Cu_3 shares some similarities with HCN-Cu_3 that make their comparisons useful. It was determined that the Cu_3 molecular orbitals derived from the in-plane 4p atomic orbitals of Cu, especially those perpendicular to the CO-Cu axis, are the major factors in stabilizing the CO-Cu_3 cluster, compared to the CO-Cu_2 complex. The stabilization energy arises from the mixing of the 4p derived MOs with the π^* MO on CO. Inspecting Figure 7.14, the importance of the mixing of the Cu_3 MOs with the π^* on HCN is clearly demonstrated. The electron density along the intermolecular bond between the nitrogen and Cu is similar to the HCN-Cu_2 complex, while the density *about* the intermolecular axis shows a large increase in density upon complexation, especially in the plane of the Cu_3 clusters (Figures 7.14A and B). We therefore conclude that HCN-Cu_3, like CO-Cu_3, derives a large part of its binding energy through the mixing of the 4p-derived MOs on Cu_3 and the π^* MOs on HCN.

Having unambiguously assigned each band, we would like to step back from the individual bonding characteristics of each HCN-Cu_n complex and examine the trends in vibrational shifts and binding energy as a function of cluster size. In addition to the complexes presented in this paper, we will also compare the nature of binding and C-H stretching frequency to the bulk copper limit. As it was stated above, HCN binds, nitrogen end down, to Cu(100) at an atop site and has a C-H frequency of 3294 cm^{-1} [1]. It was also calculated, using a model Cu_{13} cluster, that HCN binds (nitrogen end down) to an atop site, with a binding energy of 3.54 kcal/mol [222].

Chemical intuition suggests that the binary HCN-Cu complex, being furthest from the bulk limit, should be the poorest model for the binding of HCN onto a copper surface. However, counter to this intuition, we find that the binary complex is closest to the bulk both in terms of binding energy and in vibrational frequency. The HCN-Cu_2 and HCN-3 are blue-shifted relative to HCN-Cu and also have much higher binding energies. Obviously, at some point in the copper cluster's growth, the C-H stretch and the binding energy between HCN and the copper cluster must reverse the trend and red-shift towards 3294 cm^{-1}, as well as weaken in binding energy.

In order to investigate the question of when the turnaround in binding energy and frequency shift occurs, we have performed additional DFT calculations on the HCN-Cu_4 complex. The global minimum geometry of HCN-Cu4 (upper left) and its corresponding electron density difference map (upper right) are given in Figure 7.15. In these calculations, we used the same DFT methods (B3LYP) and basis sets used for the smaller HCN-Cu_{1-3} clusters.

The N-Cu bond length was calculated to be 1.9076 Å, an increase with respect to the HCN-Cu_3 but shorter than that of the HCN-Cu_2 complex. This pattern is reflected in the binding energy between HCN and Cu_4 as well. The calculated value of 15.8 kcal/mol lies above HCN-Cu_2 (14.4 kcal/mol) and below HCN-Cu_3 (20.6 kcal/mol). Interestingly, the vibrational frequency red-shift of the C-H stretch from the HCN monomer was calculated to be 1.84 cm^{-1}, showing a continued shift towards higher frequencies with increasing copper cluster size. For completeness, we give the electron density difference plot for HCN-Cu_4 in Figure 7.15. The pattern of electron density between the nitrogen and nearest copper atom is continued in the HCN-Cu_4 cluster. Similar to the HCN-Cu_2 and HCN-Cu_3 complexes, there is a large buildup of density near the nitrogen upon complexation, but there also appears to be slightly less density buildup about the N-Cu bond axis, when compared to HCN-Cu_3. This density pattern suggest that charge donation from the 4p MOs on Cu_4 to the π^* orbitals on HCN is less important than what was calculated for the HCN-Cu_3 complex (Figure 7.14).

A summary of the experimental and DFT vibrational frequencies is shown in the lower area of Figure 7.15. This plot is given to emphasize the vibrational shift pattern both observed and calculated for this system. It should be noted that we did not experimentally observe the HCN-Cu_4 complex. However, this is merely a result of current limitations in experimental methods. The capture of larger metal clusters should be possible be the use of larger helium droplets, which are made possible through the advances in closed-cycle helium refrigerator equipment. Many of these issues are discussed more thoroughly in an upcoming review article [**?**].

Assuming that the HCN-Cu_4 calculation is accurate, it is clear that the complex has not yet "turned back" towards the bulk surface regime. We are left with the question: How large must the copper cluster become so that HCN's C-H stretch and binding energy approach the bulk limit? The answer was addressed already by Fournier through his CO-Cu_n theoretical study [211]. We have already discussed similarities in geometry between the CO-Cu_n and HCN-Cu_n complexes. Apparently, there are also similarities in the trend of the binding energy between ligand and metal cluster as the cluster approaches the bulk limit. While discussing the binding energies of each CO-Cu_n cluster, Fournier commented that CO was calculated to be bound to the small copper clusters at energies 10-20 kcal/mol larger than what was measured for CO on a copper surface. Because the binding energy must become smaller at a critical copper cluster size, he speculated that only when clusters become large enough to have flat faces will the interaction energy approach the bulk limit. We feel that this is an excellent interpretation and similarly speculate that HCN will begin to decrease in binding energy and start shift its C-H stretch back towards 3294 cm^{-1} when the cluster,

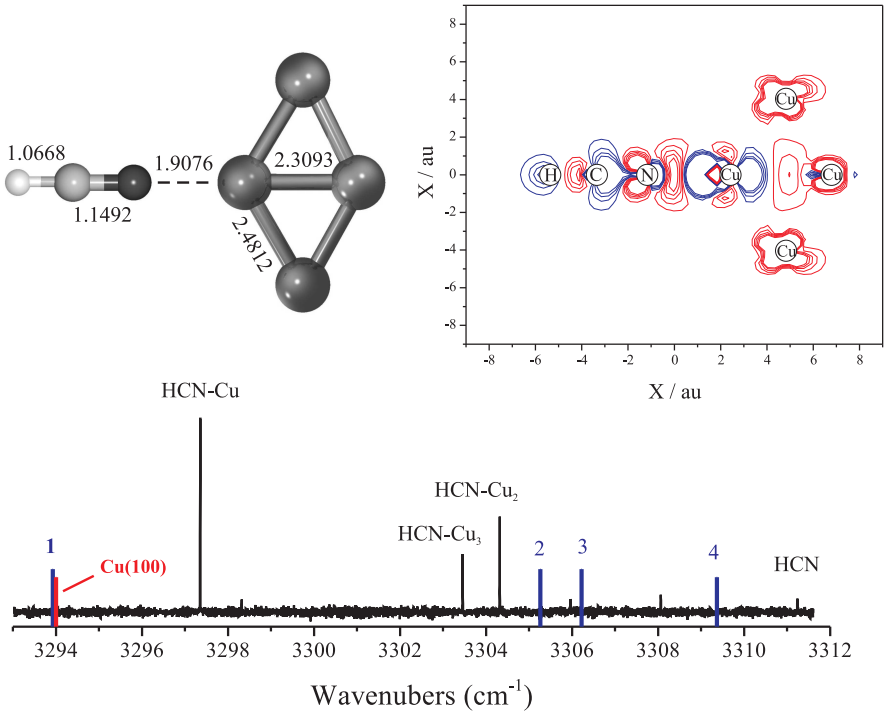

Figure 7.15: The bond lengths of HCN-Cu_4 (upper left) and the electron density difference plot (upper right) calculated using the B3LYP functional are given in the upper left and upper right, respectively. The experimental C-H stretches of HCN-Cu_n is overlayed with the experimental HCN-Cu(100) C-H stretch [1] (red) and the calculated HCN-Cu_n DFT C-H frequencies (blue). The reported DFT frequencies are calculated as frequency shifts from the calculated HCN monomer C-H stretch.

first becomes 3-dimensional, and then begins to approach the bulk limit when there are no longer any sharp corners on the cluster.

7.5 Summary

The rotationally resolved infrared spectra of HCN-Cu, HCN-Cu_2, and HCN-Cu_3 solvated in helium droplets have been reported. Through the comparisons of theoretical calculations with measured rotational constants, dipole moments and frequency shifts, we have reached unambiguous structure assignments for each complex. These structures are very similar to theoretical structures reported for CO-Cu_{1-3}.

The frequency shifts and calculated binding energies between HCN and Cu_{1-3} indicate that a dramatic change in the nature of binding occurs with increasing Cu cluster size. The HCN-Cu complex is weakly bound and van der Waals in nature, while the HCN-Cu_2 and HCN-Cu_3 are much more strongly bound and show covalent character in their electron density difference plots. This change in the nature of binding is reflected in the frequency shifts, as the HCN-Cu_2 and HCN-Cu_3 are blue-shifted relative to HCN-Cu, indicating a break-down in the hydrogen bond model of frequency shifts [217].

Comparisons of this work with previous RAIRS studies of HCN on a Cu(100) surface suggest that at large enough clusters, the HCN-Cu_n complex will begin to red-shift back towards the bulk limit (3294 cm-1) as well as revert to a weak van der Waals type bond.

Chapter 8

HCN-Ag$_n$ (n=1-3)

The structures, vibrational frequencies, and dipole moments of the HCN-Ag$_n$ (n=1-3) clusters are determined through high-resolution infrared spectroscopy. The complexes are formed and probed within superfluid helium droplets, whereby the helium droplet beam is passed over a resistively heated crucible containing silver shot and then through a gas HCN pickup cell. The HCN-Ag$_n$ clusters are compared with theory and the previously studied HCN-Cu$_n$ clusters.

8.1 Experimental

The essence of the experimental apparatus has been discussed elsewhere [119, 59]. The droplets were formed by expanding ultra-pure helium through a 5 micron nozzle. The nozzle was cooled to temperatures in the range of 19 K to 16 K and backed with 60 bar of helium pressure. These conditions produce average droplet sizes of about 6000 to 12000 helium atoms, respectively. After droplet formation and skimming, the droplet beam is passed just over the top of a resistively heated alumina crucible that contains the silver shot.

The HCN-Ag$_n$ seeded droplets were passed through the laser interaction region, where the C-H stretch of HCN is excited by an F-center laser (Burleigh FCL-20), operating on crystal 3 (RbCl:Li). Subsequent vibrational relaxation to the helium droplet results in the evaporation of approximately 600 helium atoms. The resulting depletion of the droplet beam is then detected by a liquid helium cooled bolometer [192]. The laser was amplitude modulated and the corresponding bolometer signals were measured using phase sensitive detection methods. The details associated with tuning and calibrating the laser can be found elsewhere [193].

An electric field could be applied to the laser interaction region using two metal electrodes. A considerable enhancement of the signal levels was obtained by using a large electric field

Table 8.1: The bond length (Å), harmonic frequency (cm^{-1}) and binding energy (eV) of the $^1\Sigma_g^+$ ground state of Ag_2 are compared with previous work.

Ag_2 $^1\Sigma_g^+$	R_e	ω_e
RMP2	2.5812	177.56
B3LYP	2.5888	178.11
B3LYP [225]	2.611	177.1
Expt [226]	2.530	192

(24 kV/cm) to record pendular spectra [60, 61], which was particularly useful when searching for new species. At more modest electric fields [78] (1-4 kV/cm) the resulting Stark spectra provided an accurate measure of the dipole moments of the HCN-Cu_n complexes.

8.2 Computational details and results

All MP2 calculations were performed with Molpro [186]. All DFT calculations were performed with Gaussian 03 [187]. In all calculations we used the small core Stuttgart-Dresden ECP (ECP10MDF) [184] along with the Stuttgart-Dresden valence basis set for copper [6s,5p,3d], which was augmented with 2f functions and 1g function, as optimized by Martin and Sundermann [189]. The 6-311++G** basis set was used for HCN.

The results of our calculations are given in Tables 8.1, 8.2, 8.3 and Figure 8.1. Comparisons of our results to previous experimental and theoretical work, show excellent agreement in all cases. We do not report the binding energy for the HCN-Ag DFT/B3LYP due to the well known problems this functional has with weakly bound species []. We also do not report the HCN-Ag4 MP2 structure due to the expense of this calculation. The binding energies between HCN and Ag_2, Ag_3 and Ag_4 are sufficiently large so that the DFT calculations should be reliable.

8.3 Pendular spectrum

The method of pendular spectroscopy [] has been shown to be extremely useful in the search of new, previously unobserved, spectra. As discussed above, a large electric field (24 kv/cm), parallel to the E field, was applied to the laser interaction region of the experimental apparatus. In the case of a parallel band, like HCN-Agn, the field orients the vibrational transition moment along with the laser polarization and collapses the rotational structure, thus giving a

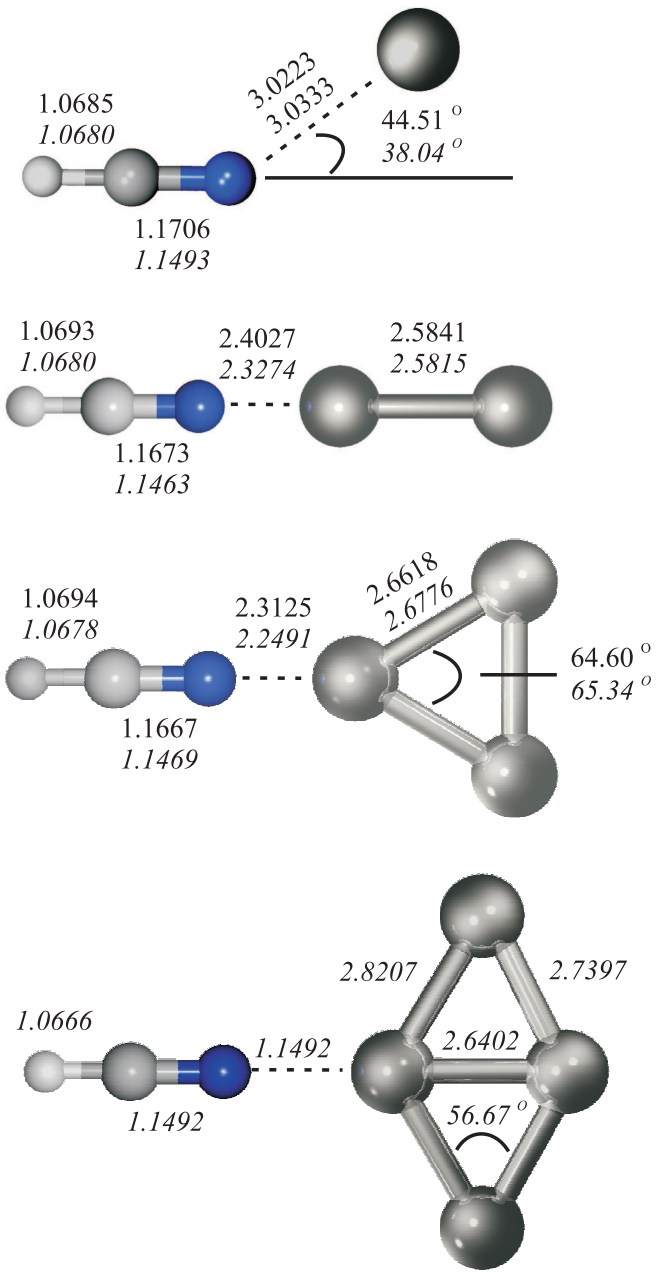

Figure 8.1: The structures of the HCN-Ag_n (n=1-4) complexes. The MP2 bond lengths and angles are given in the upper set of numbers while the B3LYP bond lengths and angles are given as the lower set (in italics). The MP2 structure for HCN-Ag_4 was not calculated.

Table 8.2: The $^2B_2$ electronic state of silver trimer is a Jahn-Teller distorted obtuse triangle. The bond length of legs (Å) and bond angle (degrees) of the triangle are given. The symmetric stretch (S.S.), asymmetric stretch (A.S.) and bend frequency (cm^{-1}) are also given.

Ag_3 $^2B_2$	R_e	θ	S.S.	Bend
RMP2	2.6479	68.12	167.8	62.7
CCSD(T) [227]	2.695	67.88	166.4	57.8

Table 8.3: The RMP2 and DFT harmonic vibrational red-shifts (from HCN monomer), dipole moments and binding energy between HCN and Ag_n.

	$\Delta\nu$ (cm^{-1})	μ (Debye)	D_e (kcal/mol)
HCN-Ag			
ROMP2	5.6	4.959	0.258
B3LYP	4.70	3.900	—
HCN-Ag_2			
MP2	9.73	6.473	6.25
B3LYP	7.30	6.763	6.57
HCN-Ag_3			
ROMP2	10.86	6.704	10.26
B3LYP	8.16	6.763	10.63

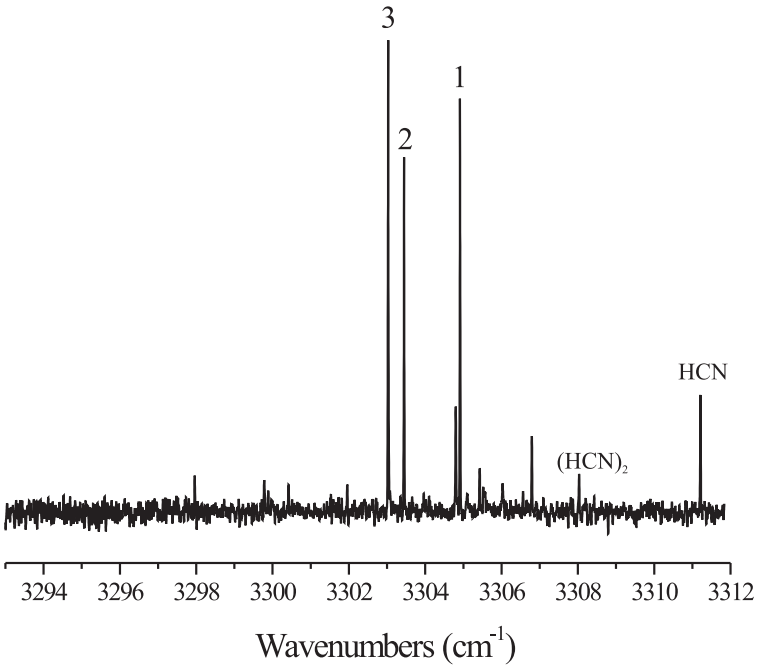

Figure 8.2: A pendular spectrum covering the free C-H stretch region of the HCN-Ag_n (n=1-3) clusters. The monoligated silver cluster size is labeled in the figure. This spectrum was taken with very low HCN pressures (2x10^{-6} Torr)to minimize signal contributions of HCN multimer peaks.

large increase in signal-to-noise. The pendular spectrum of HCN-Agn is shown in Figure 8.2 and was acquired with an average droplet size of 5740 He atoms, HCN pressure of 2.0x10^{-6} and He backing pressure of 60 bar. The well known HCN and HCN dimer peaks are labeled along with HCN-Ag$_n$ assignments, which were determined through a combitnation of using signal dependence techniques, field-free spectra and dipole moment measurements.

Let us begin with the determination of the peak assignments using signal optimization techniques. During a typical experiment when a new peak is discovered, we tune the laser to the peak of an individual pendular band. We then adjust the HCN pressure, average droplet size and metal oven temperature until the optimal signal is acquired. Because the pick-up of dopants by helium droplets is known to occur via Poisson statistics, adjusting these variables provides clues about which complexes correspond to which bands. Consider, for example, the band at 3304.9 cm^{-1}. At oven temperatures below 830^o C (10^{-4} torr vapor pressure of Ag) the only peak that is present, besides the HCN multimer peaks, is found at 3304.9 cm^{-1}. "Parking" the laser frequency on top of this peak and adjusting the HCN frequency we found that it optimized at HCN pressures just below the pressure found for HCN monomer, namely 6x10^{-6} torr, thus giving compelling evidence that the band also corresponds to a single HCN molecule. Working our way through the other peaks we found that the peaks assigned to higher order silver clusters required increasingly higher oven temperatures as well as increasingly higher average droplet sizes. The larger clusters optimized with larger droplet sizes for two reasons. One, the larger droplets have greater pick-up cross-sections and two, they have a greater heat capacity for the dissipation of condensation energy upon silver cluster formation. A full listing of the optimal experimental conditions for each band is given in Table x.

8.4 HCN-Ag

The assignment of each peak is not based solely on the optimization techniques discussed above. The great power of superfluid helium droplet spectroscopy is that rotational resolution is observed for species solvated within the droplet. Although the rotational constants are perturbed from their gas-phase counterparts, the overall symmetry of the spectra remains unchanged and structural determinations can be made. The pendular band already assigned to HCN-Ag based upon optimization techniques was scanned again in the absence of any electric field. The resulting spectra of taken at three different droplet sizes is shown in Figure 8.3. The spectrum is clearly that of a linear rotor (vibrationally averaged in this case), which is in agreement with the theoretical structure given in Figure 8.1. The spectra of

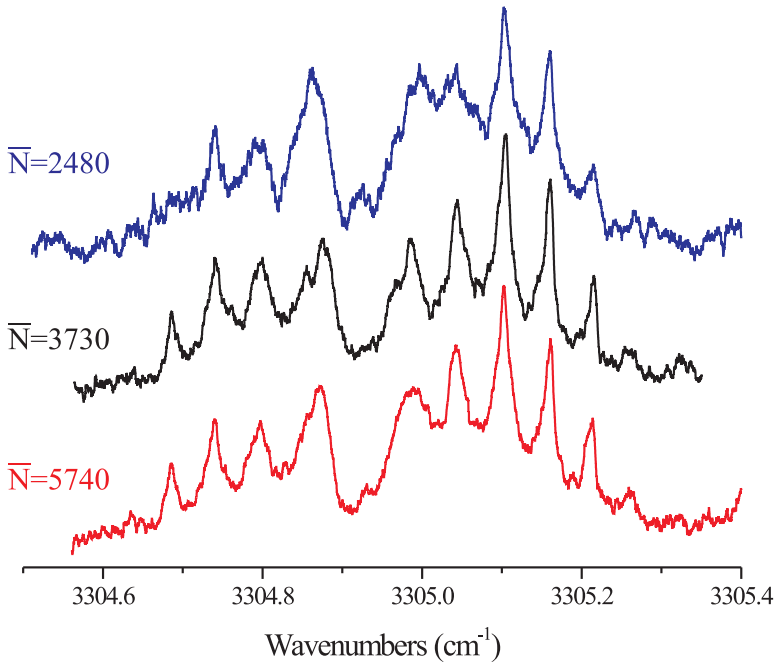

Figure 8.3: Three field-free spectra of HCN-Ag taken at various average droplet sizes.

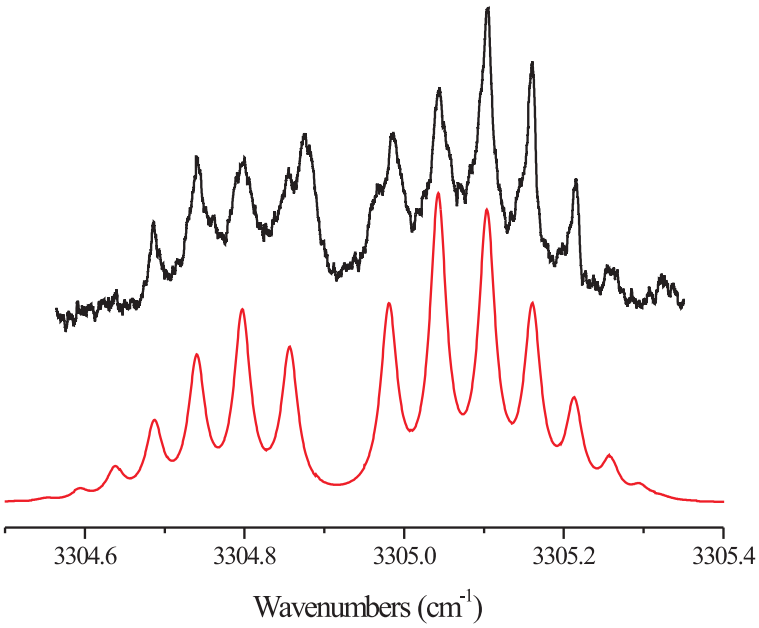

Figure 8.4: Three field-free spectrum and fit to a linear rotor Hamiltonian (red) of HCN-Ag.

Table 8.4: The vibrational origin (cm^{-1}), vibrational red-shift (cm^{-1}), linear rotor rotational constants (cm^{-1}) and dipole moments experimentally determined for HCN-Ag. The relevant theoretical values are also given.

	Expt		ROMP2	B3LYP
ν_0	3304.92			
$\Delta\nu_0$	6.29	$\Delta\nu_0$	5.60	4.70
B″	0.0308	B_e	0.0622	0.0609
B′	0.0313	$\frac{B_{gas}}{B_{He}}$	2.02	1.98
D″	$4.2x10^{-5}$			
D′	$5.1x10^{-5}$			
μ''	4.65 ± 0.05	μ	4.959	3.899
μ'	4.55 ± 0.05			

HCN-Ag are shown at different average droplet sizes because of the anomalous features near the vibrational origin of the spectrum. These peaks have been observed in other systems and have been interpreted as an interaction between the rotational states of the dopant and the helium surface bulk excitations. This interpretation is consistent with the observed spectra shown in Figure 8.3, where the spectrum acquired in smaller droplets is poorly resolved. A complete solvent-solute Hamiltonian is presumably required to fully understand the origin of these features but unfortunately such a Hamiltonian does not yet exist.

The fitting of the spectrum of HCN-Ag solvated within helium droplets was complicated by the features about the vibrational origin discussed above. The rotational constants (B and D) were fit in the ground and vibrationaly excited states while ignoring the R(0) and P(1) ro-vibrational bands. The resulting fit using a linewidth (FWHM) of 0.025 cm^{-1} is shown in Figure 8.4, and the resulting rotational constants are given in Table 8.4. The B rotational constant is reduced from the ROMP2 rotational constant by a factor of 2. As it has been discussed previously, the rotational constants of rotors solvated in helium droplets have been found to be reduced by a factor of 2.5 ±0.5, compared to their gas-phase values. This is due to the attractive potential between the solvent and solute which drags some of the helium density along with the dopant. An understanding of this process is an active area of theoretical research and significant progress has been made, but unfortunately a computationally feasible method for the calculation of helium's effect is still beyond the state of the art. We will refer to the empirically determined factor of 2.5 throughout this paper

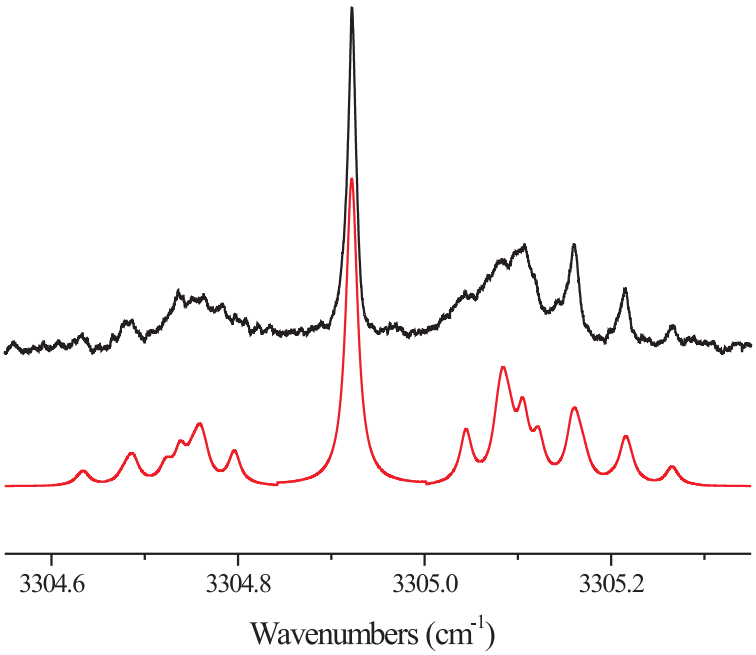

Figure 8.5: The Stark spectrum of HCN-Ag.

when comparing rotational constants. Another advantage of the free rotation of dopants within superfluid helium droplets is the ability to record the Stark spectra of molecules [120]. Figure 8.4 shows the Stark spectrum of HCN-Ag taken at a field of 2.055 kV/cm. This spectrum is one of 3 taken a various fields. The dipole moment was fit using our pendular rotor program. The rotational constants were taken from the previous field free spectrum fit (Table 8.4), thus allowing us to fit the Stark spectrum by adjusting the ground and vibrationally excited dipole moments. The results are given in Table 8.4. It is interesting to note that the vibrationally excited dipole moment (4.55 D) was found to be smaller than the ground state dipole moment (4.65 D). This is certainly counterintuitive due to the fact that the vibrationally excited state in the C-H stretch tends to elongate the C-H bond and therefore should increase the dipole moment. Similarly, it was found that the vibrationally excited B rotational constant was larger than the ground state. Again, this should be the opposite since the C-H bond length should increase upon vibrational excitation and thus lower the rotational constant. This odd behavior has not been seen before, to my knowledge, and is probably a consequence of the interaction between solvent and solute in the droplet.

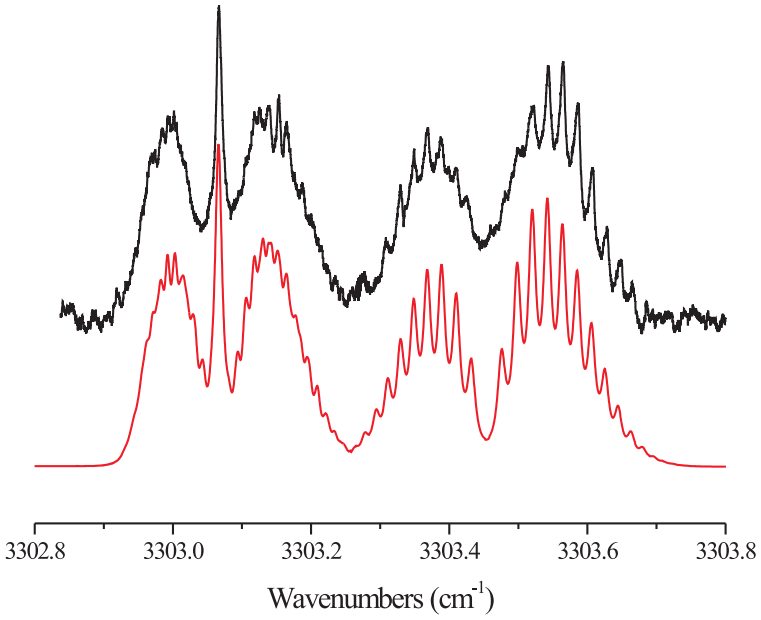

Figure 8.6: The field free spectrum of HCN-Ag_2 and HCN-Ag_3. The linear HCN-Ag_2 (no Q-branch) is at a higher frequency, while the asymmetric top, HCN-Ag_3, is shown at a lower frequency.

A comparison with theory reveals that the experimental dipole moment (4.65 D) is significantly smaller than the theoretical (4.959 D). We do not consider the DFT dipole moment due to DFT's poor performance with weakly bound complexes. The discrepancy between theory and experiment is due to vibrational averaging. Wide amplitude motion takes place between HCN and Ag, given that their corresponding interaction potential is quite shallow (-90 cm^{-1} calculated at the MP2 level).

HCN and Ag are weakly bound (ROMP2 = -90 cm^{-1}) and as such, can have wide amplitude motion with respect to each other. A full exploration of the degree to which vibrational averaging should have on the measured dipole moment requires a 2D potential energy surface and is beyond the scope of this chapter.

Table 8.5: The vibrational origin (cm^{-1}) and red-shift (cm^{-1})from HCN of the C-H stretch in HCN-Ag_2 determined from experiment and calculated through MP2 and DFT methods. The relevant experimental and theoretical rotational constants (cm^{-1}) for a linear rotor Hamiltonian. The experimental and theoretical dipole moments (Debye) are also given.

	Expt		MP2	B3LYP
ν_0	3303.45			
$\Delta\nu_0$	7.76	$\Delta\nu_0$	9.73	7.30
B″	0.01098	B_e	0.02068	0.02127
B′	0.0111	$\frac{B_{gas}}{B_{He}}$	1.9	1.9
D″	5.1x10^{-6}			
D′	5.2x10^{-6}			
μ	6.8 ± 0.3	μ	6.473	6.542

8.5 HCN-Ag_2 and HCN-Ag_3

Figure 8.2 shows two large bands red-shifted with respect to the HCN-Ag complex. These bands optimized at higher oven temperatures and larger average droplet sizes, indicating that they were due to larger silver clusters. The confirmation of the structures and identity of each peak was accomplished through the measurement of their field-free spectra. The two bands are close to each other and for convenience we will present both spectra simultaneously. The field-free spectra for HCN-Ag_2 and HCN-Ag_3 are shown in Figure 8.5. The higher frequency linear rotor spectrum optimizes at oven temperatures above the previously assigned HCN-Ag and at lower temperatures than the asymmetric top spectrum. Looking to the *ab initio* structures given in Figure 8.1, HCN-Ag_2 is a linear rotor and is the only possible complex that can give rise to the linear rotor spectrum shown in Figure 8.5. Likewise, the asymmetric top spectrum shown in Figure 8.5 can only be due to the HCN-Ag_3 structure shown in Figure 8.1. The rotational constants determined from the fits of each spectrum are in good agreement with the ab initio structures, as are the harmonic frequency calculations. A summary of the theoretical and experimentally determined observables are given in Table 8.5 and Table 8.6.

The agreement between the harmonic frequency shifts from HCN monomer are quite good, although it should be pointed out that this near quantitative agreement is primarily due to a fortuitous cancelation of errors. The dipole moments, on the other hand, (especially the HCN-Ag_3 complex) are not in good agreement. It is true that the helium solvent can shield the dopant from the full magnitude of the applied field, but as shown earlier, this usually

Table 8.6: The vibrational origin (cm^{-1}) and red-shift (cm^{-1}) from HCN of the C-H stretch in HCN-Ag_3 determined from experiment and calculated through ROMP2 and DFT methods. The experimental and theoretical rotational constants (cm^{-1}) for an asymmetric top Hamiltonian. The experimental and theoretical dipole moments (Debye) are also given.

	Expt		ROMP2	B3LYP
ν_0	3303.07			
$\Delta\nu_0$	8.14	$\Delta\nu_0$	10.86	8.17
$\overline{A}$	0.033	A_e	0.03862	0.03774
$\overline{B}$	0.00701	B_e	0.01956	0.01999
$\overline{C}$	0.00555	C_e	0.01299	0.01307
D	$1x10^{-6}$			
μ	7.5 ± 0.5	μ	6.705	6.763

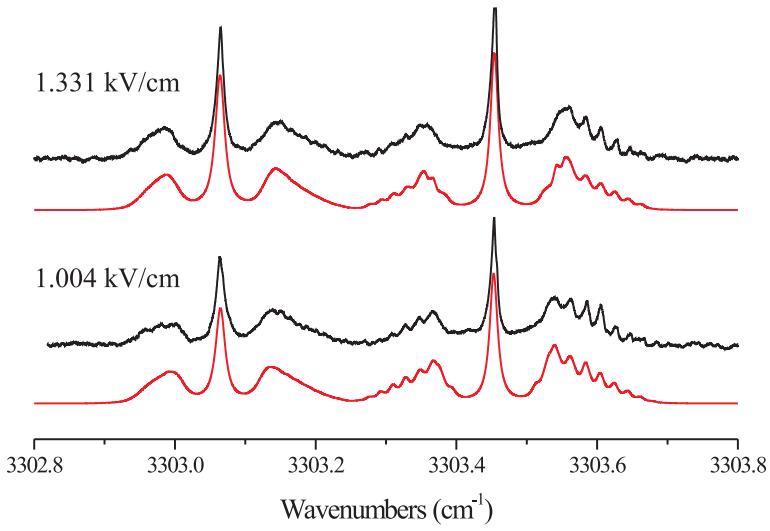

Figure 8.7: The Stark spectra of HCN-Ag_2 and HCN-Ag_3. The simulated spectra used to fit the data are shown below in red.

affects the measured dipole moment by 1 to 2 %. We feel that our measurements are sound and that the discrepancy is due to errors in the calculation. The Stark spectra taken at two different fields for these bands are shown in Figure 8.5.

8.6 Discussion

Besides structures and dipole moments, the data presented above gives a valuable information about the nature of the bond between the HCN ligand and the small silver clusters. The vibrational shift pattern of HCN-Cu_n (n=1-4) presented in the previous chapter showed a very interesting pattern when the binary HCN-Cu, HCN-Cu_n and HCN-Cu(100) species were compared. The HCN-Cu and HCN on Cu(100) were more similar in bond strength and in vibrational frequency than the rest of the complexes investigated. In addition, the HCN-Cu_2, HCN-Cu_3 and HCN-Cu_4 complexes were all blue-shifted with respect the the HCN-Cu and HCN on Cu(100) C-H stretch frequencies. The interpretation was as follows. In the theory of the vibrational shifts of van der Waals or hydrogen bonds, one typically looks to the excited vibrational state to understand the magnitude of the vibrational red-shift from the non-bonded monomer. Consider, for example, the HF-Ar and HF-Mg binary complexes. Both are weakly bound bound to the hydrogen end of the HF molecule, yet both have very different vibrational shifts, namely HF-Ar is red-shifted by 9.6 cm^{-1} while HF-Mg is shifted by 82 cm^{-1}. To a first order approximation, one can rationalize the difference in frequency shifts by comparing the polarizabilities of Ar and Mg, which are 1.586 $\mathring{A}^3$ and 10.6 $\mathring{A}^3$ respectively. Upon vibrational excitation, the HF bond length increases and as a result there is a corresponding increase in the dipole moment. The larger dipole moment increases the dipole induced dipole interaction energy between HF and its binding partner (Ar or Mg in this case), which is proportional to the polarizability of that binding partner. This increased binding energy lowers the excited state vibrational level, relative to the ground state, and results in a red-shift. Typically, the larger the interaction energy the larger the red-shift.

As stated above, this pattern was not seen for the HCN-Cu_n system and it was concluded that HCN-Cu_2, HCN-Cu_3 and HCN-Cu_4 were not described by the standard theory of vibrational frequency shifts due to hydrogen bonding [217] and that their bonding could be considered to be at least partially covalent. One of the methods used to help visualize the nature of the bond between HCN and Cu_n was through the use of electron density difference plot. These plots show the way electrons move as two fragments of a molecular complex are brought together. The DFT electron density difference plots of the HCN-Ag_n (n=2-4) are

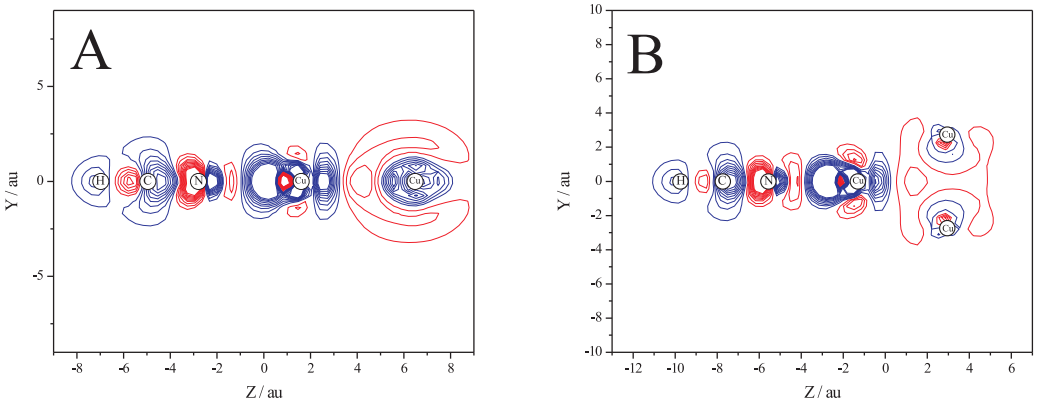

Figure 8.8: The electron density difference plot of (A) HCN-Ag_2 and (B) HCN-Ag_3 calculated using the B3LYP functional. Contours range from -0.005 e/au^3 to +0.005 e/au^3 and are spaced at 0.0005 e/au^3 intervals. Positive and negative contours are given in red and blue, respectively. ECP and basis set information can be found in the text.

shown in Figure 8.6. We do not show the HCN-Ag because there is little doubt that this is a van der Waals bond, dominated by dispersion and a dipole induced dipole interaction.

Let us begin by discussing the electron density difference plot of HCN-Ag_2. In the case of the HCN-Cu_2 complex it was concluded that the primary factor causing the increase in binding energy when going from HCN-Cu to HCN-Cu2 was due to Cu2's ability to polarize electron density into its (4s - 4s)σ^* molecular orbital, thus decreasing Pauli repulsion and increasing binding. Figure 8.6A gives the electron density difference plot of HCN-Ag2 and shows obvious similarities to the HCN-Cu_2. First, a nodal feature is observed between the two silver atoms, indicating that electron density has been pushed into the (5s - 5s)σ^* molecular orbital. Second, although to a lesser degree than the HCN-Cu_2, there is an increase in electron density near the lone pair on the nitrogen of HCN, which is presumably due to the charge donation interaction from the lone pair to the LUMO of the silver dimer. The binding energies of HCN-Ag2 and HCN-Cu2 calculated at the MP2 level are -6.24 and -16.2 kcal/mole, respectively. The difference between these two binding energies is consistent with previous work [210] and is qualitatively consistent with the presented electron density difference plots presented above.

The electron density difference plot for HCN-Ag_3 is given in Figure 8.6B. There is an increase in electron density near the nitrogen lone pair, consistent with the increased binding energy over the HCN-Ag_2 complex. Unlike the HCN-Cu_3 complex, we do not see a large

increase in the electron density about the N-Ag bond. It was concluded in the previous chapter that the large increase in density about the N-Cu bond in HCN-Cu3 was due to the interaction of the 4p derived molecular orbitals and the anti-bonding orbitals in HCN. Apparently, this interaction does not occur as readily with the 5p derived MOs in the HCN-Ag_3 complex.

Bibliography

[1] Celio, H.; Mills, P.; Jentz, D.; Pae, Y. I.; Trenary, M. *Langmuir* **1998,** *14,* 1379–1383.

[2] Bergeron, D. E.; Castleman, A. W.; Morisato, T.; Khanna, S. N. *Science* **2004,** *304,* 84–87.

[3] Duncan, M. A. *Spectroscopy and dynamics;* JAI Press: Greenwich, CT, 1993.

[4] Moskovits, M., Ed.; *Metal Clusters;* Wiley-Interscience: New York, 1986.

[5] Knickelbein, M. B. *Annu.Rev.Phys.Chem.* **1999,** *50,* 79–115.

[6] Haruta, M.; Tsubota, S.; Kobayashi, T.; Kageyama, H.; Genet, M. J.; Delmon, B. *J.Catal.* **1993,** *144,* 175–192.

[7] Yoon, B.; Hakkinen, H.; Landman, U.; Worz, A. S.; Antonietti, J.; Abbet, S.; Judai, K.; Heiz, U. *Science* **2005,** *307,* 403–407.

[8] Yoon, B.; Hakkinen, H.; Landman, U. *J.Phys.Chem. A* **2003,** *107,* 4066–4071.

[9] Hakkinen, H.; Yoon, B.; Landman, U.; Li, X.; Zhai, H.; Wang, L. *J.Phys.Chem. A* **2003,** *107,* 6168–6175.

[10] Hakkinen, H.; Landman, U. *Phys.Rev.B* **2000,** *62,* R2287–R2290.

[11] Luedtke, W. D.; Landman, U. *J.Phys.Chem. B* **1998,** *102,* 6566–6572.

[12] Sanchez, A.; Abbet, S.; Heiz, U.; Schneider, W. D.; Hakkinen, H.; Barnett, R. N.; Landman, U. *J.Phys.Chem. A* **1999,** *103,* 9573–9578.

[13] Goodman, D. W. *J.Phys.Chem.* **1996,** *100,* 13090–13102.

[14] Valden, M.; Lai, X.; Goodman, D. W. *Science* **1998,** *281,* 1647–1650.

[15] Zakin, M. R.; Brickman, R. O.; Cox, D. M.; Reichmann, K. C.; Trevor, D. J.; Kaldor, A. *J.Chem.Phys.* **1986,** *85,* 1198–1199.

[16] Knickelbein, M. B.; Koretsky, G. M. *J.Phys.Chem. A* **1998,** *102,* 580–586.

[17] Lehmann, K. K.; Scoles, G. *Science* **1998,** *279,* 2065–2066.

[18] Grebenev, S.; Hartmann, M.; Lindinger, A.; Portner, N.; Sartakov, B.; Toennies, J. P.; Vilesov, A. F. *Physica B* **2000,** *280,* 65–72.

[19] Hartmann, M.; Miller, R. E.; Toennies, J. P.; Vilesov, A. F. *Science* **1996,** *272,* 1631–1634.

[20] Onnes, H. K. *Commun.Phys.Lab.Univ.Leiden* **1908,** *108,* 3.

[21] Kapitza, P. *Nature* **1938,** *141,*.

[22] Landau, L. D. *J.Phys.USSR* **1941,** *5,* 71.

[23] Andronikashvilli, E. *Journal of Physics* **1946,** *3,* 201–206.

[24] Becker, E. W. *ZPD* **1986,** *3,* 101–107.

[25] Scheidemann, A.; Schilling, B.; Toennies, J. P.; Northby, J. A. *Physica.B* **1990,** *165,* 135–136.

[26] Scheidemann, A.; Toennies, J. P.; Northby, J. A. *Phys.Rev.Lett.* **1990,** *64,* 1899–1902.

[27] Lewerenz, M.; Schilling, B.; Toennies, J. P. *J.Chem.Phys.* **1995,** *102,* 8191–8207.

[28] Goyal, S.; Schutt, D. L.; Scoles, G. *Phys.Rev.Lett.* **1992,** *69,* 933–936.

[29] Frochtenicht, R.; Toennies, J. P.; Vilesov, A. F. *Chem.Phys.Lett.* **1994,** *229,* 1–7.

[30] Kwon, Y.; Whaley, K. B. *Phys.Rev.Lett.* **1999,** *83,* 4108–4111.

[31] Hartmann, M.; Portner, N.; Sartakov, B.; Toennies, J. P.; Vilesov, A. F. *J.Chem.Phys.* **1999,** *110,* 5109–5123.

[32] Kwon, Y.; Ceperley, D. M.; Whaley, K. B. *J.Chem.Phys.* **1996,** *104,* 2341–2348.

[33] Kwon, Y.; Whaley, K. B. *J.Chem.Phys.* **2003,** *119,* 1986–1995.

[34] Draeger, E. W.; Ceperley, D. M. *Phys.Rev.Lett.* **2003,** *90,* 065301-1–065301-4.

[35] Callegari, C.; Conjusteau, A.; Reinhard, I.; Lehmann, K. K.; Scoles, G.; Dalfovo, F. *Phys.Rev.Lett.* **1999,** *83,* 5058–5061.

[36] Huang, P.; Whaley, K. B. *J.Chem.Phys.* **2002,** *117,* 11244–11264.

[37] Zillich, R. E.; Whaley, K. B. *Physical Review B* **2004,** *69,* 104517.

[38] Paesani, F.; Kwon, Y.; Whaley, K. B. *Physical Review Letters* **2005,** *94,* 153401.

[39] Hartmann, M.; Miller, R. E.; Toennies, J. P.; Vilesov, A. F. *Phys.Rev.Lett.* **1995,** *75,* 1566–1569.

[40] Grebenev, S.; Hartmann, M.; Havenith, M.; Sartakov, B.; Toennies, J. P.; Vilesov, A. F. *J.Chem.Phys.* **2000,** *112,* 4485–4495.

[41] Grebenev, S.; Toennies, J. P.; Vilesov, A. F. *Science* **1998,** *279,* 2083–2086.

[42] Knuth, E. L.; Li, W.; Toennies, J. P. *Prog.Astronaut.Aeronaut.* **1989,** *117,* 329–334.

[43] Toennies, J. P.; Harms, J.; Knuth, E. L. *J.Chem.Phys.* **1997,** *106,* 3348–3357.

[44] Nauta, K.; Miller, R. E. The Spectroscopy of Molecules and Unique Clusters in Superfluid Liquid Helium Droplets. In ; Campargue, R., Ed.; Springer Verlag: 2001.

[45] Knuth, E. L.; Schilling, B.; Toennies, J. P. On Scaling Parameters for Predicting Cluster Sizes in Free Jets. In , Vol. 19; Oxford Univ. Press: Oxford, 1995.

[46] JIANG, T.; Northby, J. A. *Phys.Rev.Lett.* **1992,** *68,* 2620–2623.

[47] Knuth, E. L.; Henne, U. *J.Chem.Phys.* **1999,** *110,* 2664–2668.

[48] Lewerenz, M.; Schilling, B.; Toennies, J. P. *Chem.Phys.Lett.* **1993,** *206,* 381–387.

[49] Harms, J.; Toennies, J. P.; Dalfovo, F. *Phys.Rev.B* **1998,** *58,* 3341–3350.

[50] Buchenau, H.; Knuth, E. L.; Northby, J. A.; Toennies, J. P.; Winkler, C. *J.Chem.Phys.* **1990,** *92,* 6875–6889.

[51] Toennies, J. P.; Vilesov, A. F. *Annu.Rev.Phys.Chem.* **1998,** *49,* 1–41.

[52] Toennies, J. P.; Vilesov, A. F. *Angew.Chem.Int.Ed.Eng.* **2004,** *43,* 2622–2648.

[53] Mollenauer, L. F. Color Center Lasers. In ; Tang, C. L., Ed.; Academic Press: 1979.

[54] Kasper, J. V. V.; Pollock, C. R.; Curl Jr, R. F.; Tittel, F. K. *Appl.Optics* **1982,** *21,* 236–247.

[55] Burak, I.; Hepburn, J. W.; Sivakumar, N.; Hall, G. E.; Chawla, G. K.; Houston, P. L. *J.Chem.Phys.* **1987,** *86,* 1258–1268.

[56] Nauta, K. *Infrared Spectroscopy and Dynamics of Molecules and Molecular Complexes in Liquid Helium Droplets,* Thesis, 2000.

[57] Frochtenicht, R.; Kaloudis, M.; Koch, M.; Huisken, F. *J.Chem.Phys.* **1996,** *105,* 6128–6140.

[58] Goyal, S.; Schutt, D. L.; Scoles, G. *J.Phys.Chem.* **1993,** *97,* 2236–2245.

[59] Nauta, K.; Miller, R. E. *J.Chem.Phys.* **1999,** *111,* 3426–3433.

[60] Rost, J. M.; Griffin, J. C.; Friedrich, B.; Herschbach, D. R. *Phys.Rev.Lett.* **1992,** *68,* 1299–1301.

[61] Block, P. A.; Bohac, E. J.; Miller, R. E. *Phys.Rev.Lett.* **1992,** *68,* 1303–1306.

[62] Friedrich, B.; Herschbach, D. *Int.Rev.Phys.Chem.* **1996,** *15,* 325–344.

[63] Friedrich, B.; Herschbach, D. R. *Nature* **1991,** *353,* 412–414.

[64] Nauta, K.; Miller, R. E. *Science* **1999,** *283,* 1895–1897.

[65] Nauta, K.; Miller, R. E. *Science* **2000,** *287,* 293–295.

[66] Nauta, K.; Moore, D. T.; Stiles, P. L.; Miller, R. E. *Science* **2001,** *292,* 481–484.

[67] Lehmann, K. K. *J.Chem.Phys.* **2001,** *114,* 4643–4648.

[68] Paesani, F.; Gianturco, F. A.; Whaley, K. B. *J.Chem.Phys.* **2001,** *115,* 10225–10238.

[69] Viel, A.; Whaley, K. B. *J.Chem.Phys.* **2001,** *115,* 10186–10198.

[70] Lehmann, K. K.; Callegari, C. *J.Chem.Phys.* **2002,** *117,* 1595–1603.

[71] Lehmann, K. K. *Mol.Phys.* **1999,** *97,* 645–666.

[72] Stiles, P. L.; Moore, D. T.; Miller, R. E. *J.Chem.Phys.* **2003,** *118,* 7873–7881.

[73] Stiles, P. L.; Moore, D. T.; Miller, R. E. *J.Chem.Phys.* **2003,** .

[74] Dong, F.; Miller, R. E. *Science* **2002,** *298,* 1227–1230.

[75] Ebenstein, W. L.; Muenter, J. S. *J.Chem.Phys.* **1984,** *80,* 3989–3991.

[76] DeLeon, R. L.; Muenter, J. S. *J.Chem.Phys.* **1985,** *82,* 1702–1704.

[77] Gough, T. E.; Miller, R. E.; Scoles, G. *Faraday Discuss.Chem.Soc.* **1981,** *71,* 77–85.

[78] Nauta, K.; Miller, R. E. *Phys.Rev.Lett.* **1999,** *82,* 4480–4483.

[79] Higasi, K. *Sci.Papers Inst.Phys.Chem.Research (Tokyo)* **1936,** *28,* 284.

[80] Scaife, B. K. P. *Principles of Dielectrics;* volume Revised Oxford Science Publications: Oxford, 1998.

[81] Donnelly, R. J.; Barenghi, C. F. *J.Phys.Chem.Ref.Data* **1998,** *27,* 1217.

[82] Harris-Lowe, R. F.; Smee, K. A. *Phys.Rev.A* **1970,** *2,* 158–168.

[83] Kerns, K. P.; Parks, E. K.; Riley, S. J. *J.Chem.Phys.* **2000,** *112,* 3394–3407.

[84] Parks, E. K.; Nieman, G. C.; Kerns, K. P.; Riley, S. J. *J.Chem.Phys.* **1997,** *107,* 1861–1871.

[85] Copperthwaite, R. G.; Carley, J. S.; Roberts, M. W. *Surf.Sci.* **1986,** *165,* L1–L6.

[86] Tian, Z. J.; Yxklinten, U.; Lundqvist, B. I.; Jacobsen, K. W. *Surf.Sci.* **1991,** *258,* 427–438.

[87] Jenks, C. J.; Bent, B. E.; Bernstein, N.; Zaera, F. *J.Phys.Chem. B* **2000,** *104,* 3008–3016.

[88] Moskovits, M. *Acc.Chem.Res.* **1979,** *12,* 229–236.

[89] Klabunde, K. J. *Free atoms, clusters and nanoscale particles;* Academic Press: New York, 1994.

[90] Halonen, L.; Bernasek, S. L.; Nesbitt, D. J. *J.Chem.Phys.* **2001,** *115,* 5611–5619.

[91] Bauschlicher, C. W. *J.Chem.Phys.* **1994,** *101,* 3250–3254.

[92] Yang, H.; Caves, T. C.; Whitten, J. L. *J.Chem.Phys.* **1995,** *103,* 8756–8763.

[93] Wang, L. S.; Wu, H. Proboing the Electronic Structureof Transition Metal Clusters From Molecular To Bulk-like Using Photoelectron Spectroscopy. In ; Duncan, M. A., Ed.; JA1 Press, Inc.: Greenwich, CT, 21998.

[94] Edwards, P. P.; Johnston, R. L.; Rao, C. N. R. On the Size-Induced Metal-Insulator Transition in Clusters and Small Particles. In ; Braunstein, P.; Oro, L. A.; Raithby, P. R., Eds.; Wiley-VCH: 1998.

[95] Wang, L.; Li, X.; Zhang, H. *Chem.Phys.* **2000,** *262,* 53–63.

[96] Lombardi, J. R.; Davis, B. *Chem.Rev.* **2002,** *102,* 2431–2460.

[97] Barnett, R. N.; Cleveland, C. L.; Hakkinen, H.; Luedtke, W. D.; Yannouleas, C.; Landman, U. *Eur.Phys.J.D.* **1999,** *9,* 95–104.

[98] Schafer, M.; Pratt, D. W. *J.Chem.Phys.* **2002,** *115,* 11147–11156.

[99] Thomas, O. C.; Zheng, W.; Bowen, K. H. *J.Chem.Phys.* **2001,** *114,* 5514–5519.

[100] Liu, K.; Parks, E. K.; Richtsmeier, S. C.; Pobo, L. G.; Riley, S. J. *J.Chem.Phys.* **1985,** *83,* 2882–2888.

[101] Jackson, K. A.; Knickelbein, M. B.; Koretsky, G. M.; Srinivas, S. *Chem.Phys.* **2000,** *262,* 41–51.

[102] Evans, C.; Gerry, M. C. L. *J.Phys.Chem. A* **2001,** *105,* 9659–9663.

[103] Lin, W.; Beaton, S. A.; Evans, C. J. *J.Mol.Spectrosc.* **2000,** *199,* 275–283.

[104] Richards, P. L.; Tobin, R. G. Infrared Spectroscopy of Adsorbates on Metals: Direct Absorption and Emission. In ; 1987.

[105] Trenary, M. *Annu.Rev.Phys.Chem.* **2000,** *51,* 381–403.

[106] Illas, F.; Ricart, J. M.; Fernandez-Garcia, M. *J.Chem.Phys.* **1996,** *104,* 5647–5656.

[107] Kim, C.; Yurgenson, S.; Northby, J. A. *ZPD* **1997,** *40,* 119–122.

[108] Gough, T. E.; Mengel, M.; Rowntree, P.; Scoles, G. *Proc.SPIE-Int.Soc.Opt.Eng.* **1986,** *669,* 129–132.

[109] Peet, A. C.; Yang, W. *Chem.Phys.Lett.* **1988,** *153(1),* 98–104.

[110] Werner, H. J. *et al.* **2002,** .

[111] Boys, S. F.; Bernardi, F. *Mol.Phys.* **1970,** *19(4),* 553–566.

[112] Evans, C. J.; Gerry, M. C. L. *J.Chem.Phys.* **2000,** *112,* 9363–9374.

[113] Evans, C. J.; Lesarri, A.; Gerry, M. C. L. *J.Am.Chem.Soc.* **2000,** *122,* 6100–6105.

[114] Norman, L.; Evans, C. J.; Gerry, M. C. L. *J.Mol.Spectrosc.* **2000,** *199,* 311–313.

[115] Jug, K.; Zimmermann, B.; Calaminici, P.; Koster, A. M. *J.Chem.Phys.* **2002,** *116,* 4497–4507.

[116] Kaplan, I. G.; Roszak, S.; Leszczynski, J. *J.Chem.Phys.* **2000,** *113,* 6245–6252.

[117] Nauta, K.; Miller, R. E. *J.Chem.Phys.* **2001,** *115,* 8384–8392.

[118] Callegari, C.; Lehmann, K. K.; Schmied, R.; Scoles, G. *J.Chem.Phys.* **2001,** *115,* 10090–10110.

[119] Nauta, K.; Moore, D. T.; Miller, R. E. *Faraday Discuss.Chem.Soc.* **1999,** *113,* 261–278.

[120] Stiles, P. L.; Nauta, K.; Miller, R. E. *Phys.Rev.Lett.* **2003,** *90,* 135301.

[121] Nauta, K.; Miller, R. E. *J.Chem.Phys.* **2001,** *115,* 10254–10260.

[122] Leopold, K. R.; Fraser, G. T.; Lin, F. J.; Nelson Jr, D. D.; Klemperer, W. *J.Chem.Phys.* **1984,** *81,* 4922–4931.

[123] Anderson, D. T.; Hinde, R. J.; Tam, S.; Fajardo, M. E. *J.Chem.Phys.* **2002,** *116,* 594–607.

[124] Bumgarner, R. E.; Blake, G. A. *Chem.Phys.Lett.* **1989,** *161,* 308–314.

[125] Drucker, S.; Tao, F. M.; Klemperer, W. *J.Phys.Chem.* **1995,** *99,* 2646–2655.

[126] Tao, F. M.; Drucker, S.; Klemperer, W. *J.Chem.Phys.* **1995,** *102,* 7289–7297.

[127] Thornley, A. E.; Hutson, J. M. *J.Chem.Phys.* **1994,** *101,* 5578–5584.

[128] Tennyson, J.; Sutcliffe, B. T. *J.Chem.Phys.* **1983,** *79,* 43–51.

[129] Collatz, L. *The Numerical Treatment of Differential Equations;* volume 1 Springer: Berlin, 1960.

[130] Bemish, R. J.; Block, P. A.; Pedersen, L. G.; Yang, W. T.; Miller, R. E. *J.Chem.Phys.* **1993,** *99,* 8585–8598.

[131] Yang, X.; Kerstel, E. R. T.; Scoles, G.; Bemish, R. J.; Miller, R. E. *J.Chem.Phys.* **1995,** *103,* 8828–8839.

[132] Gutowsky, H. S.; Keen, J. D.; Germann, T. C.; Emilsson, T.; Augspurger, J. D.; Dykstra, C. E. *J.Chem.Phys.* **1993,** *98,* 6801–6809.

[133] Bauschlicher, C. W.; Partridge, H. *Chem.Phys.Lett.* **1999,** *300,* 364–368.

[134] Kaplan, I. G.; Roszak, S.; Leszczynski, J. *Adv.Quantum.Chem.* **2001,** *40,* 257–278.

[135] Kohn, A.; Weigend, F.; Ahlrichs, R. *Berichte der Bunsen-Gesellschaft-Physical Chemistry Chemical Physics* **2001,** *3,* 711–719.

[136] Yin, X. L.; Wan, L. J.; Yang, Z. Y.; Yu, J. Y.; Bai, C. L. *Surf.Sci.* **2003,** *531,* 226–230.

[137] Kiyohara, T.; Shinohara, H.; Kasahara, T.; Okubo, R.; Itoh, K. *J.Phys.Chem. B* **2003,** *107,* 5008–5015.

[138] Sykes, E. C. H.; Han, P.; Weiss, P. S. *J.Phys.Chem. B* **2003,** *107,* 5016–5021.

[139] McNutt, A.; Haq, S.; Raval, R. *Surf.Sci.* **2003,** *531,* 131–144.

[140] Brown, W. A.; King, D. A. *J.Phys.Chem. B* **2000,** *104,* 2578–2595.

[141] Hammer, B.; Norskov, J. K. *Surf.Sci.* **1995,** *343,* 211–220.

[142] Cavanagh, R. R.; King, D. S.; Stephenson, J. C.; Heinz, T. F. *J.Phys.Chem.* **1993,** *97,* 786–798.

[143] Dixon-Warren, S. J.; Jensen, E. T.; Polanyi, J. C. *Physical Review Letters* **1991,** *67,* 2395–2398.

[144] Harris, A. L.; Rothberg, L.; Dhar, L.; Levinos, N. J.; Dubois, L. H. *J.Chem.Phys.* **1991,** *94,* 2438–2448.

[145] Neurock, M.; Vansanten, R. A. *J.Am.Chem.Soc.* **1994,** *116,* 4427–4439.

[146] Tevelde, G.; Baerends, E. J. *Chem.Phys.* **1993,** *177,* 399–406.

[147] Headgordon, M.; Tully, J. C. *Physical Review B* **1992,** *46,* 1853–1856.

[148] Pacchioni, G.; Cogliandro, G.; Bagus, P. S. *Int.J.Quantum Chem.* **1992,** *42,* 1115–1139.

[149] Duncan, M. A., Ed.; *Advances in Metal and Semiconductor Cluster;* JAI Press: Greenwich, 1993.

[150] Scoles, G., Ed.; *The Chemical Physics of Atomic and Molecular Clusters;* North-Holland: Amsterdam, 1990.

[151] Puddephatt, R. J. Metal Clusters in Catalysis- An Overview. In ; Braunstein, P.; Oro, L. A.; Raithby, P. R., Eds.; Wiley-VCH: 1998.

[152] Hermann, K.; Witko, M.; Michalak, A. *Zeitschrift fur Physikalische Chemie* **1996,** *197,* 219–235.

[153] Hermann, K.; Witko, M. *J.Mol.Struct.* **1999,** *458,* 81.

[154] Schmid, G. Nanosized Clusters on and in Supports - Perspective for Future Catalysis. In ; Braunstein, P.; Oro, L. A.; Raithby, P. R., Eds.; Wiley-VCH: 1998.

[155] Mcintyre, B. J.; Salmeron, M.; Somorjai, G. A. *Science* **1994,** *265,* 1415–1418.

[156] Thomas, O. C.; Zheng, W.; Xu, S.; Bowen, K. H. *Phys.Rev.Lett.* **2002,** *89,* 213403.

[157] Salazar, M. C.; Paz, J. L.; Hernandez, A. J. *J.Mol.Struct.-Theochem* **1998,** *426,* 53–58.

[158] Lide, D. R., Ed.; *CRC Handbook of Chemistry and Physics;* volume 71 CRC Press: Boca Raton, 1990.

[159] DeLeon, R. L.; Muenter, J. S. *J.Chem.Phys.* **1984,** *80,* 3992–3999.

[160] Balfour, W. J.; Douglas, A. E. *Can.J.Phys.* **1970,** *48,* 901–901.

[161] Eley, D. D.; Wilkinson, P. R. *Proc.R.Soc.London,A* **1960,** *254,* 327.

[162] Nauta, K.; Miller, R. E. *J.Chem.Phys.* **2001,** *115,* 10138–10145.

[163] Douberly, G. E.; Miller, R. E. *To Be Published* **2003,** .

[164] Lee, T. J.; Rendell, A. P.; Taylor, P. R. *J.Chem.Phys.* **1990,** *92,* 489–495.

[165] Akola, J.; Rytkonen, K.; Manninen, M. *Eur.Phys.J.D.* **2001,** *16,* 21–24.

[166] deCoulon, V.; Delaly, P.; Ballone, P.; Buttet, J.; Reuse, F. *ZPD* **1991,** *19,* 173–176.

[167] Dong, F.; Miller, R. E. *J.Phys.Chem. A* **2004,** *108,* 2181–2191.

[168] Hirshfeld, F. L. *Theor.Chim.Acta* **1977,** *44,* 129.

[169] Mills, G.; Gordon, M. S.; Metiu, H. *J.Chem.Phys.* **2003,** *118,* 4198–4205.

[170] Busani, R.; Folkers, M.; Cheshnovsky, O. *Phys.Rev.Lett.* **1998,** *81,* 3836–3839.

[171] Kaiser, B.; Rademann, K. *Phys.Rev.Lett.* **1992,** *69,* 3204–3207.

[172] Brechignac, C.; Broyer, M.; Cahuzac, P.; Delacretaz, G.; Labastie, P.; Wolf, J. P.; Woste, L. *Phys.Rev.Lett.* **1988,** *60,* 275.

[173] Pastor, G. M.; Stampfli, P.; Bennemann, K. H. *Europhys.Lett.* **1988,** *7,* 419–424.

[174] Garcia, M. E.; Pastor, G. M.; Bennemann, K. H. *Physical Review Letters* **1991,** *67,* 1142–1145.

[175] Ruppel, M.; Rademann, K. *Chem.Phys.Lett.* **1992,** *197,* 280–285.

[176] Yonezawa, F.; Tanikawa, H. *J.Non-Cryst.Solids* **1996,** *205-207,* 793–796.

[177] Flad, H. J.; Schautz, F.; Wang, Y.; Dolg, M.; Savin, A. *Eur.Phys.J.D.* **1999,** *6,* 243–254.

[178] Yu, M.; Dolg, M. *Chem.Phys.Lett.* **1997,** *273,* 329–336.

[179] Wang, J.; Wang, G.; Zhao, J. *Phys.Rev.A* **2003,** *68,* 013201.

[180] Haberland, H., Ed.; *Clusters of Atoms and Molecules I;* Springer-Verlag: Berlin, 1995.

[181] Stiles, P. L.; Moore, D. T.; Miller, R. E. *J.Chem.Phys.* **2004,** *121,* 3130.

[182] Paesani, F.; Whaley, K. B. *J.Chem.Phys.* **2004,** *121,* 4180–4192.

[183] Kaplan, I. G. *Int.J.Quantum Chem.* **1999,** *74,* 241–247.

[184] Dolg, M.; Wedig, U.; Stoll, H.; Preuss, H. *J.Chem.Phys.* **1987,** *86,* 866–872.

[185] Mller, W.; Flesch, J.; Meyer, W. *J.Chem.Phys.* **1984,** *80,* 3297.

[186] Werner, H. J. *et al.* **2002,** .

[187] Frisch, M. J. *et al.* **2003,** .

[188] Peterson, K. A.; Figgen, D.; Goll, E.; Stoll, H.; Dolg, M. *J.Chem.Phys.* **2003,** *119,* 11113–11123.

[189] Martin, J. M. L.; Sundermann, A. *J.Chem.Phys.* **2001,** *114,* 3408–3420.

[190] Schautz, F.; Flad, H. J.; Dolg, M. *Theor.Chem.Acc.* **1998,** *99,* 231–240.

[191] Nauta, K.; Miller, R. E. *J.Chem.Phys.* **2001,** *115,* 4508–4514.

[192] Cavallini, M.; Gallinaro, G.; Scoles, G. *Z.Naturforsch.A* **1967,** *22,* 413–414.

[193] Huang, Z. S.; Jucks, K. W.; Miller, R. E. *J.Chem.Phys.* **1986,** *85,* 3338–3341.

[194] Moore, D. T.; Oudejans, L.; Miller, R. E. *J.Chem.Phys.* **1999,** *110,* 197–208.

[195] Carter, S.; Mills, I. M.; Handy, N. C. *J.Chem.Phys.* **1992,** *97,* 1606–1607.

[196] Bondi, A. *J.Phys.Chem.* **1964,** *68,* 441–451.

[197] Douberly, G. E.; Miller, R. E. *J.Phys.Chem. B* **2003,** *107,* 4500–4507.

[198] Bauschlicher Jr, C. W.; Bagus, P. S.; Cox, B. N. *J.Chem.Phys.* **1982,** *77,* 4032–4038.

[199] Gullberg, D.; Litzen, U. *Physica Scripta* **2000,** *61,* 652–656.

[200] Delaly, P.; Ballone, P.; Buttet, J. *Phys.Rev.B* **1992,** *45,* 3838–3841.

[201] Gong, X. G.; Zheng, Q. Q.; He, Y. *Phys.Lett.A* **1993,** *181,* 459–464.

[202] Bowen, K. H. **2002,** .

[203] Duncan, M. *Int.Rev.Phys.Chem.* **2003,** *22,* 407-435.

[204] Haruta, M. *Catalysis Today* **1997,** *36,* 153-166.

[205] Northby, J. A. *J.Chem.Phys.* **2001,** *115,* 10065–10077.

[206] Stienkemeier, F.; Vilesov, A. F. *J.Chem.Phys.* **2001,** *115,* 10119–10137.

[207] Barnett, R. N.; Whaley, K. B. *J.Chem.Phys.* **1993,** *99,* 9730–9744.

[208] Choi, M.; Douberly, G.; Falconer, T.; Lewis, W.; Lindsay, C.; Merritt, J.; Stiles, P.; Miller, R. *Int.Rev.Phys.Chem.* **2006,** *In press,*.

[209] Florez, E.; Tiznado, W.; Mondragon, F.; Fuentealba, P. *J.Phys.Chem. A* **2005,** *109,* 7815–7821.

[210] Chan, W. T.; Fournier, R. *Chem.Phys.Lett.* **1999,** *315,* 257–265.

[211] Fournier, R. *J.Chem.Phys.* **1995,** *102,* 5396–5407.

[212] Ram, R. S.; Jarman, C. N.; Bernath, P. F. *J.Mol.Spectrosc.* **1992,** *156,* 468–486.

[213] Pou-Amerigo, R.; Merchan, M.; Nebot-Gil, I.; Malmqvist, P. A.; Roos, B. O. *J.Chem.Phys.* **1994,** *101,* 4893–4902.

[214] Papas, B. N.; Schaefer III, H. F. *J.Chem.Phys.* **2005,** *123,* 074321/1–074321/12.

[215] Berces, A. *Spectrochimica Acta, Part A: Molecular and Biomolecular Spectroscopy* **1997,** *53A,* 1257–1272.

[216] Moskovits, M.; Hulse, J. E. *J.Phys.Chem.* **1977,** *81,* 2004–2007.

[217] Liu, S. Y.; Dykstra, C. E. *J.Phys.Chem.* **1986,** *90,* 3097–3103.

[218] Lee, E.; Farrelly, D.; Whaley, K. B. *Phys.Rev.Lett.* **1999,** *83,* 3812–3815.

[219] Kwon, Y.; Huang, P.; Patel, M. V.; Blume, D.; Whaley, K. B. *J.Chem.Phys.* **2000,** *113,* 6469–6501.

[220] Kwon, Y.; Whaley, K. B. *J.Low Temp.Phys.* **2005,** *138,* 253–258.

[221] Dkhissi, A.; Alikhani, M. E.; Bouteiller, Y. *J.Mol.Struct.* **1997,** *416,* 1–9.

[222] Jian-Ming, H.; Yi, L.; Jun-Qian, L.; Yong-Fan, Z. *Acta Chimica Sinica* **2002,** *23,* 181–184.

[223] Stiles, P. L.; Miller, R. E. *In preparation* **2006,** .

[224] Badenhoop, J. K.; Weinhold, F. *J.Chem.Phys.* **1997,** *107,* 5406–5421.

[225] Wang, X. W.; Wan, X. W.; Zhou, H.; Takami, S.; Kubo, M.; Miyamoto, A. *J.Mol.Struct.(Theochem)* **2002,** *579,* 221–227.

[226] Morse, M. D. *Chem.Rev.* **1986,** *86,* 1049–1109.

[227] Yoon, J.; Kim, K. S.; Baeck, K. K. *Journal of Chemical Physics* **2000,** *112,* 9335–9342.